Alma Mater Studiorum – Università di Bologna

Dipartimento di Fisica e Astronomia
Corso di Laurea magistrale in Astrofisica e Cosmologia

The X-ray Variability and Multiphase Winds of a Changing-Look AGN at z=0.149

Tesi di laurea

Presentata da:
Pietro Baldini

Relatore:
Chiar.ma Prof.ssa Marcella Brusa

Correlatori:
Dott. Giorgio Lanzuisi
Dott. Andrea Merloni

Anno accademico 2021-2022

Abstract

According to the Active Galactic Nuclei (AGN) Unified Model, the main discriminant between AGN of different classifications is the viewing angle. The discovery of "Changing Look" AGN (CL-AGN), a subclass that shows drastic spectral variations on relatively short timescales, poses a threat to the static Unified Model and requires either a better understanding of accretion physics or the inclusion of more complex, dynamical processes. Characterizing such objects is of crucial importance in order to assess where our theories come short. 2MASS 0918+2117 (2M0918) is a CL-AGN, as witnessed by 2 XMM-Newton observations (respectively dating 2003 and 2005, Pounds & Wilkes 2007) which revealed an increase in its X-ray flux by a factor ~ 10, possibly due to a decrease in obscuration. In this work we re-analyze the XMM-Newton spectra available in the archive, investigate the nature of the variability and interpret it in a dynamical framework. We do so by extending the light curve (both from a spectral and from a brightness point of view) through dedicated 2020 XMM-Newton and NuSTAR follow-up observations and data from the first 4 eROSITA all-sky surveys. The 2005 spectrum shows tentative evidence of absorption features above 7.8 keV rest-frame, which can be interpreted as highly ionized, dense, and fast winds launched from the accretion disk, known in literature as Ultra Fast Outflows (UFO). The feature is confirmed following the analysis of the X-ray spectra obtained in 2020, where we detected at $> 99\%$ significance UFOs with v=0.15c. Overall the X-ray spectral properties of 2M0918 suggest a scenario in which winds play a crucial role in the displacement of obscuring material in and out of the line of sight. In addition, the 2005 SDSS optical spectrum reveals the presence of outflows in the ionized phase on kpc scale, with velocities up to 1000 km/s. The almost simultaneous detection of accretion disk- and galaxy-scale winds allows to constrain outflow propagation mechanisms, which in the case of 2M0918 is consistent with a momentum-driven scenario.

Contents

Chapter 1

Introduction: AGN, Variability & Feedback

1.1 Super Massive Black Holes & Active Galactic Nuclei

Super Massive Black Holes (SMBH) are astrophysical objects predicted by General Relativity and described by extreme masses ($M_{SMBH} > 10^6 M_\odot$) entrained in very compact regions ($r < 1 - 10$ AU). Due to the high compactness, the gravitational potential has to be described as a space-time singularity, from which not even light can escape, once it crosses the so-called "Event Horizon".

Because they do not emit any radiation, their presence was only indirectly inferred from stellar and gas dynamics, which revealed that all massive galaxies and most galaxies in general host a SMBH in their inner regions. It was only in 2019 that the first ever image of a SMBH was produced at 1.3mm by the Event Horizon Telescope Collaboration (EHT), an international collaboration that combines facilities around the globe into an Earth-size baseline interferometer with ~ 30 microarcsecond resolution (Event Horizon Telescope Collaboration et al. 2019a, Event Horizon Telescope Collaboration et al. 2019b). The first image looked at the nucleus of the local galaxy M87, while in 2022 the EHT unveiled Sgr A*, the SMBH lying at the center of our own galaxy (Event Horizon Telescope Collaboration et al. 2022, See Fig. 1.1). This provided the first direct evidence of the existence of SMBHs, by imaging the "black hole shadow", which is the projected region where circular photon orbits can exist (See e.g. Bronzwaer and Falcke 2021 for an in-depth discussion on the nature of the black hole shadow).

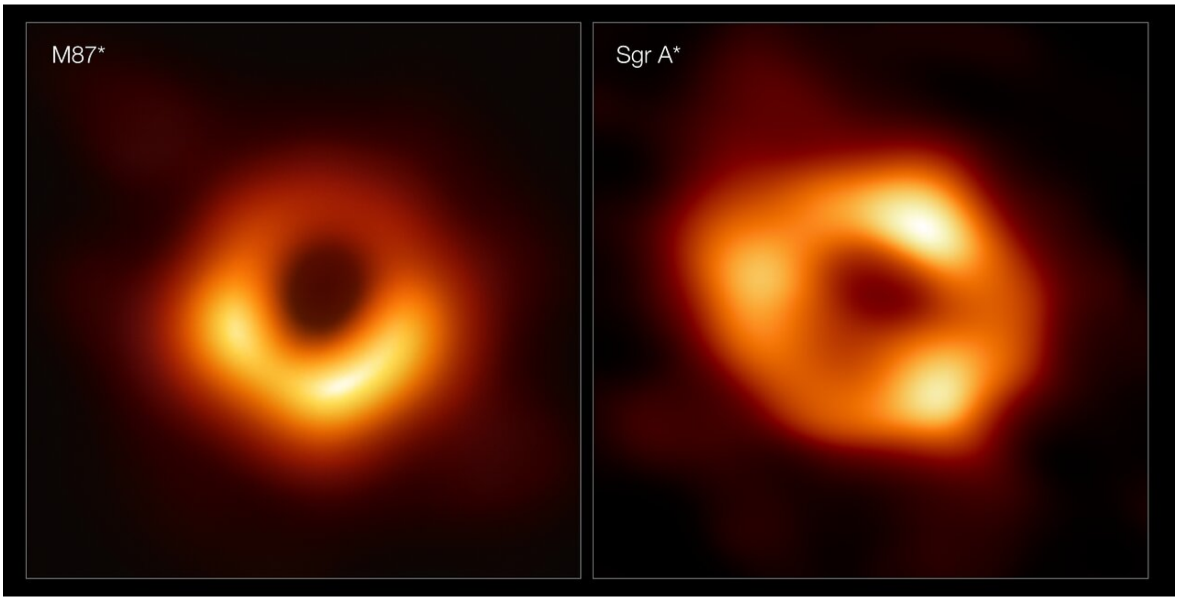

Figure 1.1: EHT images of M87* and Sgr A*. The central black region in both images corresponds to the black hole event horizon. The outer ring is gravitationally lensed radiation produced by the accretion of matter onto the black hole. See EHT Collaboration for further details on the interpretation of the two images. (Credits: EHT collaboration)

When the SMBH at the center of a galaxy is accreting the surrounding matter it visually manifests as an Active Galactic Nucleus (AGN[1]). It is now commonly accepted that the accretion of such matter is in the form of an optically thick, geometrically thin accretion disk, where viscous processes dissipate gravitational energy and angular momentum in the form of thermal radiation (Shakura and Sunyaev 1973, SS73 hereafter).

The primary emitted radiation can be so powerful that it outshines the whole stellar emission from the host galaxy. Moreover, emission from AGN is expected over the whole electromagnetic spectrum due to reprocessing by secondary components surrounding the SMBH (Padovani et al. 2017, P17 hereafter).

AGN are sources interesting on their own, as accretion is the most efficient spontaneous process in the universe for converting matter into radiation. Indeed the efficiency (η) for accretion onto a rotating black hole can be as high as $\eta = 0.42$, while the most efficient nuclear reaction, the conversion of hydrogen into helium is only efficient as

---

[1] The plural form of Active Galactic Nucleus is Active Galactic Nuclei. In this work we make use of the acronym “AGN” for both plural and singular cases.

$\eta = 0.007$ (Longair 2011). However, in recent years AGN have become of interest not only to accretion and black hole enthusiasts, but also to the galaxy evolution and cosmology communities. AGN are indeed thought to have a strong impact on the formation of structures and on the properties of the host-galaxy through “AGN Feedback” (e.g Harrison 2017).

In this Chapter, we present the basic ingredients and properties of AGN, their drastically variable subclass known as Changing-Look AGN, and the current theoretical and observational view of AGN feedback. Lastly, we present the source 2MASS 0918+2117 (2M0918), which is the subject of this work as it is both highly variable and caught in its active feedback phase.

1.1.1 Radiation from Disk Accretion

When matter spirals toward the black hole, angular momentum is dissipated due to viscous friction which heats up the particles. This thermal energy is then released as radiation from the optically thick disk. As the energy involved in the process is gravitational (U), we can express the luminosity L resulting from the accretion process as:

$$L = \frac{dU}{dt} = \frac{GM}{R}\frac{dm}{dt} = \frac{GM\dot{M}}{R} \tag{1.1}$$

where $G = 6.67 \times 10^{-8} cm^3 g^{-1} s^{-2}$ is the gravitational constant, M is the mass of the object generating the potential, R is the distance of the gas from the center of the object, and $\dot{M}$ is the rate at which matter is accreted. As $L = dE/dt$, with E being energy, we can also express the luminosity in terms of conversion of matter into energy, using the famous $E = Mc^2$ relation, by adding the efficiency factor η:

$$L = \frac{dE}{dt} = \eta \dot{M} c^2 \tag{1.2}$$

where $c = 2,998 \times 10^{10} cm/s$ is the speed of light. By combining Eq. 1.1 and Eq. 1.2, one can easily see that accretion is most efficient on the most compact objects ($\eta \propto \frac{M}{R}$).

Although this process can be very efficient ($\eta \sim 0.10$ for a standard black hole, and up to 0.42 for a rotating black hole), highly intense radiation fields produce strong radiation pressure P_{rad} which can counterbalance the gravitational force experienced by the particles in the gas. This phenomenon gives rise to the natural Eddington Limit, or Eddington Luminosity L_{EDD}. If the AGN luminosity is higher than L_{EDD}, accretion is halted altogether and gas outflows can arise. The Eddington Luminosity can be found analytically by equating, in module, the force experienced by ionized plasma due to radiation pressure $P_{rad}dA = L\sigma_e/(4\pi R^2 c)$, with σ_e being the electromagnetic Thomson cross-section, to the gravitational pull $F_{grav} = -GMm_p/(4\pi R^2)$, where $m_p = 1.67 \times 10^{-24} g$ is the proton mass. Solving for L and converting to units commonly used in extragalactic astrophysics ($1M_\odot = 1.99 \times 10^{33} g$, the mass of the Sun), the Eddington Luminosity can be expressed as:

$$L_{EDD} = 1.26 \times 10^{38} \left(\frac{M}{M_\odot} \right) erg/s \tag{1.3}$$

The Eddington Luminosity is a limit only dependent on the BH mass, from which it is straightforward that the brightest AGN, reaching $\sim 10^{45}$ erg/s, have to be therefore hosting the most extreme black holes in the universe. The luminosity of an AGN is often expressed in terms of the Eddington Ratio, $\lambda_{EDD} = L_{bol}/L_{EDD}$, where L_{bol} is the bolometric luminosity of the AGN. Accretion rates can span orders of magnitude in the AGN/SMBH population ($\lambda_{EDD} = 10^{-6} - 100$) and are also thought to be related to different types of accretion flows, other than the standard optically thick geometrically thick SS73 disk, which cannot explain the “Super-Eddington” sources accreting at $\lambda_{EDD} > 1$ (See Giustini and Proga 2019).

The bolometric luminosity L_{bol} is integrated on the whole electromagnetic spectrum, and takes into account the whole disk emission. In the next Section we discuss which additional components are thought to reprocess such radiation and what spectral signatures arise as a result of these processes.

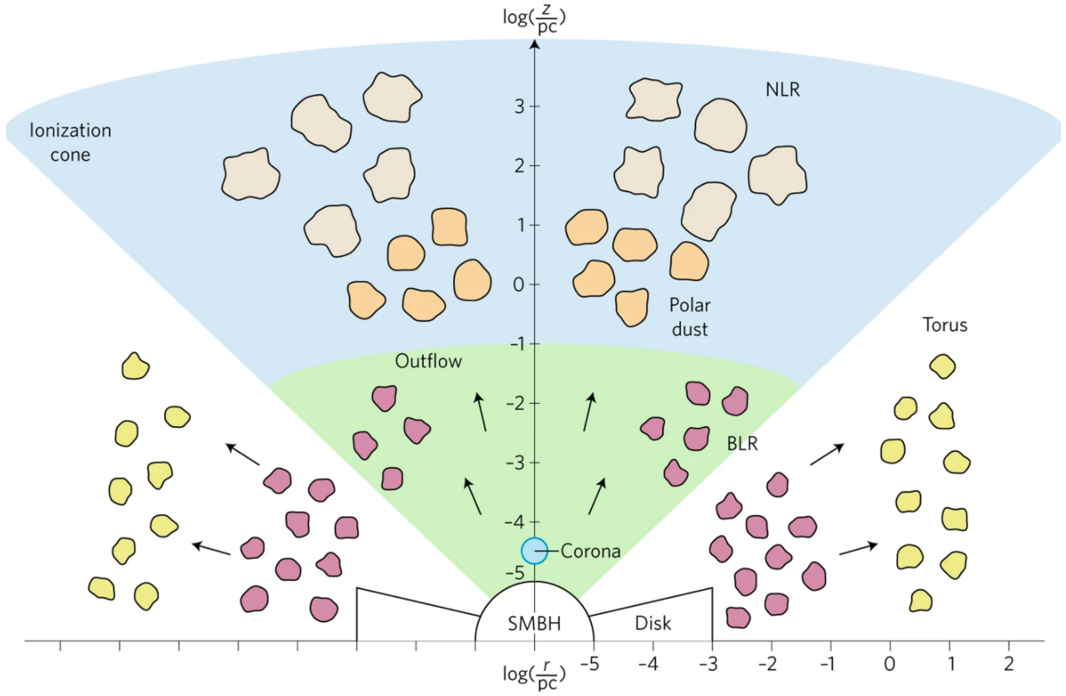

Figure 1.2: AGN Unified Model section view cartoon, from Ramos-Almeida and Ricci (2017). The different components in the picture are described in the text, and scales at which they are located for an AGN with a SMBH of mass $10^8\ M_\odot$ are indicated by the distance parameters r and z on both axes.

1.1.2 The AGN Unified Model & Broad Band Emission

Although the details of the structure of AGN is are still an open question (See Netzer 2015 for a review), the general broad band emission of the bulk of the AGN population can be explained through the Unified Model paradigm (See e.g Antonucci and Miller 1985, Urry and Padovani 1995, and P17 for a recent review).

We will now describe the main components that constitute the Unified Model (of which a schematic representation also describing scales can be seen in Fig. 1.2), starting from the innermost regions of the AGN and moving outwards. As we also discuss the resulting emission, we assume a basic knowledge on radiation processes, for which the reader can refer to Longair (2011).

The Accretion Disk

The accretion disk is the source of the primary radiation emission of the AGN, and is confined to the innermost regions of the galactic nucleus, extending from $\sim 10^{-3}$ pc down to the "Innermost Stable Circular Orbit" (ISCO), the smallest possible radius for a circular orbit to be stable. The ISCO is of the order of 1 to 6 R_g (depending on the rotational velocity of the black hole), where $r_g = GM/c^2$ is the gravitational radius, which is equal to half of the Schwarzschild radius R_S. Any object with mass M confined to a region smaller than R_S is a black hole, and, although R_S should be derived in a relativistic framework, its analytic expression can be derived by investigating how compact an object should be for the Newtonian gravitational escape velocity to be equal to the speed of light ($R_S = 2GM/c^2$).

Although the nature of the accretion flow and disk geometry is still debated and not necessarily univocal in all AGN, the standard assumption is the geometrically thin and optically thick disk originally presented in SS73. In this context, the accretion radiation thermalizes due to the optical thickness of the disk, and the resulting emission is blackbody-like. As shown in Eq. 1.1, the energy released in the form of radiation is gravitational, and therefore dependent on the distance (R), therefore the total emission of the disk will be the superposition of blackbodies coming from different annuli, each with a temperature which increases with vicinity to the ISCO. This can be expressed by equating the Stefan-Boltzmann law $L \propto T^4$ to 1.1, thus $T \propto R^{-3/4}$. Typical temperatures of AGN accretion disks are of the order of 10^5 K, making the multi-color blackbody peak in the optical/UV.

The Corona

The X-ray emission of AGN is due to the reprocessing of the primary accretion emission by the so-called "Hot Corona", or simply Corona. The geometry, location, and properties of the Corona are still highly unconstrained and debated (e.g. Fabian et al. 2015, Ricci et al. 2018, Kang and Wang 2022), but in the general picture it can be described by hot ionized gas, with T up to 10^9 k and located within few R_g, above or around the accretion disk. As disk photons encounter the energetic plasma, they get upscattered through inverse-Compton processes from the UV to the X-rays. Because the primary emission is a superposition of multiple blackbodies, and the Corona is thermalized, the resulting emission will be a power-law with a high-energy cutoff

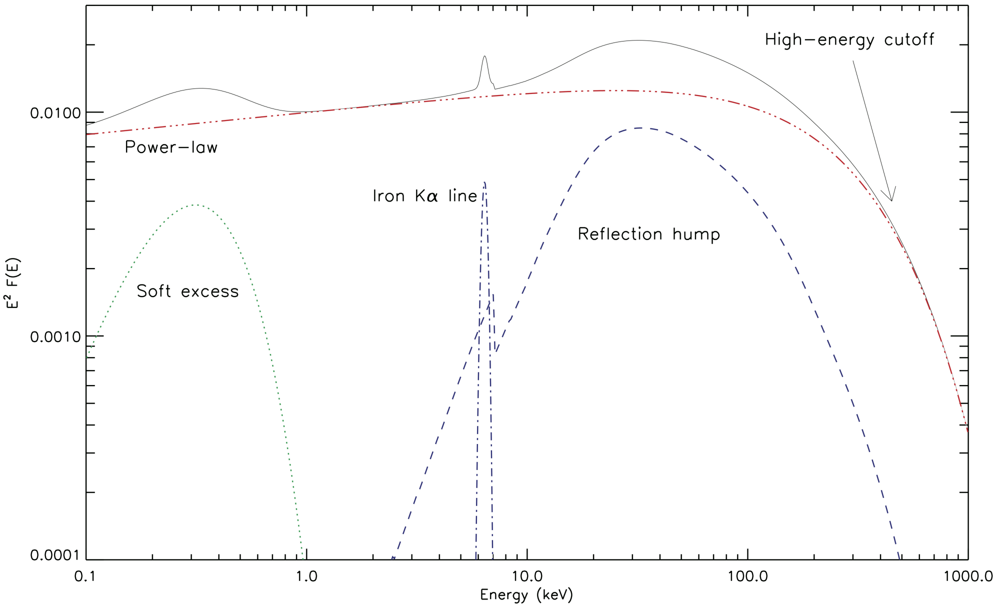

Figure 1.3: X-ray emission components of AGN, from Ricci 2011. The Power-law, Reflection hump and Iron Kα line components are described in the text, while the Soft excess isn't as its origin is uncertain and not thought to be due to the Corona /Disk (See Waddell et Al. submitted, for an extensive discussion on Soft Excess models.)

(See Fig. 1.3). Approximately half of the X-ray photons escape the AGN, while the remaining are scattered towards the disk. Low energy photons ($E < 10\ keV$) will be absorbed by the disk because of photoelectric effects, while photons above $\sim 40\ keV$ will be so energetic they penetrate deep in the disk before losing energy, and therefore will stay trapped and not be re-emitted. The photons with energies in between these two values will instead be reflected by the disk and reach the observer. The combination of these processes gives rise to the Compton or Reflection Hump, the green line in the aforementioned figure. The photons irradiating the disk will also give rise to fluorescence line emission, of which the most intense is the Iron Kα at $E \sim 6.4 - 7keV$, depending on the ionization state of the metals (blue line in Fig. 1.3).

The Broad Line Region

Surrounding the Disk, but still within sub-pc regions, gas clouds with densities of $n_e \sim 10^{9-10}$ cm^{-3} and temperatures of $T \sim 10^4$ K orbiting the SMBH give rise to the Broad Line Region (BLR). The name is due to the reprocessing by these clouds of the primary radiation into optical/IR emission lines, broadened ($FWHM > 2000\ km/s$) due to the fast Keplerian motions resulting from the proximity of the gas to the SMBH. The emission never shows forbidden lines, as the high densities suppress their emission due to collisional processes, while the temperature favors Balmer and Paschen emission.

The Torus

On ∼pc scale, and extending up to ∼100pc, the Unified Model predicts the presence of a dusty and molecular Torus component. Although its name originates from its first proposed geometry (that of a smooth-donut, Antonucci and Miller 1985) in more recent years a clumpy geometry has gained the consensus of the AGN community (See Fig. 1.3 and Ramos-Almeida and Ricci 2017). The dusty nature of the Torus makes it capable of suppressing the BLR, disk and soft-Coronal emission, making the hard ($E > 2\ keV$) X-rays the most suited band for detecting "obscured" AGN. The Torus is also responsible for the MIR emission of AGN, as the radiation it absorbs is re-emitted at lower energies/longer wavelengths.

The Narrow Line Region and the Type 1/Type 2 Dichotomy

Farther than the Torus, on scales up to hundreds of pc, we find the Narrow Line Region (NLR). At such distances Keplerian broadening becomes negligible, and the temperatures are similar to those of the BLR ($T = 10^{3-4}\ K$), but density is much lower ($n_e \sim 10^4\ cm^{-3}$, allowing narrow forbidden lines to be emitted from the gas, hence the name Narrow Line Region.

Because of the location of the NLR, the torus can never suppress the narrow line emission. This is thought to be the origin of the Type 1/Type 2 dichotomy: AGN are classified in the optical as either Type 1 or Type 2 based on the presence or absence, respectively, of BLR emission (See Fig. 1.4, *right*). The AGN Unified Model predicts that this effect is due to the viewing angle: if the source is seen "edge-on", the l.o.s towards the disk will intercept the Torus, which will suppress the disk and the BLR emission, resulting in a red, narrow line dominated optical spectrum. Instead, if the source is seen face-on, the Torus does not block out the primary and broad emission,

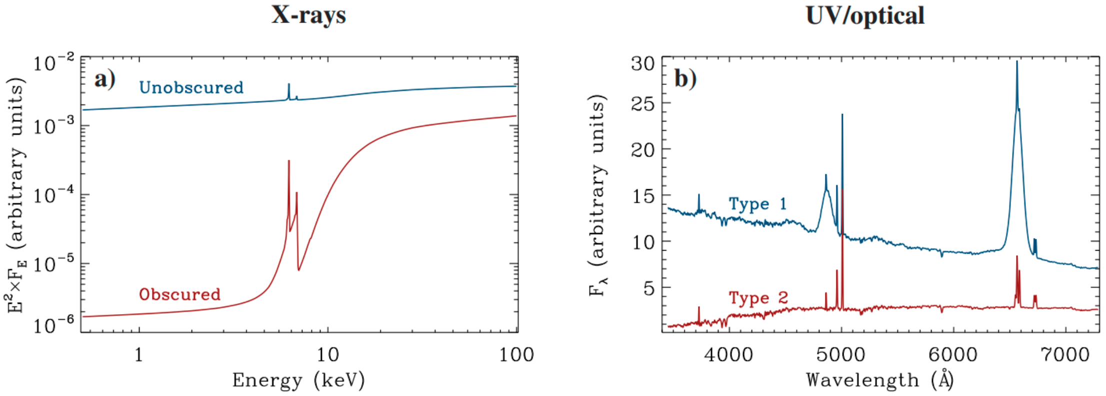

Figure 1.4: Typical Obscured vs. Unobscured and Type 1 vs Type 2 AGN spectra (adapted from Ricci and Trakhtenbrot 2022). In the Unified Model, the soft X-ray emission is suppressed when the torus intercepts the l.o.s towards the Corona. In the optical, the BLR emission is also suppressed in Type 2 due to the same reason. This is also supported by the redder continuum in Type 2 AGN.

giving rise to Type 2 spectra.

This dichotomy is also present in the X-ray as Obscured (line of sight column density $N_H > 10^{22}\ cm^{-2}$) vs. Unobscured (line of sight column density $N_H < 10^{22}\ cm^{-2}$). In this case, the torus absorbs soft X-ray photons, while highly penetrative hard X-ray photons reach the observer undisturbed (Fig. 1.4, *left*). The Iron lines are also more prominent in the obscured sources, as they are no longer outshined by the continuum emission.

The Unified Model can explain the overall shape of the AGN Spectral Energy Distribution (SED), shown in Fig. 1.5, as well as a plethora of AGN observations. However, it should be noted that not all type 1 AGN are unobscured, and not all type 2 AGN are obscured (e.g. Merloni et al. 2014). Moreover, some sources experience spectral transitions on timescales of months to years, hardly explainable as a change in the viewing angle (*Changing-Look* AGN, see next Section). The AGN Unified Model is therefore not the end of the story, and a clear picture of accreting SMBHs is far from being drawn.

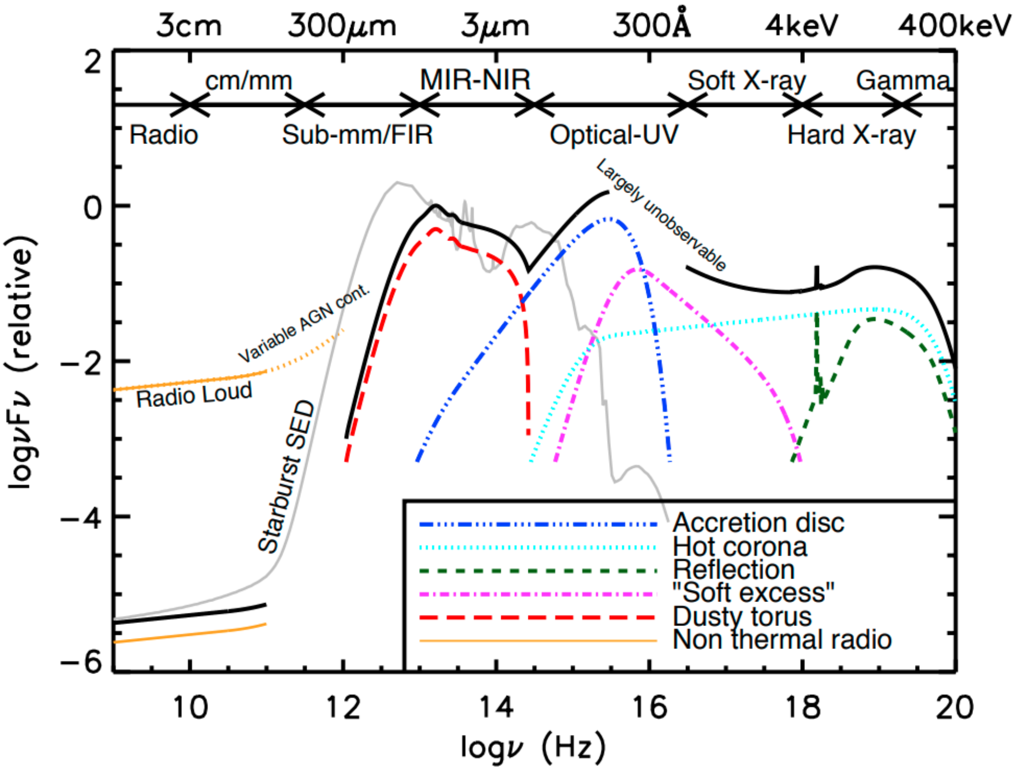

Figure 1.5: AGN broadband SED, from Harrison (2016). The accretion disk multicolor-blackbody peaks in the optical/UV band, while the torus reprocesses the primary emission in the Mid-Near Infrared (MIR and NIR). The Coronal-disk interaction produces the X-ray emission discussed in the previous sections, while the radio emission can be ascribed to stellar processes or Jets in the case of “Radio Loud” AGN, which we do not discuss in this work. The reader can refer to Blandford et al. (2019) for a review on Radio Loud AGN.

1.2 Variable & Changing-Look AGN

A defining characteristic of AGN is their variability, which is observed on all timescales (from minutes to decades, P17). The variability spectrum is red-noise-like, which means that higher amplitude variations are more likely on longer timescales, and, moreover, it is wavelength dependent, with faster variability happening on more energetic wavebands (X-rays). As it should be evident from the previous section, variability at different wavelengths traces changes in different components of the AGN. More in particular, variability in the X-rays can reflect changes in the structure or position of the Corona, changes in the column density in the line of sight, but also changes in the accretion disk, which is rapidly reprocessed by the nearby Corona.

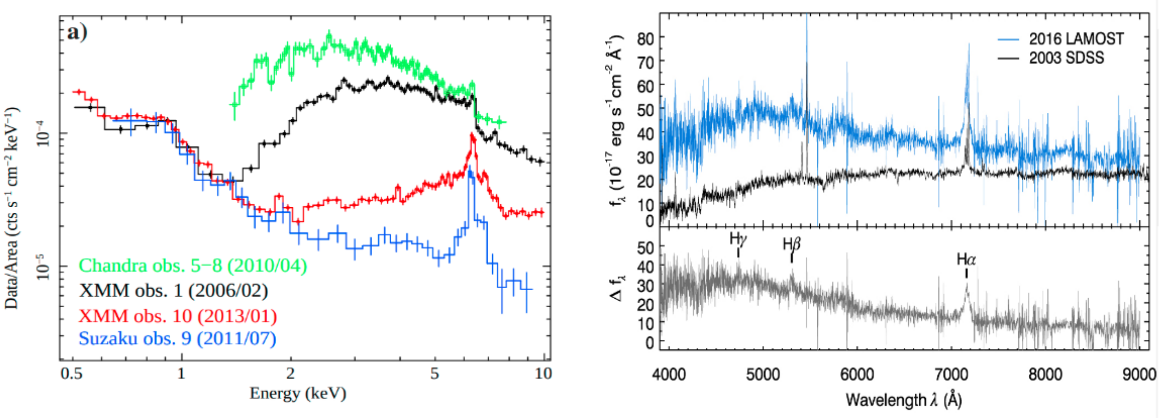

Figure 1.6: *Left:* X-ray spectral evolution of the AGN ESO 323-G771, showing transitions from Unobscured to obscured on timescales as short as 1 year (Miniutti et al. 2014). *Right:* Optical spectral transition in J1132+0357 which went from Type 2 to Type 1 over 13 years (selected from the sample presented in Yang et al. 2018). The bottom panel shows the residuals between the two observations, clearly revealing the appearance of a broad H_{α} emission line.

When variability is so drastic that the AGN transitions from one spectral type to another (Type 1 ↔ Type 2 or Unobscured ↔ Obscured) the AGN is said to be "Changing-Look" (CL-AGN, Ricci and Trakhtenbrot 2022). An increasing number of sources have been observed in recent years to undergo such transitions on timescales of months/years. which are hard to explain within the framework of the statical Unified Model. Two examples of these spectral transitions, both from an X-ray and from an optical point of view, taken from Miniutti et al. (2014) and Yang et al. (2018), are shown in Fig. 1.6.

The discovery of CL-AGN requires the expansion of the Unified Model, to include dynamic processes. These can take the form of accretion disk instabilities (e.g. Śniegowska et al. 2022), occultation events (e.g. Risaliti et al. 2007), or ignition/shutdown events of the central engine (e.g. Matt et al. 2003, Gezari et al. 2017). Investigating these sources can reveal powerful insights on accretion physics or on the dynamics of the nuclei of galaxies. We follow up on this discussion in Chapter 5.

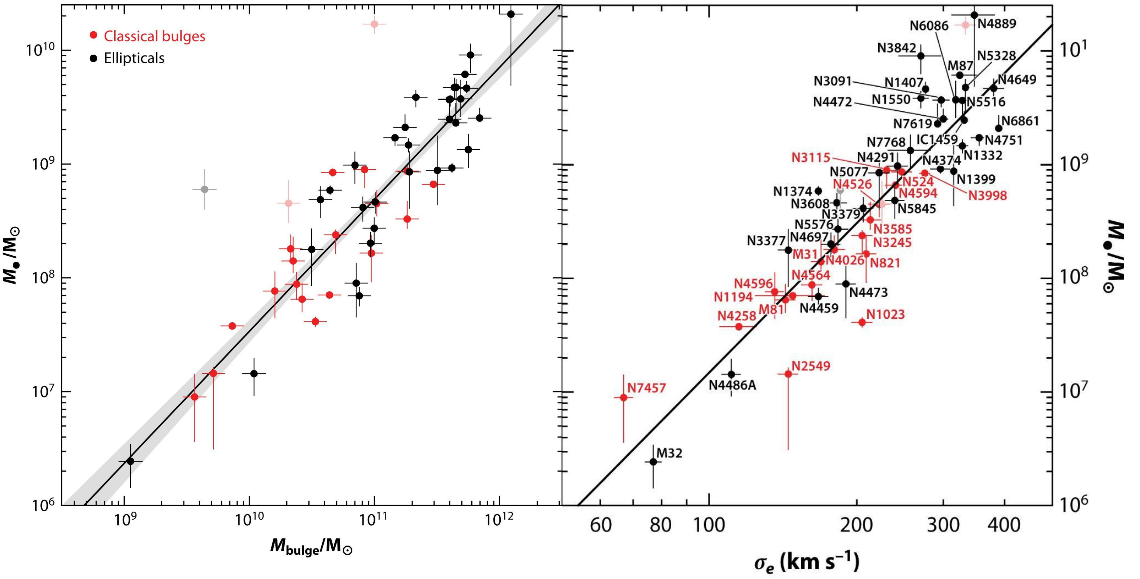

Figure 1.7: SMBH mass vs. bulge mass (*left*) and SMBH mass vs. velocity dispersion of stars (*right*) in elliptical galaxies and bulge components of star-forming galaxies. Adapted from Kormendy and Ho 2013.

1.3 Feedback from AGN

In the past 20 years, we have learned that galaxies know about the SMBH lying at their center, despite the gravitational sphere of influence of the black holes being usually confined below 100 pc. A striking example of how this manifests are the SMBH-Host scaling relations, such as the M-σ and the Black Hole Mass-Bulge Mass relations (See e.g Ferrarese and Merritt 2000, Gebhardt et al. 2000 and Häring and Rix 2004). These relations, which are shown in Fig. 1.7, reveal a tight trend between the masses of the central SMBHs and parameters of the bulge component of their host galaxies (such as the stellar velocity dispersion σ and the mass of the bulge itself).

Observational evidence such as this (e.g. Magorrian et al. 1998, and see Kormendy and Ho 2013 for an extensive review), as well as theoretical considerations (e.g. Silk and Rees 1998) have led the astronomical community to believe that the SMBH and galaxy assembly are connected, in the AGN/Galaxy Coevolution framework. In this context, the AGN, through its enormous amounts of energy emitted through accretion and angular momentum dissipation, can severely impact the gas reservoirs of the host galaxy, possibly quenching or triggering star-formation (See Harrison 2017 and references therein). AGN feedback is now included in most cosmological simulations (e.g. Di Matteo et al. 2005, Sijacki et al. 2015, Pillepich et al. 2021), as it is a necessary ingredient to prevent the formation of galaxies of extreme masses ($M > 10^{12-13} M_{\odot}$), which are indeed extremely rare in the universe.

A very promising way in which AGN can enact feedback on the host is through disk winds or outflows that propagate throughout the galaxy (e.g. Fabian 2012, King and Pounds 2015). In the following Sections, we describe the observational evidence on the multiple scales and phases in which these winds manifest and the theoretical predictions and open questions regarding AGN feedback.

1.3.1 Multi-phase signatures of AGN-driven winds

Winds associated with AGN activity have been observed on scales that range from sub-pc to 10s of kpc (Cicone et al. 2018 and references therein). As the Inter-Stellar Medium (ISM) of galaxies contains multiple phases of the gas, characterized by different densities and temperatures, and therefore different emission signatures, also the winds sweeping through the host will be observed on a multitude of phases.

Winds are usually revealed through emission or absorption lines that contain a blueshifted component, due to the proper motion of the outflowing gas (Fig. 1.8). These features have been observed on galaxy scales in the ionized (optical wavelengths), molecular (mm/sub-mm wavelengths), or atomic (radio) phases of the ISM, also with spatially resolved spectroscopy, which reveal complex interactions of the winds with the surrounding medium (e.g Gitti et al. 2006, Brusa et al. 2018, Cresci et al. 2023). The galaxy-scale outflows have typical velocities of $\sim 1000\ km/s$ (Fiore et al. 2017). Higher levels of ionizations are associated to winds closer to the central launching engine, the AGN. Broad absorption features in the soft X-rays and absorption lines above 7 keV ascribed to blueshifted Iron lines, respectively known as Warm Absorber (WA) and Ultra Fast Outflows (UFOs), trace such small-scale outflows. While warm absorbers also have velocities of $\sim 1000\ km/s$ and a range in ionization state, UFOs are characterized by high levels of ionization ($log(\xi) \sim 4$) and extreme, relativistic velocities (up to $0.3c$, Tombesi et al. 2010).

The detection of winds in one of the described phases is nearly ubiquitous, however, there are only a handful of sources for which multiphase and multiscale winds have been constrained (Tozzi et al. 2021). Simultaneously measuring outflow energetics on multiple scales is of crucial importance for constraining feedback propagation mechanisms, which will be discussed in the next section and are still an open question.

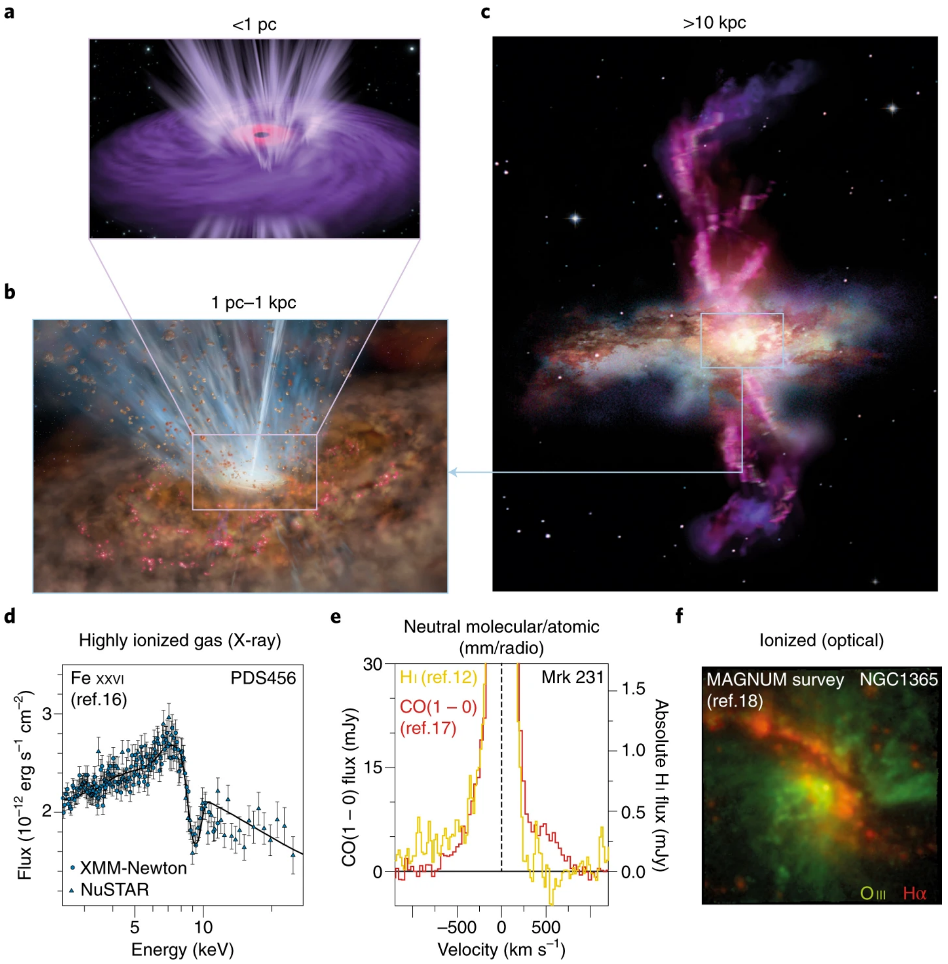

Figure 1.8: The multiple phases and scales of AGN winds (from Cicone et al. 2018). Panels a, b, and c are artistic representations of outflows from sub-pc to 10s of kpc scales. Panels d and e show the spectral features tracing respectively UFOs (PDS 456, Nardini et al. 2015) and atomic and molecular outflows (Mrk 231, Morganti et al. 2016, Cicone et al. 2012), while panel f shows spatially resolved outflows in the Ionized phase (NGC1365, Venturi et al. 2017).

1.3.2 The Physics of AGN-driven winds

The SMBH/AGN, despite not being able to gravitationally influence the entire host galaxy, is energetic enough to significantly impact the ISM. The black hole grew to its supermassive state largely through luminous accretion (e.g. Soltan 1982), of which the energy can be expressed as:

$$E_{BH} = \eta M c^2 \sim 2 \times 10^{61} M_8 \; erg \tag{1.4}$$

Where M_8 is the mass of the BH in units of $10^8 M_\odot$, and the accretion efficiency was assumed to be that of a non-rotating BH $\eta = 0.1$ (King and Pounds 2015). The Black Hole Mass-Bulge Mass relation found in Häring and Rix (2004) can be expressed as $M = 10^{-3} M_{bulge}$, where M_{bulge} is the bulge mass. The binding energy of the bulge component of the galaxy can be thus expressed in terms of the BH mass:

$$E_{bulge} = M_{bulge} \sigma^2 \sim 8 \times 10^{58} \sigma_{200}^2 M_8 \; erg \tag{1.5}$$

Where σ_{200} is the velocity dispersion of the stars in the bulge in units of 200 km/s. If the system lies close to the M - σ relation, and if we only consider the gas binding energy ($E_{gas} = f_g E_{bulge}$, with $f_g < 1$ is the gas fraction of the total mass), it is evident that the total energy associated to the mass build-up of the AGN greatly exceeds E_{gas}:

$$E_{BH} \sim 2000 E_{gas} \tag{1.6}$$

The AGN is therefore, in principle, fully capable of influencing the properties of the host.

As winds are launched, the UFOs produce a forward shock, sweeping through the ISM and generating multiphase outflows, while a reverse shock also forms and releases energy in the wind itself. Whether the energy is then radiated away or is stored in the wind is the origin of the momentum-driven vs. energy-driven wind propagation mechanism dichotomy (Fig. 1.9, Costa et al. 2014). If Compton cooling is efficient enough, the wind experiences significant energy losses and the impact on the ISM is

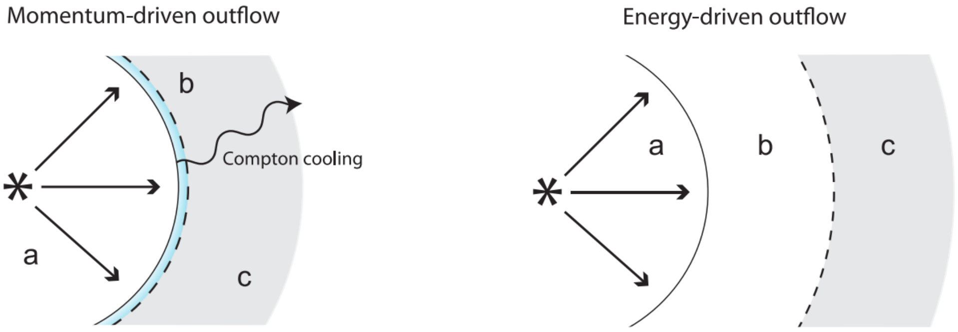

Figure 1.9: Momentum- vs. Energy-driven outflow propagation mechanism schematics, from Costa et al. (2014). *a* represents the launched wind, *c* is the ISM swept by the forward shock, while *b* is the wind that crossed the reverse shock. In the momentum-driven scenario, Compton cooling energy losses are significant, and *b* is thin, while the adiabatic expansion in the energy-driven scenario keep region *b* thick.

limited (momentum-driven scenario). Instead, if energy is conserved, the wind can expand adiabatically and significantly accelerate the ISM.

It's still not clear from theory which of these mechanisms is favored, and if a transition between the two is expected at certain radii. Observations can help in constraining which model is in act in AGN if multiphase outflows are observed, by measuring the momentum outflow rate $\dot{P}_{OF}$ and kinetic power $\dot{K}_{OF}$ of the winds:

$$\dot{P}_{OF} = \dot{M} v_{OF}, \qquad \dot{K}_{OF} = \frac{1}{2}\dot{M} v_{OF}^2 \tag{1.7}$$

where $\dot{M}$ is the mass ouflow rate, and v_{OF} is the velocity of the outflowing gas. The different ways these parameters are computed are illustrated in Chapter 3, while the way they are used to disentangle models is presented in Chapter 5.

1.4 The case of 2MASS 0918+2117

Given the number of open questions and the limited sizes of samples, both regarding CL-AGN and AGN where multiphase outflows are detected, single-object studies can be highly insightful. Detailed multi-epoch spectral analysis can provide constraints on the mechanisms responsible for the observed spectral transitions. Moreover, careful spectral modeling is needed in order to reveal outflows in sources that do not constitute the exceptional bright end of the AGN population.

2MASS 0918+2117 (2M0918 hereafter) is a bright, semi-local (z=0.149) AGN, located at RA = 09h 18m 48.61s, Dec=+21° 17' 17.07", originally discovered in the Two Micron All Sky Survey (2MASS, Cutri et al. 2002, Skrutskie et al. 2006). It is classified as Type 1.5, which is an intermediate optical class in which the narrow and broad H_β lines are comparable in flux (Osterbrock 1981).

It was the subject of three X-ray observations, in 2001 (with Chandra, Wilkes et al. 2002), in 2003 (with XMM-Newton, Wilkes et al. 2005) and in 2005 (with XMM-Newton, Pounds and Wilkes 2007, PW07 hereafter), which revealed very different spectral states (Fig. 1.10).

The 2001 Chandra observation did not show significant obscuration, while the 2003 observation appeared both fainter (factor $\sim$ 5) and harder, suggesting an increase in the column density in the line of sight. In 2005 the spectrum appeared 10x brighter than

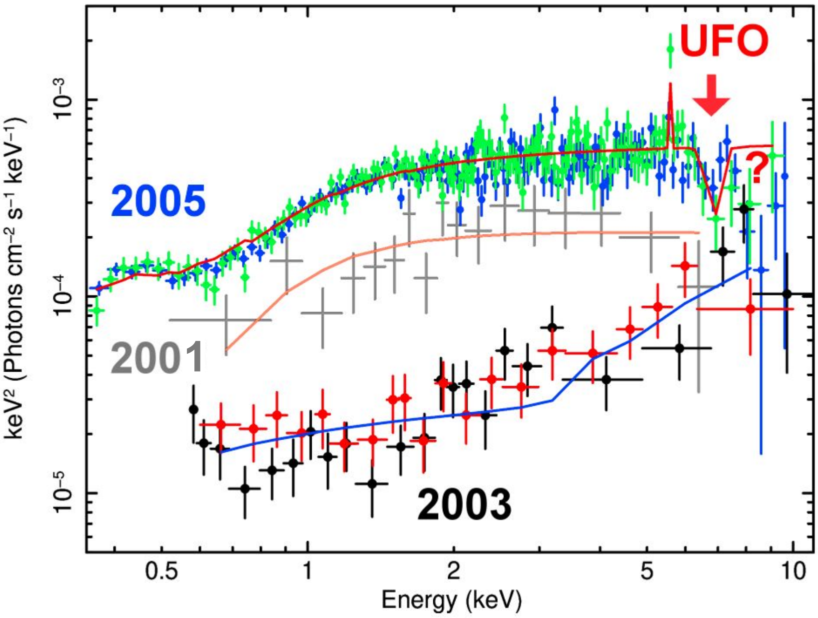

Figure 1.10: The X-ray spectral variability of 2M0918 (Courtesy of G. Lanzuisi). The source dimmed between 2000 and 2003 and re-brightened in 2005, with a flux increase of $\sim$ 1 order of magnitude. The 2003 observation also appears to be significantly harder than in the other observations, suggesting changes in the absorbing material. In the 2005 observation, an absorption feature above 7 keV suggests the presence of UFOs.

in 2003, and also much softer. PW07 ascribes the variability to be explainable in terms of changes in the intrinsic luminosity, tracing the accretion disk/Corona. However, the changes in the hardness of the spectra suggest that variable obscuration could also be at play.

PW07 also noted the presence of an absorption feature above 7 keV, which is interpreted in the work as tracing an Ultra Fast Outflow of $v_{OF} \sim 0.15c$, despite the evidence being tentative and the term “UFO” not being common in literature yet. The fact that this AGN is caught in its “active feedback” phase is corroborated by the presence of blue-winged emission line profiles in the 2005 SDSS optical spectrum, which indicate that ionized outflows are at play (See Chapter 3).

1.4.1 Aim of the Thesis

In this work, we shed light on the nature of the X-ray variability of 2M0918, as well as characterize the multiphase and multiscale winds of which previous studies show evidence. In order to characterize the UFO we make use of dedicated follow-up XMM-Newton and NuSTAR X-ray observations, obtained in 2020 (P.I: G. Lanzuisi), with a total exposure time of $\sim 100\ ks$. The ionized outflows will instead be studied with the publicly available SDSS optical spectrum.

In addition to the aforementioned spectra, we also analyze the data from the first 4 eROSITA all-sky surveys (2019-2021) in order to produce the 20-year-long spectrally derived X-ray lightcurve.

In the next Chapter we present the instrument used in this work, and in Chapter 3 we present the spectral analyses conducted to characterize the ionized winds and UFOs. In Chapter 4 we present the variability analysis and in Chapter 5 our conclusions and future perspectives.

In this work we assume ΛCDM Cosmology, with $H_0 = 69.6$, $\Omega_M = 0.286$, $\Omega_\Lambda = 0.714$. We also adopt a bolometric luminosity for 2M0918 of $L_{bol} = 2.23 \times 10^{45}$ erg/s, as extracted from SED-fitting through the software CIGALE (Boquien et al. 2019) by

Katia Gkmisi[2], as part of her Erasmus+ Internship at the University of Bologna.

Table 1.1 summarizes the most relevant parameters for 2M0918, including values derived from the SED fitting procedure. The modeled SED is shown in Fig. 1.11.

RA	09h 18m 48.61s
Dec	+21° 17' 17.07"
z	0.149
L_{bol}	2.23×10^{45} erg/s
M_*	7.45×10^{10} $M_\odot$
SFR	0.12 $M_\odot$/yr

Table 1.1: Summary of 2M0918 parameters. The bolometric luminosity L_{bol}, the total stellar mass M_* and Star Formation Rate (SFR) were all estimated from the SED fitting procedure.

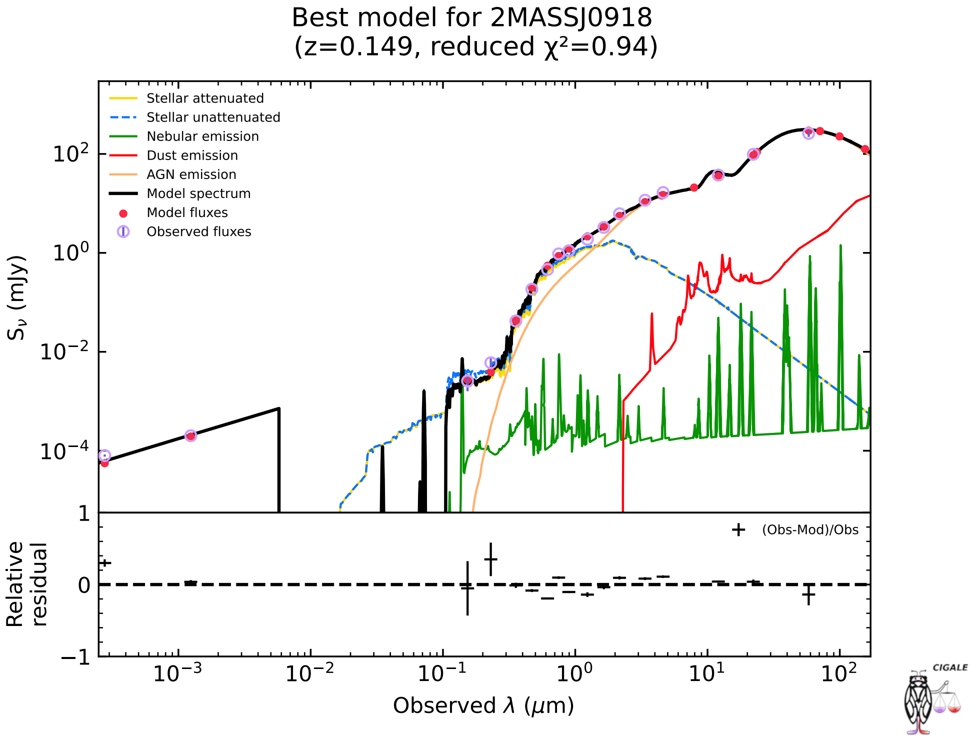

Figure 1.11: SED of 2M0918 as modeled with CIGALE, with residuals. As shown by the labels, the model includes templates for stellar, nebular, dust and AGN emission, as well as dust attenuation.

---

[2] https://www.researchgate.net/profile/Katia-Gkimisi

Chapter 2

Astrophysical probes: telescopes and instruments

The physical interpretation of observations can never be separated from the instruments through which the data are collected. The performance, parameters, and limitations of each telescope will always affect the kind of science that can be conducted with it, therefore in this Chapter, we report a comprehensive description of the instruments used in this Thesis.

2.1 X-ray Telescopes

X-ray photons are highly penetrative and therefore require different focusing techniques than lower energy electromagnetic radiation. Modern X-ray telescopes rely on grazing reflection, for which radiation that encounters a surface with an angle $\theta < \theta_c$ with respect to the surface, where θ_c is the *critical angle*, will be entirely reflected. This is depicted in Fig. 2.1, where the paths of different light rays crossing two different mediums with refractive indices n_1 and n_2 are shown.

For a photon of energy E and a mirror made of a medium with mean density ρ, it can be shown that $\theta_c \propto \frac{\sqrt{\rho}}{E}$. In other words, higher energy photons need heavier mirrors in order to be focused with the same incidence angle. Alternatively, the same instrument will focus lower energy photons more off-axis than higher energy ones.

Figure 2.2 shows a schematic representation of a typical focusing X-ray telescope (Wolter type, Wolter 1952), where grazing mirrors are typically nested to capture as much incoming light as possible.

Photons are then collected on the focal plane by a detector (usually a Charge-Coupled Device, CCD). As X-ray photons are not as numerous as in lower energy bands, the same CCD can be used for imaging, spectroscopy, and timing analysis simultaneously.

The following is a list of crucial X-ray instrumentation parameters:

- The photon collecting power of an X-ray telescope is called **Effective Area** (A_{eff}, with units $[cm^2]$), which is proportional to the projected mirror area A_{geom} corrected by factors depending on the incoming photon energy and angle (E,θ), and the position on the detector (x,y):

$$A_{eff}(E,\theta,(x,y)) = A_{geom} \times R(E) \times V(E,\theta) \times QE(E,(x,y)) \tag{2.1}$$

  The *reflectivity* $R(E)$ measures the fraction of photons that get reflected by the mirrors, while *vignetting* $V(E,\theta)$ accounts for counts losses as the off-axis angle increases. Lastly, the *quantum efficiency* $QE(E,(x,y))$ takes into account the fraction of photons that don't get registered by the detector.

- The pixel distribution of a point source illuminating the telescope is called **point spread function** (PSF), and is quantitatively represented by the **Full Width at Half Maximum** (FWHM) of a 2D-Gaussian, as such distribution only goes to zero at infinity. For reasons already discussed in this section, the PSF degrades the more off-axis the source, and is also dependent on the energy.

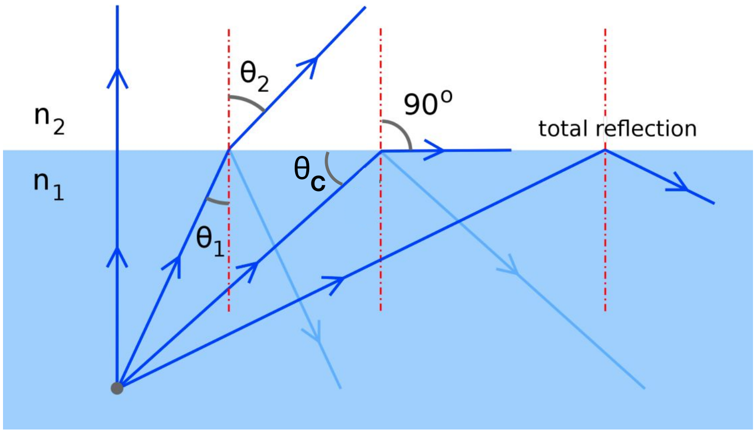

Figure 2.1: Paths of light rays encountering a refractive index discontinuity (from n_1 to n_2) with different angles. Once the rays are closer to being parallel to the surface than the limit set by the critical angle, all light is reflected. From Jfmelero (adapted by Gavin R Putland), CC BY-SA 3.0, via Wikimedia Commons.

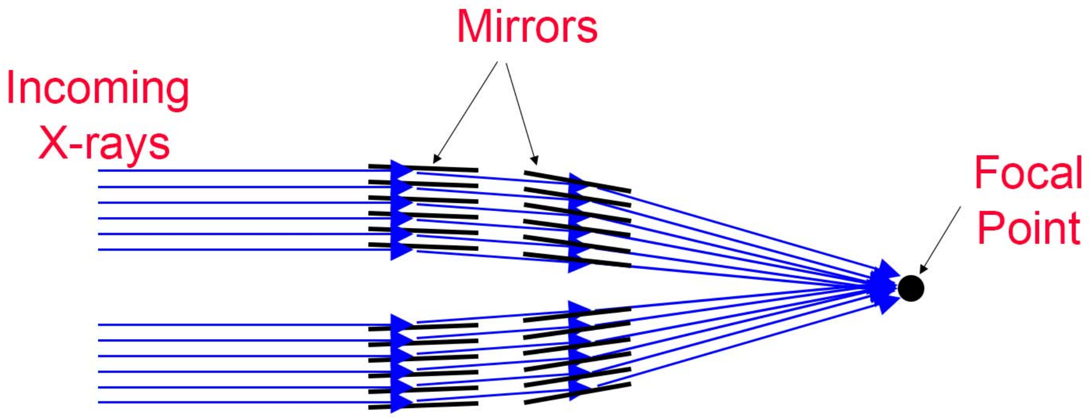

Figure 2.2: Diagram of a nested focusing Wolter-I X-ray telescope. (Credit: NASA's Imagine the Universe)

Similarly, the cumulative distribution of the energy captured at different radii for a point source is called **Encircled Energy Fraction** (EEF). The diameter at which EEF=0.5 is another quantifier of the PSF and is known as **Half Energy Width** (HEW).

- The **Spectral Resolution** of an X-ray telescope measures how finely the instrument is able to distinguish between different energy photons and is defined in terms of energy as: $E/\Delta E$.

- Lastly, the **sensitivity** of a telescope reflects how deep observations can go. This corresponds to the ability to reach a high *signal-to-noise ratio* (SNR), which can be expressed as:

$$\frac{S}{N} = \frac{S}{\sqrt{S+B}} \tag{2.2}$$

  where the noise is comprised of the sum of the Poissonian error of both source (S) and background (B).

A crucial aspect of X-ray observations is that the earth's atmosphere is opaque to X-ray radiation (Fig. 2.3), and therefore high energy telescopes need to be in space in order to measure astrophysical signals.

In the following Sections, we describe the X-ray telescopes used for this research: eROSITA, XMM-Newton, NuSTAR, and Chandra. These 4 telescopes constitute the state of the art for X-ray facilities. We chose to start with an extensive description of eROSITA, as it is the one with which the average reader is likely to be less familiar, while the remaining facilities are listed in order of 2M0918 observing time.

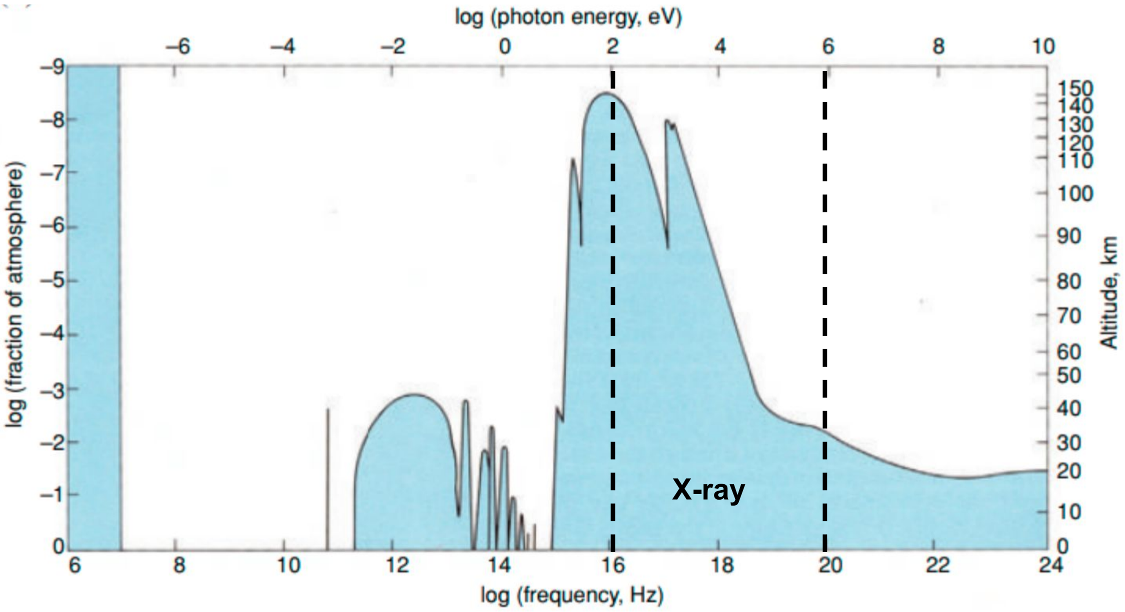

Figure 2.3: Altitude above sea-level at which the atmosphere becomes transparent to radiation as a function of frequency/photon energy. The X-ray band is indicated by the black dashed lines and is never transparent at ground level. (Adapted from Longair 2011).

2.1.1 eROSITA

eROSITA (extended ROentgen Survey with an Imaging Telescope Array, Predehl et al. 2021, P21 hereafter) is an X-ray telescope built by the German Max-Planck-Institut für Extraterrestrische Physik (MPE) and hosted on board of the Russian–German Spectrum-Roentgen-Gamma (Spektr-RG, Sunyaev et al. 2021) spacecraft, together with the Russian Astronomical Roentgen Telescope X-ray Concentrator (ART-XC, Pavlinsky et al. 2021) instrument. eROSITA has been designed to perform the deepest X-ray all-sky survey to date, expanding on the work of its German precursor ROSAT-XRT, which was operational in the 90s (Truemper 1993).

The telescope, illustrated in Fig. 2.4, is composed of 7 nested mirror assemblies (MA) with an outer diameter of 36 cm and a common focal length of 160 cm. Each MA contains 54 mirror shells. This results in a spatial resolution of 15” on axis (at 1.5 keV). On the focal plane of each MA is a CCD camera, which contains the entire 1 degree field of view (FOV).

The instrument detects photons between 0.2 and (nominally) 10 keV, with a sensi-

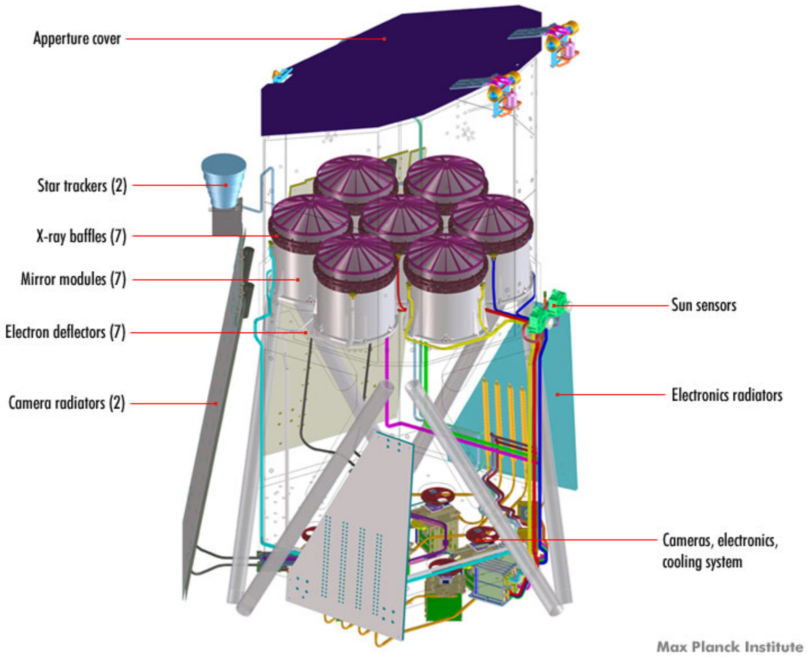

Figure 2.4: Schematic diagram of the eROSITA telescope structure (from Merloni et al. 2012). The 7 MA can be seen at the top, while the detectors are located at the bottom. The aperture cover, which is closed in the picture, is open during observations.

tivity 25x deeper than ROSAT in the 0.2-2.3 keV band. No X-ray instrument has ever performed an all-sky survey at energies above 2 keV prior to eROSITA.

The instrument was launched on 13 July 2019 from the Baikonur Cosmodrome in Kazakhstan on a Roscosmos mission and is currently performing a halo orbit (Fig.2.5) around the Lagrangian point L2 with a period of ∼6 months.

Such an orbiting strategy allows to scan the whole sky twice a year, performing therefore 8 eROSITA All-Sky Surveys (eRASS1 through eRASS8) in its 4 years predicted operative time.

The mission is designed to achieve 2 main scientific goals:

- Detect the hot gas in 50-100 thousands of galaxy clusters and in cluster filaments up to redshift $z \gtrsim 1$ to constrain the evolution of large-scale structures and cosmological parameters.

- Detect millions of new AGNs, both obscured and unobscured, both in the local and distant universe (up to $z \sim 6$).

In addition to this, the survey will provide unique samples to study the galactic population of X-ray sources (∼ few 100.000s are expected).

The survey strategy also allows for systematic variability studies as each part of the sky is observed at least once every six months for 100s of seconds each time, while exposure can be longer than 10 000 seconds in the Southern Ecliptic Pole (SEP) region (Fig. 2.6).

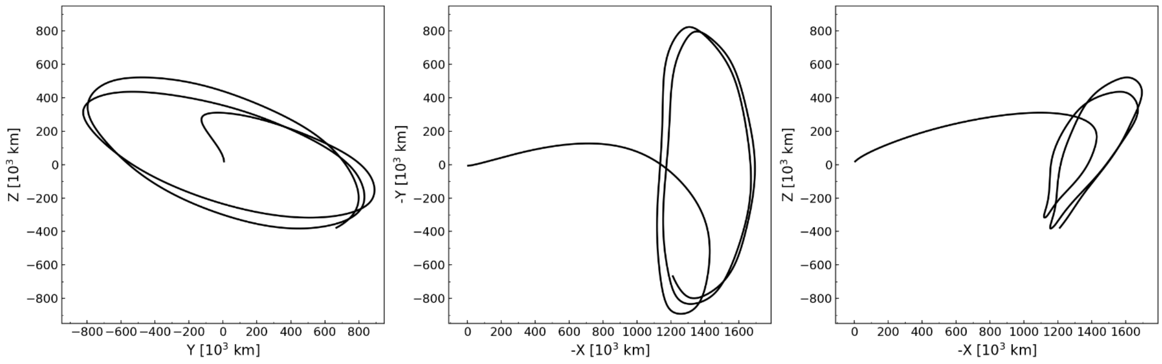

Figure 2.5: Projections of the first year eROSITA 3d halo orbit in Geocentric Solar Ecliptic coordinates (from P21).

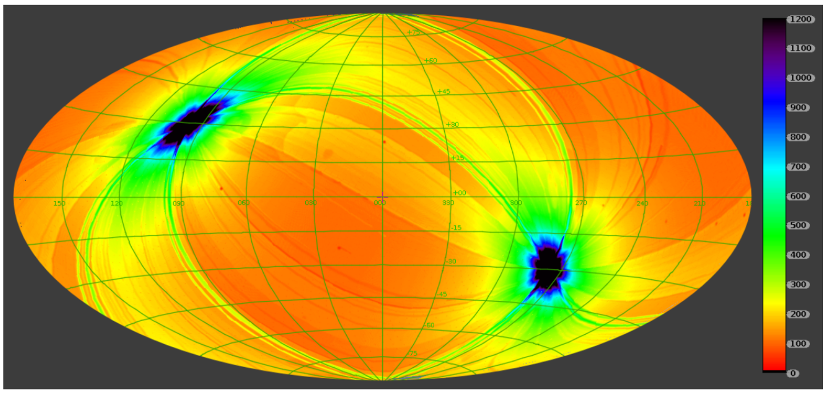

Figure 2.6: Vignetted exposure map of the first eRASS in galactic coordinates. The color bar refers to exposure times in seconds (from P21)

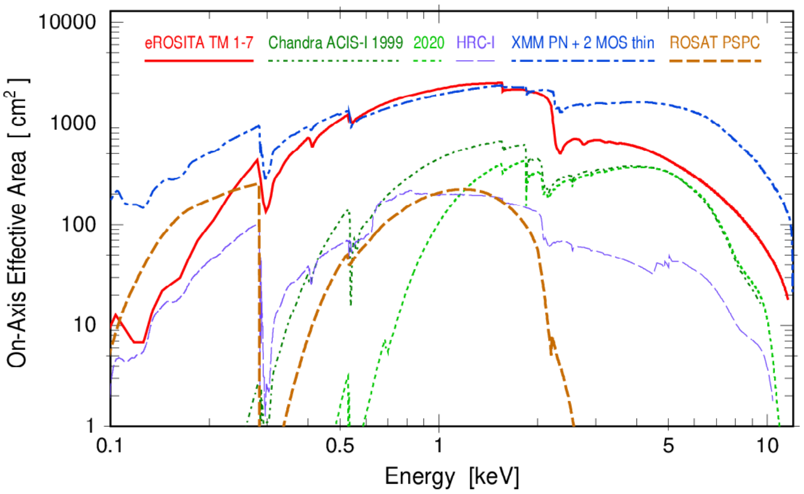

Figure 2.7: Comparison of the on-axis effective areas as a function of energy for eROSITA (red), Chandra-ACIS in two different years (1999 in dark green and 2020 in light green), XMM-Newton (blue) and ROSAT (yellow), from P21. Chandra's effective area has degraded over time in the soft band (see section 2.1.2 for more details), so it is insightful to compare how its performance has changed between early observations and current operations.

The eROSITA effective area of the 7 telescopes combined is plotted in Fig. 2.7 along with other relevant missions in the same energy bands. Between 0.5 and 2.3 keV the A_{eff} is comparable with the one of XMM-Newton (which is currently the instrument with the highest overall response), but it drops significantly in the hard band.

As of today eROSITA has completed eRASS1 through eRASS4 and was in the beginning of eRASS5 when the instrument stopped collecting data on February 26, 2022, as a consequence of the Russian invasion of Ukraine.

2.1.2 Chandra

The Chandra X-ray Observatory (Weisskopf et al. 2000, Fig. 2.8) is the X-ray telescope with the highest angular resolution to date (on-axis PSF HEW$\sim$ 0.5”). Built by NASA and launched on July 23 1999, it is still orbiting Earth and active, in spite of its 5 years of initial expected lifetime.

The optics consist of 4 nested mirrors with a focal length of 10m, which translates to deep sensitivity and low background impact, as the source photons are spread on a small area of the detector and so are less mixed with spurious signals. Figure 2.9 shows the radius at which different energy fractions are encircled as a function of photon energy. The dotted line, corresponding to EEF=0.5 corresponds to the HEW, which keeps sharp even at high energies.

In order to obtain such fine angular resolution while still being able to launch the telescope into space, the number of shells is lower than for other X-ray missions, as Chandra’s mirrors are large and heavy. This results in a compromise in the effective area, which is the smallest of all the ones shown in Fig. 2.7. Moreover, the effective area has degraded by a factor $\sim$ 10 at 1 keV since launch due to molecular build-up on

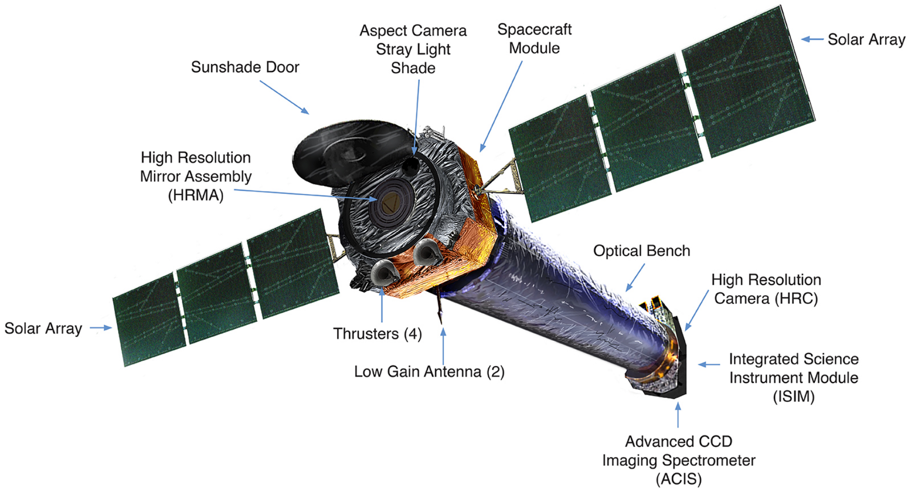

Figure 2.8: Schematic diagram of the Chandra X-ray Observatory. The detectors at the back of the instrument are connected to the High Resolution Mirror assembly by the 10m optical bench. The electrical power comes from the solar panels that extend like wings at the front of the instrument. Credits: NASA

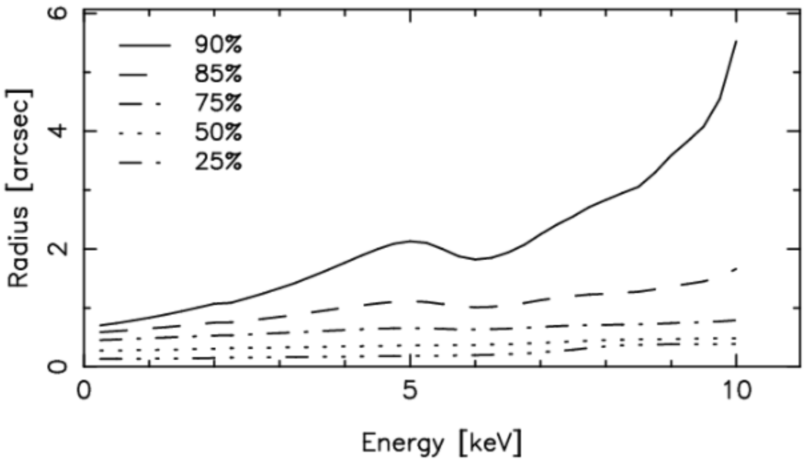

Figure 2.9: radius at which different energy fractions are encircled as a function of X-ray energy for an on-axis point source, from Chandra Main Proposer page.

the detector, which affects mostly the soft band. A comparison of the effective areas over 20 years can be seen in Fig. 2.7.

The main Chandra detector is the Advanced CCD Imaging Spectrometer (ACIS), which is composed of 10 1024x1024 pixel CCDs divided into two configurations: ACIS-I (2x2) and ACIS-S (1x6). Both have a mean spectral resolution of $\sim$ 100eV at 1 keV.

Chandra also hosts three other instruments: the High Resolution Camera (HRC) and the High and Low Energy Transmission Gratings (HETG and LETG), which are paired with ACIS, depending on the scientific Goal.

Chandra has produced the deepest X-ray survey to date, the Chandra Deep Field South (CDFS, Luo et al. 2017), where fluxes of $10^{-17} erg\ s^{-1}\ cm^{-2}$ in the 0.5-2 keV band were reached with 7Ms of exposure time.

2.1.3 XMM-Newton

Six months after Chandra, XMM-Newton was launched by ESA (Jansen et al. 2001, Fig. 2.10). The European mission complements Chandra, as its strongest asset is the large effective area (Fig. 2.7), which allows for high-quality spectroscopy in the 0.3-10 keV band. The telescope is elliptically orbiting the Earth, and its 5-year expected lifetime was extended like in the case of Chandra, so the instrument is currently still

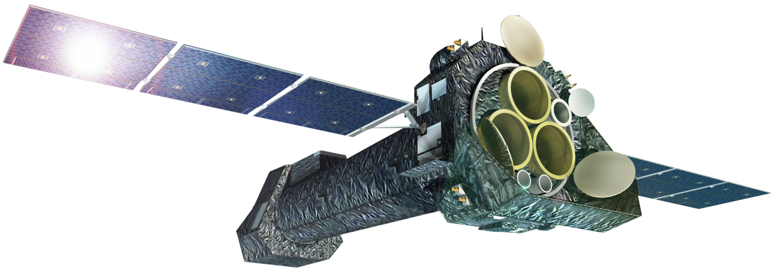

Figure 2.10: XMM-Newton spacecraft. The overall structure resembles Chandra's, but in XMM-Newton the three mirror modules are clearly visible in the front. From NASA Science Spacecraft Icons

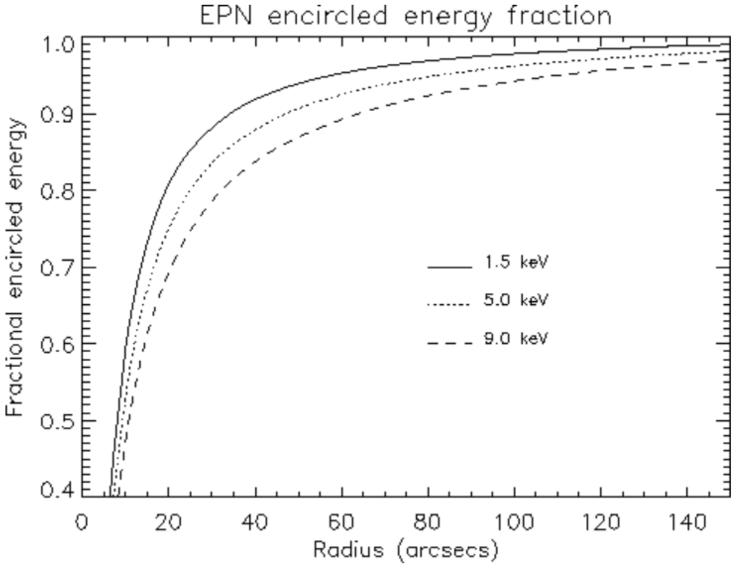

Figure 2.11: Encircled energy fraction of the EPIC-pn camera, as a function of radius, from XMM-Newton Users Handbook

operational.

The telescope's optics consist of 3 modules, each made of 58 nested shells, which provide an on-axis PSF of HEW $\sim$ 15", 30 times larger than Chandra. Figure 2.11 shows the EEF of the EPIC-pn camera as a function of radius for different energies. The HEW can be inferred from this plot similarly as in Fig. 2.9.

The most commonly used detector is the European Photon Imaging Camera (EPIC), which consists of three CCDs: pn, MOS1 and MOS2, each mounted at the focal plane of a different mirror module and therefore working simultaneously with each other. They offer a spectral resolution of $\sim 70-80$ eV at 1 keV, finer than Chandra's.

The telescope is also equipped with two Reflection Grating Spectrometers (RGS), which allow for high-resolution spectroscopy ($E/\Delta E \sim 200 - 800$). They are coupled with the MOS cameras and receive ~ 50% of the incoming photons. An Optical Monitor (OM), paired with an optical/UV camera, is also present and allows for simultaneous optical/UV and X-ray imaging, which is a unique feature of this telescope.

XMM-Newton and Chandra can be seen as complementary missions. NASA's telescope, thanks to its sharp resolution, allows for optimal imaging and for deep observations, while ESA's mission, thanks to its large effective area, is the best available in terms of spectroscopy.

2.1.4 NuSTAR

The Nuclear Spectroscopic Telescope Array (NuSTAR, Harrison et al. 2013, Fig. 2.12) is the First focusing hard ($E > 10$ keV) X-ray telescope. It was launched 13 years later than XMM-Newton and Chandra, in June 2012.

As discussed in Section 2.1, in order to focus high energy photons (NuSTAR operates in the band 3-79 keV), the incident radiation must be almost parallel to the mirrors on which it impacts ($\lesssim 0.2°$). This translates to the need for heavy telescopes with long focal lengths, which are difficult to build and prohibitively expensive. However, NASA managed to solve this issue by connecting the optics to the detectors with an extendable mast with a full length of 10m, which was initially stowed during launch.

The optics consist of two modules of 133 thin mirror shells each, while the detectors, The Focal Plane Module(s) A and B (FPMA and FPMB) consist of 4 32x32 pixel CdZnTe detector arrays each, with a FOV of 13'x13' and a pixel resolution of ~12"/pixel. The detector's spectral resolution varies between 400 eV at 10 keV and 900 eV at 68 keV.

As the mast is not solid (see Fig. 2.12), background impact can be significant, and also dependent on the distribution of sources in the FOV, as it will further be discussed in Chapter 3.

NuSTAR's effective area maintains significant values up to its 79 keV band limit (Fig. 2.13), where AGN coronal's comptonization and extreme winds are visible.

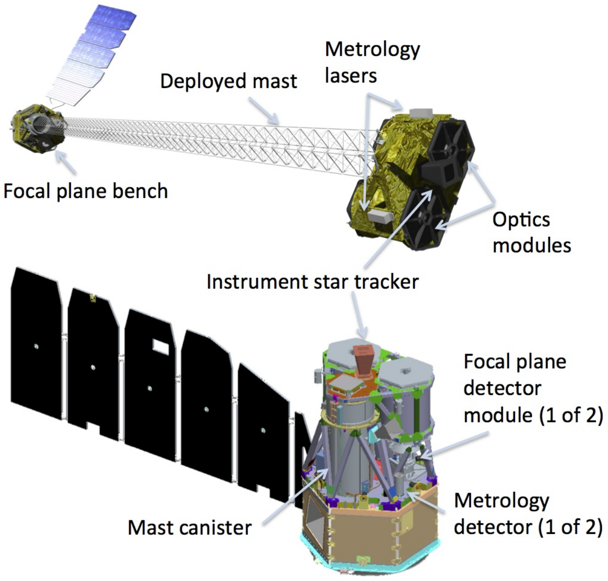

Figure 2.12: NuSTAR spacecraft schematics in launch position (below) and when deployed (above). The mast structure does not prevent stray light from seeping through and contributing to the background. From Harrison et al. 2013.

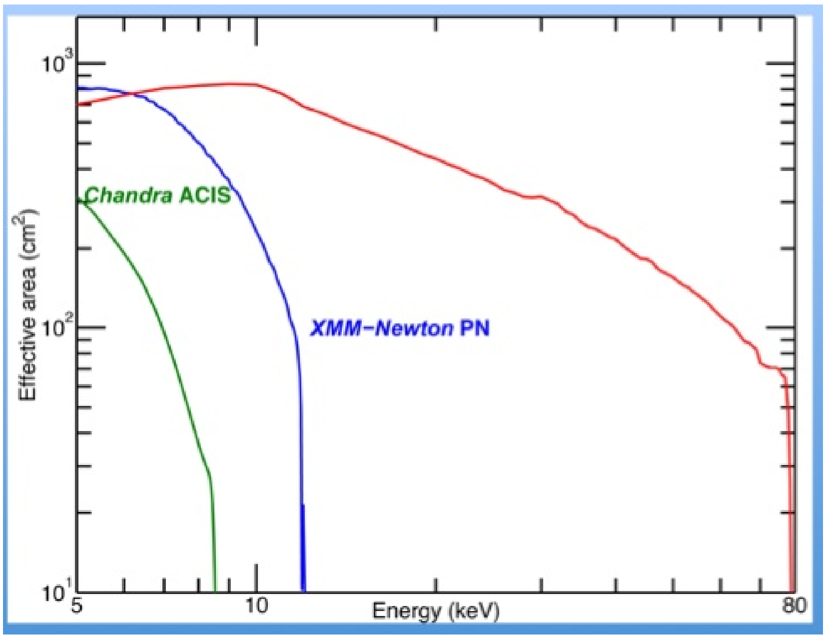

Figure 2.13: NuSTAR on-axis effective area (red), compared to XMM-Newton EPIC-pn (blue) and Chandra (green). From NuSTAR @ HEASARC

2.2 The SDSS 2.5m optical telescope

Optical telescopes differ from X-ray telescopes in the way that radiation is focused, as grazing incidence is no longer needed and parabolic/spherical mirrors are used instead. The detectors are still CCDs, although the number of photons that hit the telescope every second is so much higher than at high energies that it becomes impossible to individually register each one. Such high observation fluxes, together with the fact that the atmosphere is almost transparent to optical wavelengths (see Fig. 2.3), makes it very feasible to observe from the ground, although there are effects that need to be taken into account that would not be present in space (e.g. *telluric contamination*, *seeing* and *extinction*...).

The Sloan Digital Sky Survey (SDSS, York et al. 2000) is an optical imaging and spectroscopic survey with the aim of providing redshifts for a large number of extragalactic objects. This is done through a modified Ritchey-Chrétien telescope with an aperture of 2.5m ($f/5$) and located at the Apache Point Observatory in Sunspot, New Mexico (Fig. 2.14 Gunn et al. 2006).

The spectrograph changed over the year: before 2009, spectroscopy was performed through 640 3-arcsec diameter optical fibers, each encompassing a different object,

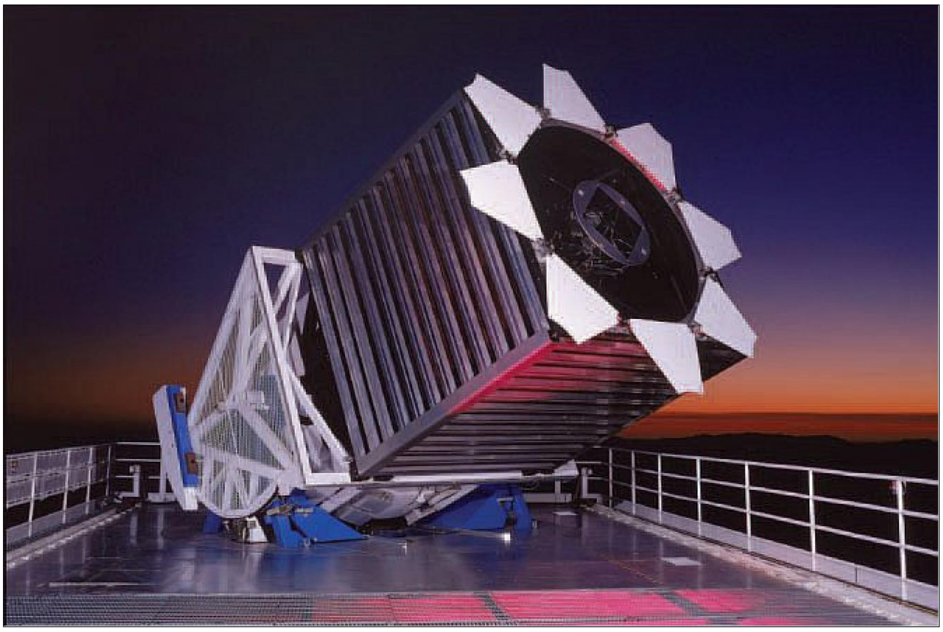

Figure 2.14: The SDSS 2.5m telescope, from Gunn et al. 2006

which then split the incoming radiations on two slit-spectrographs, with 2 2048 × 2048 pixel CCDs each as detectors, for a resulting wavelength range of 3800 to 9200 $\mathring{A}$ and a mean spectral resolution of $\lambda/\Delta\lambda \sim 1800$.

In 2009 a new spectrograph, called "BOSS", has been installed. BOSS consists of 1000 fibers of 2" in diameter covering the wavelength range 3600-10400 $\mathring{A}$ and a resolution of $\lambda/\Delta\lambda \sim 2000$.

The telescope is also equipped with a wide-field imager, with 24 2048 × 2048 CCDs as detectors, that cover the sky in the 5 filters *u,g,r,i,z*.

*

In this work we study the ionized winds of 2M0918 through the publicly available SDSS optical spectra, and characterize the UFO by combining XMM-Newton and NuSTAR observations, to ensure high SNR in the 7-15 keV band (Chapter 3). In order to investigate the nature of the variability in 2M0918, we analyze the X-ray spectra obtained with all of the aforementioned X-ray telescopes, covering 20 years with 8 observations (Chapter 4).

Chapter 3

The Multiphase and Multiscale Winds of 2M0918

In this Chapter, we illustrate our analysis of the multiphase winds of 2M0918. We first describe how we derived properties for the ionized outflow and the black hole in the 2005 SDSS spectrum, while in Section 3.2 we describe our method for detecting and characterizing sub-pc winds in X-ray spectra. The results from the X-ray spectral analysis we describe in this Section will also be preparatory to the variability analysis presented in the next Chapter.

3.1 Galaxy-scale Ionized Winds

SDSS observed 2M0918 on the 25th of November in 2005. The spectrum, shown in Fig. 3.1 along with the image of the source, reveals the clear presence of asymmetric forbidden/NLR lines, suggesting we might be observing an ionized gas outflow. In order to characterize the gas properties and kinematics, the spectral lines were fitted using the publicly available code PyQSOFit (Guo et al. 2018).

3.1.1 Spectral fitting

Following the prescriptions of Brusa et al. (2015), the following lines were fitted:

1. Eight narrow lines: H_α (6564.61 Å), H_β (4862.68 Å), and [OIII] (4960.30 & 5008.24 Å),[NII] (6549.86 & 6585.27 Å) and [SII] (6718.29 & 6732.67 Å) doublets. The FWHM was set to be < 550 km/s. The centroid offset was allowed to vary of only ~100 km/s with respect to the rest-frame wavelength ($z = 0.1495$)[1]. The

---

[1] we didn't use the redshift provided by SDSS, as it was computed using only one component for each line, which resulted in an underestimation of z. Instead, the redshift was estimated assuming that the peaks of the [OIII] doublets corresponded to the rest-frame emission

Ratios of the [OIII] and [NII] doublets were both set to be 1:2.99 from atomic physics. These lines account for NLR emission

2. Two very broad lines : H_α, H_β, with FWHM > 2000 km/s, to account for BLR emission.

3. Eight broad lines to account for outflowing components: the lines are the same as in (1), with the same constraints on ratios, however, the centroid and the width were allowed to vary freely.

As the code fits independently the H_α and H_β complex, we focus the rest of the analysis on the second region (H_β + [OIII] doublet) as it is more commonly used in literature for the characterization of outflows, in addition to being less affected by degeneracy (if our prescriptions are correct, the H_α complex would be composed of 7 blended gaussians). We constrain the velocity and the widths of the broad [OIII]s to be the same as the broad H_β, and the same is done for the narrow components.

The continuum model includes a polynomial component and FeII emission templates (Boroson and Green 1992). Galactic extinction is also included through the dust reddening maps by Schlegel et al. (1998).

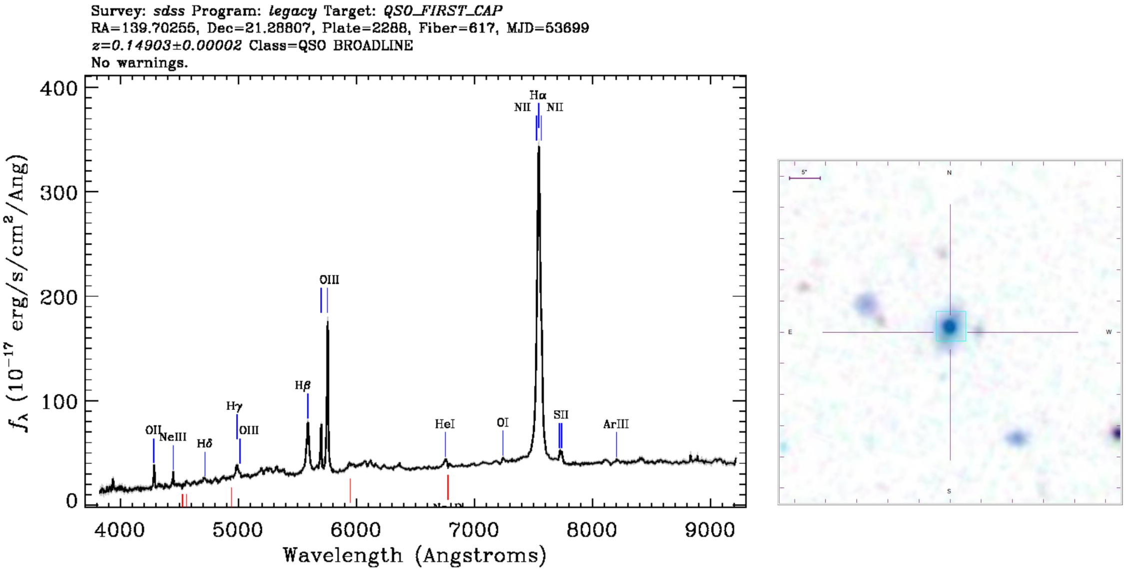

Figure 3.1: SDSS spectrum with identified lines, and image of the source as seen on SkyServer's Visual Tools

The results of the fit are shown in Fig. 3.2. As it's shown by the blue line in the plot, the outflowing component contributes significantly to line emission and is definitely needed to model the observed spectrum.

3.1.2 Gas Kinematics

In Table 3.1 are listed the properties of H_β complex lines (H_β and the [OIII] doublet). The ~ 3 Åuncertainties on the outflowing components centroids greatly affect the estimation of V_{OUT}.

The analysis of the gas kinematics was conducted following the methods used in Cano-Díaz et al. (2012), Fiore et al. (2017) (F17) and references therein. The mass outflow rate can be computed, assuming spherical geometry, through:

$$\dot{M}_{OF} = 3 \times v_{max} \times M_{OF} \times R_{OF}^{-1} \tag{3.1}$$

where v_{max} is the maximum outflow velocity, M_{OF} is the mass of the gas entrained in the outflow, and R_{OF} is the radius at which the outflow parameter is computed.

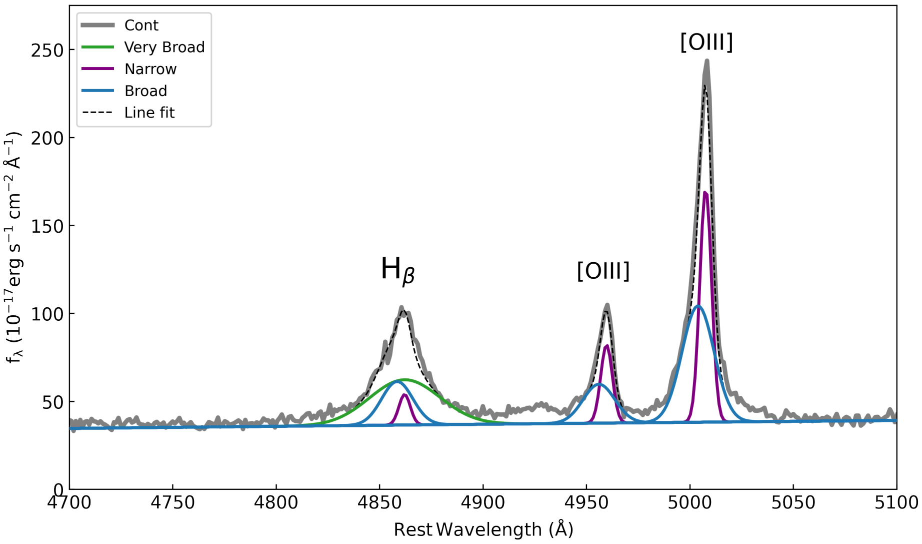

Figure 3.2: Best fit model of the H_β complex. The original dataset is shown in grey, while the total line emission is shown as the dashed black line. The purple lines account for NLR emission, while the green curve accounts for BLR emission from H_β. The blue lines, which are blueshifted with respect to the other emission components, are tracing the outflowing gas.

Line	Component	λ_{obs} [Å]	FWHM [km/s]	Flux [$10^{-17} erg/s^3$]	Velocity [km/s]
H_β	Very Broad	4862.1 ± 0.7	1828.2 ± 0.8	1095 ± 396	-35 ± 5
	Narrow	4861.4 ± 0.7	301.4 ± 0.1	119 ± 22	-78 ± 5
	Broad	4857.9 ± 0.2	809.7 ± 0.1	466 ± 76	-295 ± 14
$[OIII]_{4959}$	Narrow	4959.0 ± 0.1	307.4 ± 0.1	311 ± 14	-78 ± 5
	Broad	4955.4 ± 0.2	825.9 ± 0.1	424 ± 15	-296 ± 14
$[OIII]_{5007}$	Narrow	5006.9 ± 0.1	310.4 ± 0.1	941 ± 42	-68 ± 5
	Broad	5003.3 ± 0.2	833.9 ± 0.1	1281 ± 45	-296 ± 14

Table 3.1: Line parameters for the H_β complex. Errors are estimated through Monte Carlo flux simulations and are therefore of statistical nature. The many constraints make so the fit tightly converges to the above solution, and therefore the errors are very small.

Without spatially resolved spectroscopy R_{OF} can only be constrained as an upper limit. Knowing that the fibers on the SDSS spectrograph are 3" in diameter, the observed outflow is contained in a $\sim$ 3.9 kpc radius, as at z=0.1495 1" corresponds to a scale of 2.6 kpc.

M_{OF} can be estimated from the luminosities of $[OIII]_{5007}$ and H_β:

$$M_{[OIII]} = 4 \times 10^7 M_\odot \left(\frac{C}{10^{[O/H]}} \right) \left(\frac{L_{[OIII]}}{10^{44} erg/s} \right) \left(\frac{< n_e >}{10^3 cm^{-3}} \right)^{-1} \tag{3.2}$$

$$M_{H_\beta} = 7.8 \times 10^8 C \left(\frac{L_{H_\beta}}{10^{44} erg/s} \right) \left(\frac{< n_e >}{10^3 cm^{-3}} \right)^{-1} \tag{3.3}$$

where $L_{[OIII]}$ and L_{H_β} are the line luminosities, $\langle n_e \rangle$ is the average electron density of the ionized gas, $10^{[O/H]}$ is the metallicity of the same gas and $C = \langle n_e \rangle^2 / \langle n_e^2 \rangle$ is the "condensation factor" and can be assumed to be 1 in the simplified hypothesis that all clouds have the same average density.

We derived the electron density to be $n_e = 400$ cm^{-3} by measuring the ratio R = $[SII]_{6732}/[SII]_{6718} = 1.05$ (Osterbrock and Ferland 2006). Assuming solar metallicity and neglecting systematic errors intrinsic to the derivation of 3.2 and 3.3, we obtain the following results:

- $M_{[OIII]} = 7.9 \pm 0.2 \times 10^5 \ M_\odot$
- $M_{H_\beta} = 6 \pm 1 \times 10^6 \ M_\odot$

M_{H_β} is 7 times higher than $M_{[\mathrm{OIII}]}$, but the ratio is compatible within 3σ with the average ratio of 3 reported in F17. From here on we only use the measurements derived for [OIII], as H_β was fit with one more component, which might increase degeneracies in line parameters and therefore be less reliable.

We use the common definition $v_{max} = \Delta V + 2\sigma$, where ΔV is the shift of the broad component centroid with respect to the centroid of the narrow, systemic emission line, and σ also refers to the outflowing component. From this we obtain the following velocities:

- $v_{max_{[\mathrm{OIII}]5007}} = 938 \pm 20$ km/s

We then estimate the mass outflow rate as:

- $\dot{M}_{OF} = 0.58 \pm 0.03\ M_{\odot}/\mathrm{yr}$

It is important to remember that R_{OF} was only constrained as an upper limit and therefore $\dot{M}_{OF}$ is a lower limit.

We then estimate the kinetic power $\dot{K}_{OF}$ and the momentum outflow rate $\dot{P}_{OF}$ as illustrated in Chapter 1.

- $\dot{K}_{OF} = (1.6 \pm 0.2) \times 10^{41}$ erg/s
- $\dot{P}_{OF} = (1.7 \pm 0.2) \times 10^{33}$ erg/cm

In Chapter 5 we discuss how these values compare to other literature results and what they tell us about the physics of feedback in 2M0918.

3.1.3 Black Hole Mass

A crucial information we can derive from optical spectra is the black hole mass. In order to infer such mass, we apply the well-established Single Epoch Virial method (SEV), which is based on the empirical $R_{BLR} \propto L^{0.5}$ relation discovered through reverberation mapping studies (Kaspi et al. 2005). In this method, by assuming that the BLR is virialized, the FWHM of broad lines can be used as a proxy of rotation velocity, while the continuum luminosity is a scale indicator, as stated above. This gives us:

$$log\left(\frac{M_{BH}}{M_\odot}\right) = A + B\ log\left(\frac{\lambda\ L_\lambda}{10^{42}\ \mathrm{erg/s}}\right) + 2log\left(\frac{FWHM}{1000\ \mathrm{km/s}}\right) \tag{3.4}$$

Where A and B are constants and λL_λ is the luminosity calculated at λ. At low redshift the most commonly used lines are H_α and H_β. As discussed before, the H_α complex is too blended in order to have a solid estimate on the broad line parameters, therefore we use the FWHM of H_β and estimate the continuum luminosity at $5100\mathring{A}$. Following the prescriptions of Greene and Ho (2005), we set A equal to 6.64 and B=0.64, which corresponds to a mass of $log(M/M_\odot) = 7.2$. The same authors find that the luminosity of H_β can also be used as a proxy of the continuum luminosity, as it correlates with $L_{5100\mathring{A}}$. When we implement this method (A=6.56, B=0.56) we measure a black hole mass of $log(M_{BH}/M_\odot) = 6.9$.

As both values are close to each other and of the order of $\sim 10^7\ M_\odot$, we measure the average value of $log(M_{BH}/M_\odot) = 7.1^{+0.1}_{-0.2}$. Some authors have argued that SEV mass estimates should come with systematic errors as large as 0.4-0.5 dex (See e.g. Shen 2013), therefore in the rest of this work we use the conservative estimate $log(M_{BH}/M_\odot) = 7.1^{+0.4}_{-0.4}$.

3.2 Accretion Disk-scale Ultra Fast Outflows

The first XMM-Newton observation in which signatures of absorption above 7 keV were first noted was performed in 2005 by Pounds and Wilkes (2007). As the feature was not significant, their study did not explore thoroughly such features. Moreover, the field of Ultra Fast Outflows was still in its infancy (first reported detection in Pounds et al. 2003). Motivated by the recent developments in the field, and by the presence of ionized outflow signatures in the optical SDSS data, we reanalyzed the 2005 observations and the dedicated 2020 XMM-Newton + NuSTAR observations (PI: Lanzuisi, G.), obtained in order to better assess the seemingly active feedback phase of this AGN.

3.2.1 The Data

We look for outflow signatures in both the 2005 and 2020 observations.

The 2005 observations had an exposure time of $\sim$ 21 ks, while in 2020 the exposure times were respectively of $\sim$ 57 ks for XMM-Newton and $\sim$ 61 ks for NuSTAR FPM modules.

The XMM-Newton and NuSTAR observations were taken 3 days apart - respectively on October 19th and October 22nd - but for the goal of establishing the broadband continuum shape we can consider them to be simultaneous. The primary power-law properties depend indeed on the accretion disk seed photons spectrum and the coronal parameters, which are expected to vary on much larger time scales. However, this is not the case for the wind signatures, which have been observed to vary in intensity/energy in a few tens of ks time scale (See e.g Giustini et al. 2011, Matzeu et al. 2017).

The observation log of the X-ray observations used in the search for winds in 2M0918 is presented in table 3.2

3.2.2 Data reduction

We now illustrate how the data were reduced respectively for XMM-Newton and NuSTAR.

ObsId	RA	Dec	Date	Exp. Time (s)
XMM-Newton				
0303360101	09h 18m 48.59s	+21d 17' 17"	2005-11-15	21806
0870820101	09h 18m 48.62s	+21d 17' 17"	2020-10-19	56999
NuSTAR				
60601008002	09h 18m 56.7s	+21d 19' 13" 2	2020-10-22	61970

Table 3.2: Observation log of the X-ray data used in the search for UFOs in 2M0918.

XMM-Newton

The EPIC Observation Data Files (ODFs) were reprocessed using the standard SAS procedures EPPROC and EMPROC, in order to produce calibrated event files (Fig. 3.3)

The pn, MOS1 and MOS2 spectra were then extracted by implementing a script that maximizes the signal-to-noise ratio (SNR) in the 2-10 keV band (Piconcelli et al. 2004, Bianchi et al. 2009). The algorithm works as follows:

- The background region and the source center position are fixed.
- Multiple source extraction radii are tested.
- For each extraction radius, multiple thresholds to filter out time intervals affected by background flares are tested. The one that maximizes SNR for that specific extraction region is then used.
- The combination of extraction radius and background filtering threshold which maximizes the SNR is then used for spectral extraction and analysis. For the 2005 observations we used extraction regions of 40", 30", and 40" respectively for MOS1, MOS2, and pn, while in 2020 we used 17", 20", and 15". The results of this extraction algorithm are plotted in Fig. 3.4.

We then binned the spectra using the optimal binning option (KB, Kaastra and Bleeker 2016) in the FTGROUPPHA task, contained in the HEASOFT package. Such binning scheme is variable based on the instrument's energy spectral resolution and number of counts, and allows to preserve both energy spectral resolution and SNR, which are equally crucial in the search for lines. As we are still in Poissonian regime, we use Cash-statistics (Cash 1979) instead of Chi-square for fitting purposes.

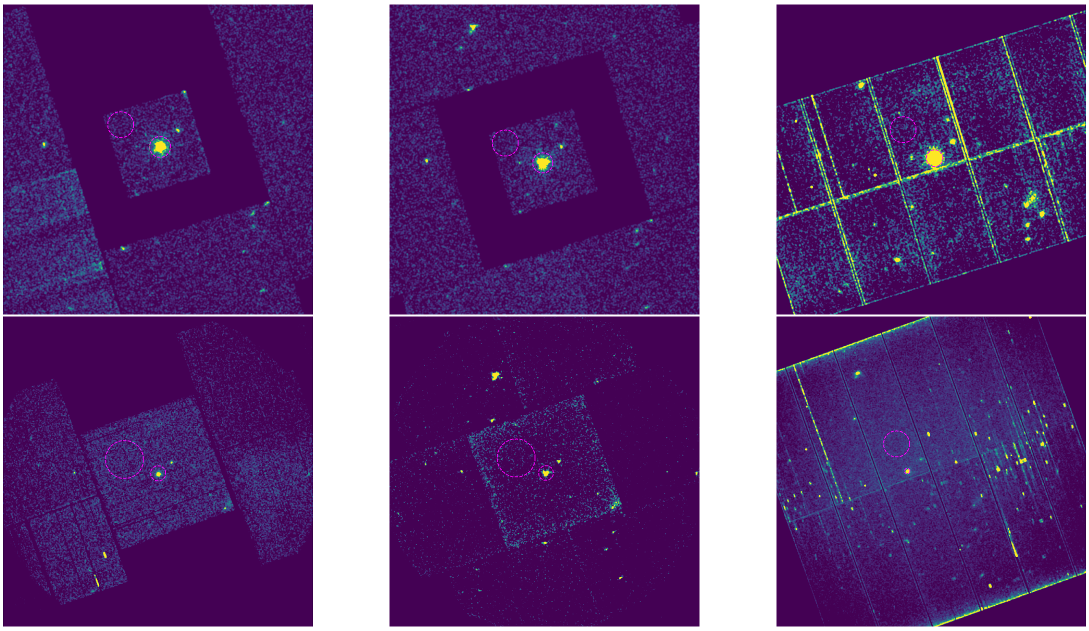

Figure 3.3: MOS1, MOS2, and PN smoothed images of the 2005 (above) and 2020 (below) observations. In magenta, the background extraction regions and the source extraction regions as determined from the algorithm described in this section. Note that some degree of variability is already noticeable in these images.

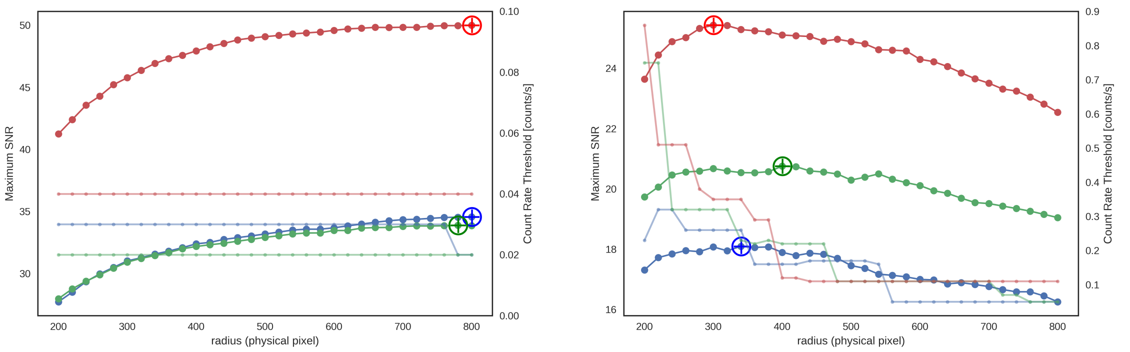

Figure 3.4: SNR (bold line) as a function of extraction radius in physical pixel (= 0.05 arcsec), for MOS1 (blue), MOS2 (green), and pn (red) for the count rate threshold that maximizes such SNR for that radius (thin line). The 2005 data (*left*) shows a steady increase, and the count rate threshold is very low. This is due to low particle flaring activity. The 2020 data (*right*) shows instead a behavior proper of data in which flares are not negligible. The best extraction regions are highlighted.

NuSTAR

As NuSTAR's optics are attached to the detectors by a mast that doesn't block out light, observations are not only affected by instrumental and cosmic background, as with XMM-Newton, but also by the photons that seep through and scatter over the structure of the spacecraft (the so-called *stray light*). This source of background is not spatially uniform because of the geometry of the instrument, which makes it hard to estimate the background at the source location. In order to solve this problem, we make use of the code NuSkyBgd (Wik et al. 2014), through which the gradient of the background was found by combining multiple concentric extraction regions (marked 1,2,3 in Fig. 3.5). The expected background at the source location (Magenta region, in Fig. 3.5) is then simulated. The source extraction region was 40" in radius, and the resulting spectra were used in Sect. 3.2.4.

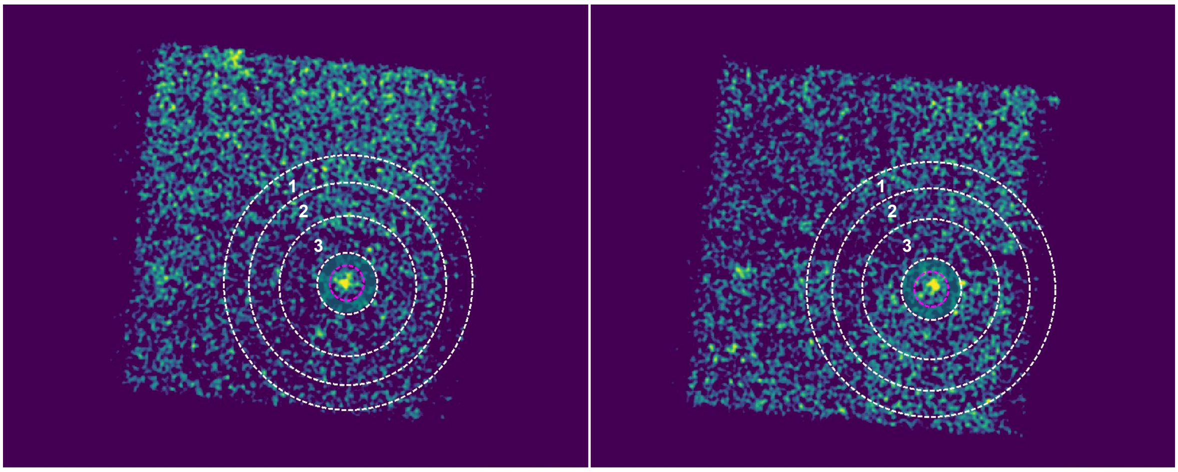

Figure 3.5: FPMA (*left*) and FPMB (*right*) images of the source, binned and smoothed, with background extraction regions (1,2,3) source extraction region (Magenta). As it's easy to notice, there is a gradient in the background distribution, due to the stray light.

3.2.3 Winds in the 2005 spectra

We re-analyze the 2005 spectra (Fig. 3.6), focusing on the search for hard X-ray absorption features. We do so with the Xspec spectral fitting package v.12.12.0 (Arnaud 1996) by first identifying the best continuum model, and subsequently looking for excess emission or absorption features with methods described in the following sections.

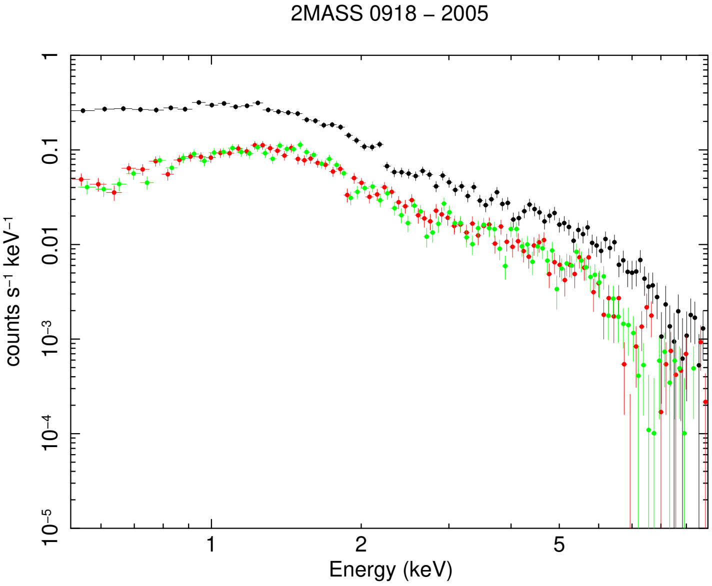

Figure 3.6: EPIC-pn (black), MOS1 (red), MOS2 (green) spectra in the 0.5-10 keV band, binned as in KB

Continuum spectral analysis

We first fit the three spectra simultaneously with a simple galactic absorption and powerlaw model (XSPEC: CONST[2]*TBABS*POWERLAW) between 0.5 and 10 keV, in order to model the continuum. We use a galactic absorption of $N_H = 3.6 \times 10^{20}$, as derived from the HEASOFT task NH (Kalberla et al. 2005).

The fit is very poor, with a C-stat value of 817 over 273 degrees of freedom (d.o.f.) The residuals, which can be seen in Fig. 3.7) show an excess of negative values below 1 keV and positive values in the 1-2 keV band, suggesting the need to add a restframe absorber in the model.

We then added a rest-frame, photoionized and partially covering absorber to the model (ZXIPCF) in order to better constrain the continuum. The residuals are less scattered (Fig. 3.7,b), and it's possible to already notice the presence of an emission line between 6 and 7 keV (source rest-frame), and absorption features above that.

The values of the fit parameters can be found in table 3.3. The fit C-stat value is 329 over 270 d.o.f. The value of the (lightly) ionized absorber's N_H is very mild, but it's

---

[2] When fitting multiple spectra the addition of a constant is needed in order to account for different instrumental normalization.

still of crucial importance for the fit. The ionization parameter, instead, is consistent with the absorber being not ionized, as it can be visualized through the contour plots in Fig. 3.8

This is our base continuum model for the rest of the following analysis.

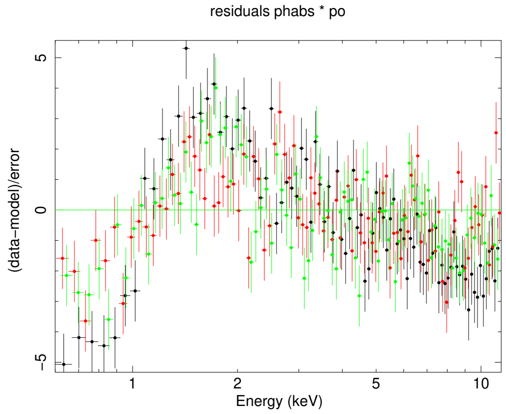

Figure 3.7: *a:* C-stat normalized residuals for the simple galactic absorption and powelaw model, color-coded as in Fig. 3.6. *b:* Same as *a*, but for the model that accounts for local (z=0.149) absorption. There now appear emission and absorption features above 5 keV. Both plots are shown with energy corrected for redshift.

Model Component	parameter	value	Lower error (1σ)	Upper error (1σ)
ZXIPCF	N$_H$	5.2×10^{21} cm^2	-0.1	0.1
	$log(\xi)$	-0.38	-0.54	0.19
	Covering fraction	0.84	-0.03	0.03
POWERLAW	Photon index	2.07	-0.07	0.07
	Normalization^a	5.8×10^{-4}	-6×10^{-05}	6×10^{-05}

Table 3.3: Values for best-fit continuum model. Notes: *a*: units for normalization are photons/keV/cm^2/s

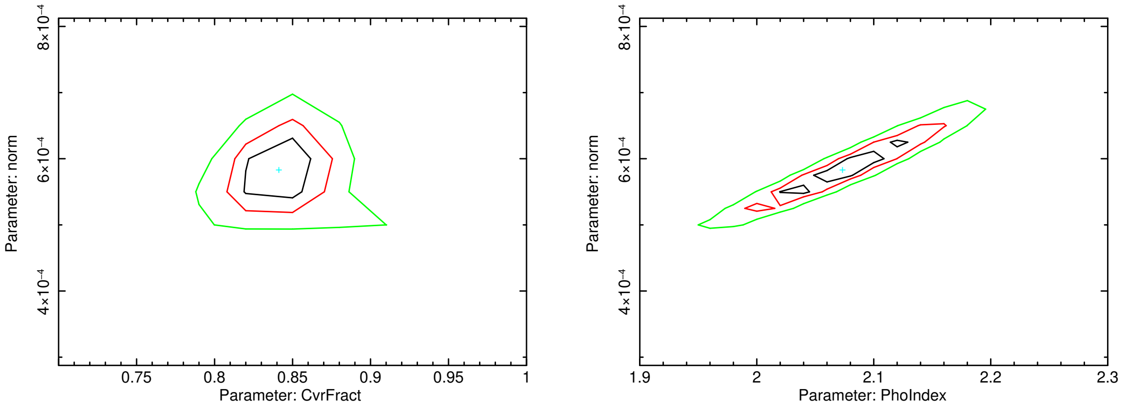

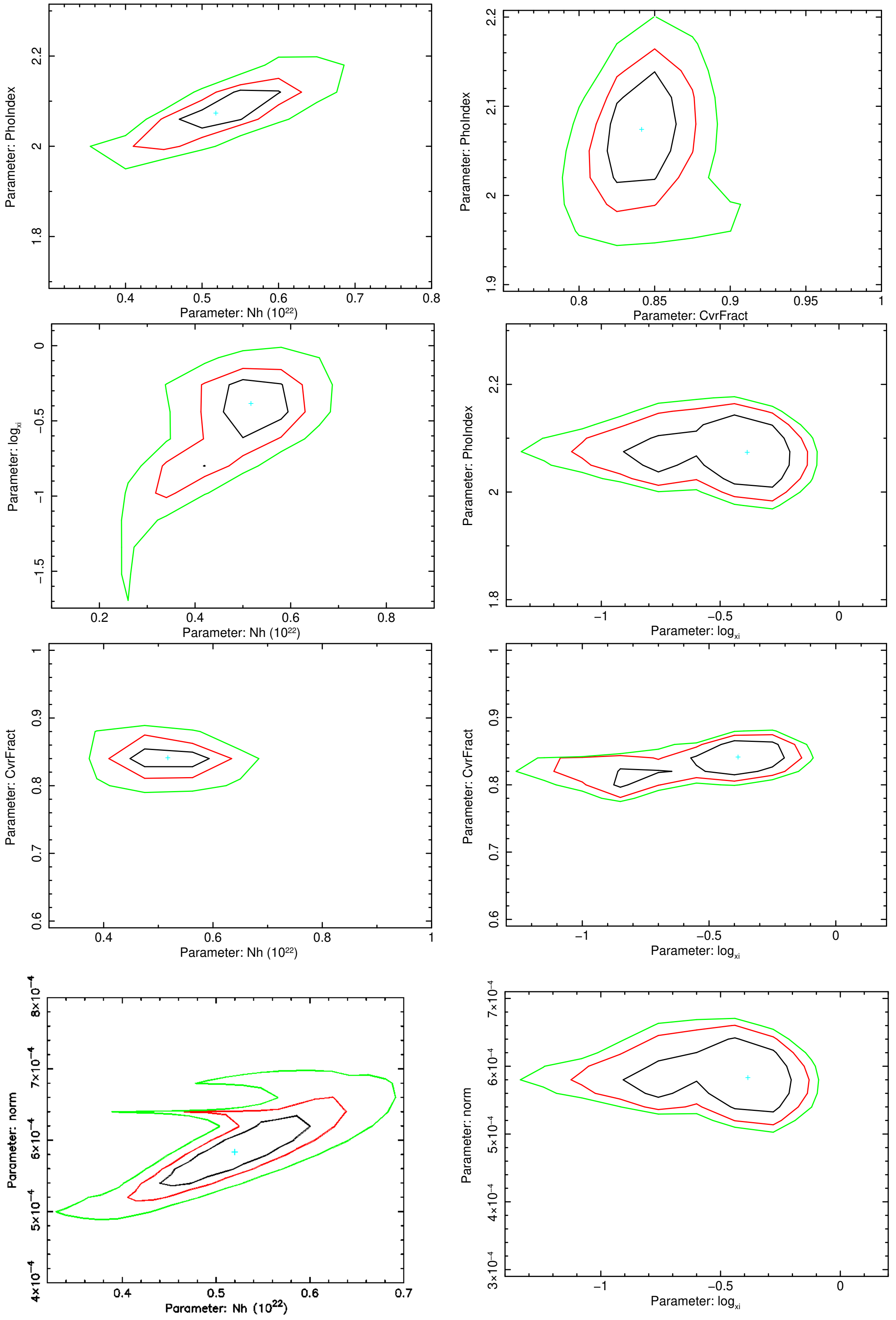

Figure 3.8: Contour plots for all variable parameters of the model summarized in Table 3.3. For $log(\xi)$ vs Photon Index and $log(\xi)$ vs Powerlaw Normalization, the contours represent 68% (black), 90% (red), and 95%1(green) confidence levels, while for all the other plots the green contour corresponds to 99 %. This is due to the fact that the ionization parameter is consistent with being zero, so $\log(\xi) \rightarrow -\infty$

Blind line search

We then proceeded to look for absorption and emission features, in order to detect Ultra Fast Outflow. We implement the well established "blind line search" method (See e.g Miniutti and Fabian 2006, Miniutti et al. 2007, Cappi et al. (2009)). The procedure operates as follows:

- The baseline continuum model is fit and its C-stat value is stored (see previous section).
- A narrow, unresolved line (XSPEC: ZGAUSS, with $\sigma = 10$ev) is added to the model, free to vary in energy and in both positive and negative normalization, to account for both emission and absorption features.
- Through the STEPPAR task, the line energy is shifted 100 times between 5 and 10 keV (rest frame), and, for each of these energies, normalization is allowed to vary both positively and negatively in ranges determined by the residuals, 100 times as well. The C-stat value of the fit of the continuum + each of these 100x100 combinations is stored.
- Contour plots are then produced for values of $\Delta\mathcal{C}$ of -2.3, -4.61, -5.99, -9.21, which correspond to 68%,90%,95%, and 99% confidence level fit improvement.

The resulting plot is to be read inversely compared to "regular" contour plots: inner closed lines indicate a higher significance of fit improvement.

As it can be seen in Fig. 3.9, there is a highly significant (99%) emission line around 6.4 keV source rest-frame, already suggested by the continuum model residuals (Fig. 3.7,b).

A slightly less significant (95%) absorption feature can be seen at ~ 9.1 keV, and an even less significant one (90%) is located at ~ 7.9keV

While it's easy to recognize the emission feature as an Iron Kα line, the absorption lines above 7 keV could be tracers of UFOs.

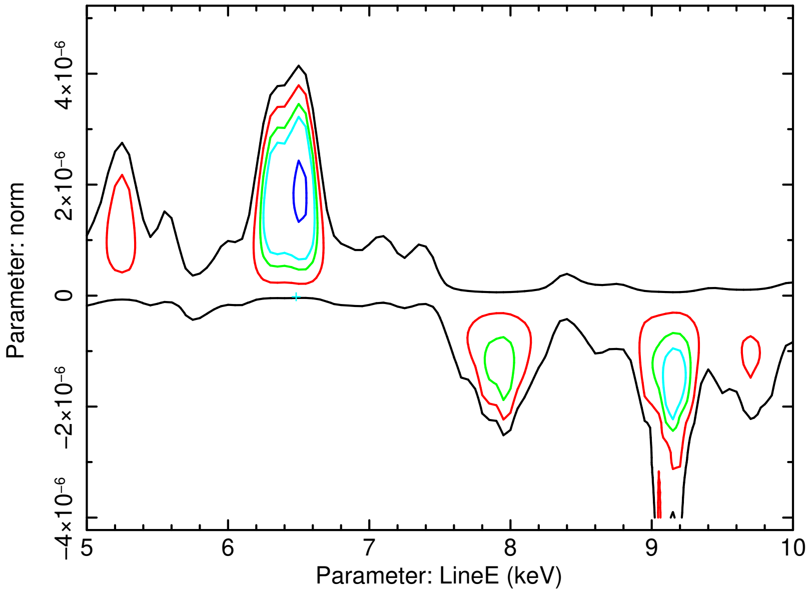

Figure 3.9: Contours produced in the 4th step of the blind search method. On the vertical axis are the line normalization values, and on the horizontal one the line energies in the source rest frame. The black line indicates no virtual improvement (~25 %), while, respectively, red, green, cyan, and blue correspond to 68%, 90%, 95% and 99% confidence level fit improvement. The black contour does not close around 9 keV can be ascribed to the interplay of background dominance and the presence of an absorption feature at that energy.

Iron Kα emission line

We fit a narrow (σ=10 eV) gaussian line over the continuum model at the energy of the emission line in Fig. 3.9 (~ 6.4 keV, source rest-frame). The guassian is centered at $E=6.5^{+0.1}_{-0.2}$ keV, with an equivalent width of 0.10 ± 0.05 keV. The new model has a C-stat value of 319 over 268 d.o.f., which gives an F-test significance of 98%. As this is a line compatible with known AGN lines (Iron Kα transition, E=6.4 keV, Fig. 3.10) we do not investigate further on the significance of the feature - despite the discussion in Protassov et al. (2002) - and we include it in the model.

Absorption lines

We then proceeded to fit the absorption features with gaussians with the same prescriptions as before. A line is found at $E=9.1 \pm 0.1$ keV, with a fit improvement with respect to the continuum plus line at 6.5 keV of $\Delta\mathcal{C} = 7$ over a Δd.o.f.=2, which gives an F-test significance of 95%. We note that the 99% line parameters contours don't close (Fig. 3.11,*right*), and are consistent with the line having normalization = 0.

If we move the initial value of the line energy towards the 7.9 keV feature seen in Fig. 3.9, the fit finds a new local minimum at E=8.0 $\pm$ 0.2 keV. However in this case the improvement is even less significant ($\Delta\mathcal{C} = 5$, F-test: 87%). In this case not even 95 % contours close (Fig. 3.11,*left*).

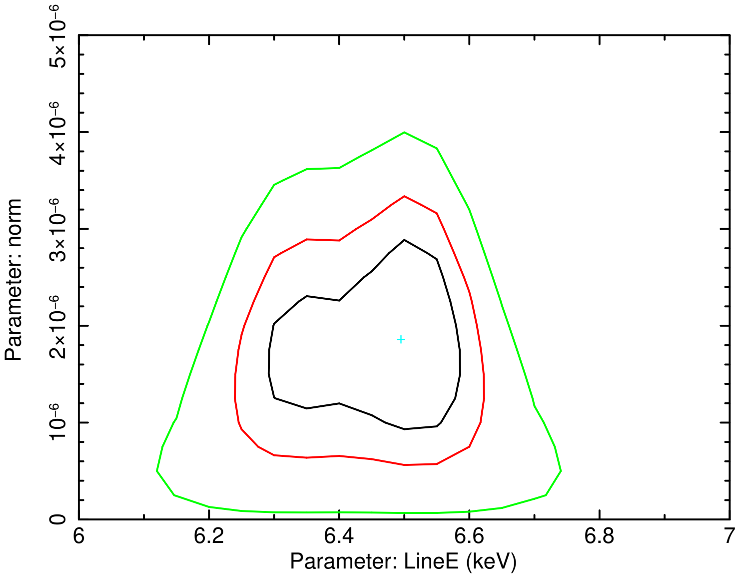

Figure 3.10: 68% (black), 90% (red) and 99% (green) contours of the 6.5 keV line parameters.

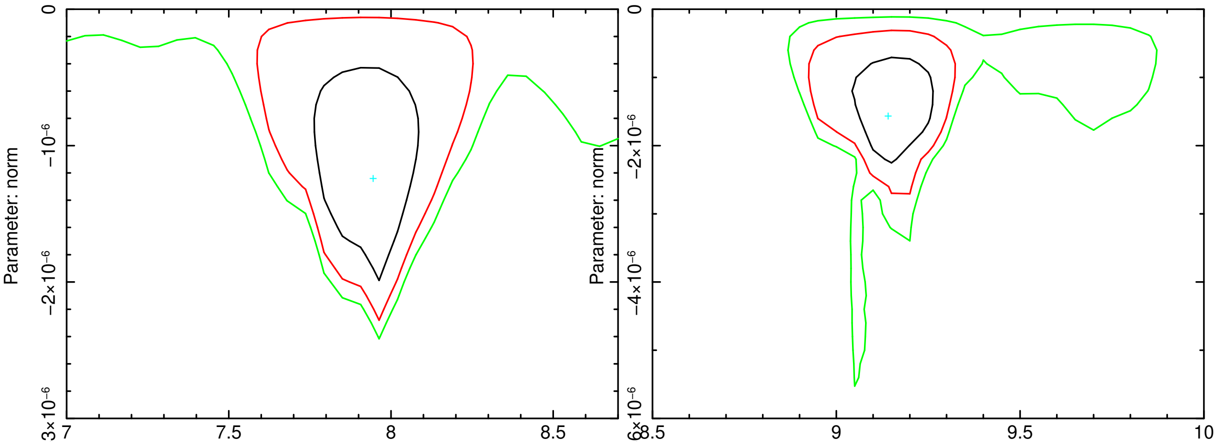

Figure 3.11: *Left:* 9.1 keV line parameters contour plots, whith levels: 68% (black), 90% (red), 95% (green). *Right:* same as *left*, for the 8 keV line.

Wind significance assessment

As shown in Protassov et al. (2002), The F-test should not be taken at face value when estimating line significance, as it can often overestimate such value. In order to have a robust estimate on whether the features are actually there or are just random fluctuations of the spectra, we make use of Monte Carlo Simulations, as many UFOs studies have done before (e.g. Tombesi et al. 2010, Matzeu et al. 2022).

The procedure is the following:

- We use the continuum model TBABS * ZXIPCF * POWERLAW + ZGAUSSIAN, with parameters set to the ones found in our analysis, to simulate 3 × 5000 spectra and backgrounds (pn, MOS1, and MOS2) with exposure times, response matrices and background levels as in the observed data, through the XSPEC task FAKEIT.

- After binning the simulated data with the same criteria as in the real data analysis, we fit the 5000 spectra triplets with the same model we used to produce them, and store the C-stat value and the number of d.o.f.

- We then refit the spectra with the addition of a gaussian line, stepping its energy between 5 and 10 keV (source rest-frame) and allowing it to be in either absorption or emission. We do so as our interest is in how often random fluctuations are mistaken for spectral lines *in general*, and not just limited to our specific energy and normalization. We store once again the C-stat value and d.o.f.

- We count how many times the gaussian produces an improvement in the fit, with respect to the continuum model, greater than the one we observed in the real data. This number, normalized to the total number of simulated spectra, gives the probability that our observed feature is actually just a count fluctuation. The significance of the line detection is therefore:

$$P = 1 - \frac{N_{[\Delta\mathcal{C}_{sim} > \Delta\mathcal{C}_{real}]}}{N_{tot}} \tag{3.5}$$

By performing such simulations we find that neither line is significant on its own. As it can be seen in Fig. 3.12, there is a large number of trials in which a gaussian can

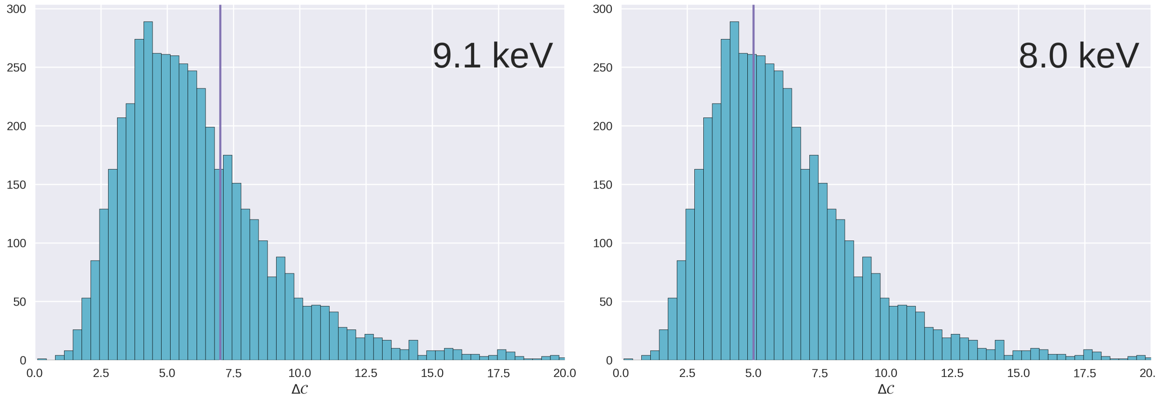

Figure 3.12: Differential distribution of $\Delta\mathcal{C}_{sim}$ obtained from the Monte Carlo simulations. In purple, the value of $\Delta\mathcal{C}$ measured for the 9.1 keV line (*left*) and the 8 keV line (*right*) for the original spectra.

produce a conspicuous fit improvement on data in which the line isn't actually there. We obtain significances of 66% and 38% respectively for the 9.1 and the 8.0 keV lines.

We conclude that we cannot significantly confirm the presence of UFOs in the 2005 spectra. The features are either ascribable to stochastic fluctuations, or, in case they are actually tracing UFOs, the SNR is not high enough to confirm the detection.

3.2.4 Winds in the 2020 spectra

We then proceeded with the same analysis of the more recent 2020 spectra. In this case, the continuum best-fit model was found with the aid of NuSTAR FPMA and FPMB data. In Fig. 3.13,*Left*, a different representation of the spectrum ("unfolded spectrum") is shown. The unfolded spectrum is model dependent and shows the spectrum corrected for the instrumental response.

Following the same reasoning as in Section 3.2.3, we found that the model that best fits the continuum (C-stat value of 349 with 313 d.o.f.), is the same as in 2005 (see residuals in Fig. 3.13,*Right*). The best-fit parameters are reported in Table 3.4.

Despite the model being the same, some parameters show significant changes from the 2005 to the 2020 observations: the absorber, which was previously consistent with not being ionized, has increased its ionization parameter ξ of more than one order of magnitude, and the column density also increased by a factor 10.

Model Component	parameter	value	Lower error (1σ)	Upper error (1σ)
ZXIPCF	N_H	$5.0 \times 10^{22}\ cm^2$	$-0.7 \times 10^{22}\ cm^2$	$0.6 \times 10^{22}\ cm^2$
	$log(\xi)$	1.1	-0.4	0.2
	Covering fraction	0.81	-0.07	0.05
POWERLAW	Photon index	2.11	-0.18	0.15
	Normalization^a	1.7×10^{-4}	-5×10^{-05}	5×10^{-05}

Table 3.4: Values for best-fit continuum model. Notes: a: units for normalization are photons/keV/cm^2/s

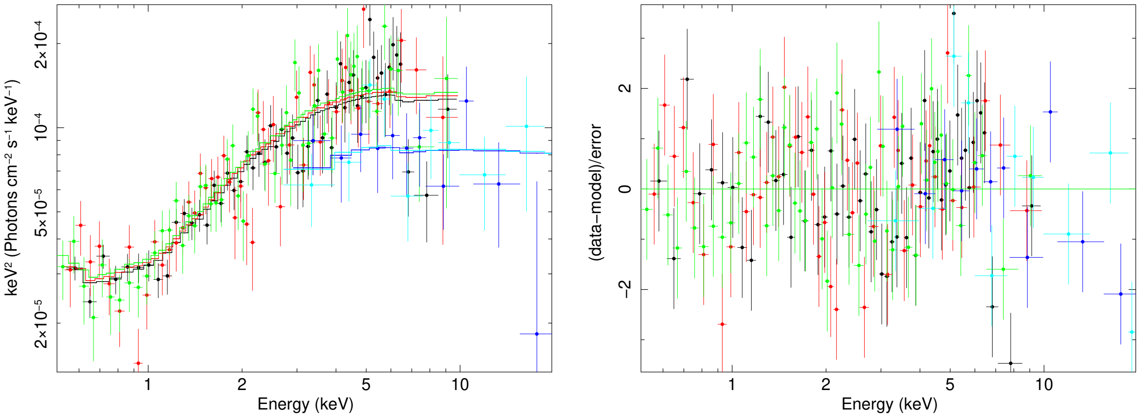

Figure 3.13: *Left:* unfolded pn (black), MOS1 (red), MOS2 (green), FPMA (cyan), and FPMB (blue) spectra, with solid lines representing the best-fit model. *Right:* Residuals of the best-fit model.

The de-absorbed, intrinsic luminosity measured in the 2-10 keV band also decreased of a factor ~ 4: $log(L_{2020}/[\text{erg/s}]) = 43.37 \pm 0.01$ vs $log(L_{2005}/[\text{erg/s}]) = 43.91 \pm 0.01$. Covering fraction and photon index stayed consistent between the two observations.

In Fig. 3.14 we show the contour plots involving the ionization parameter, which is now never consistent with 0, as opposed to the results obtained for the 2005 data.

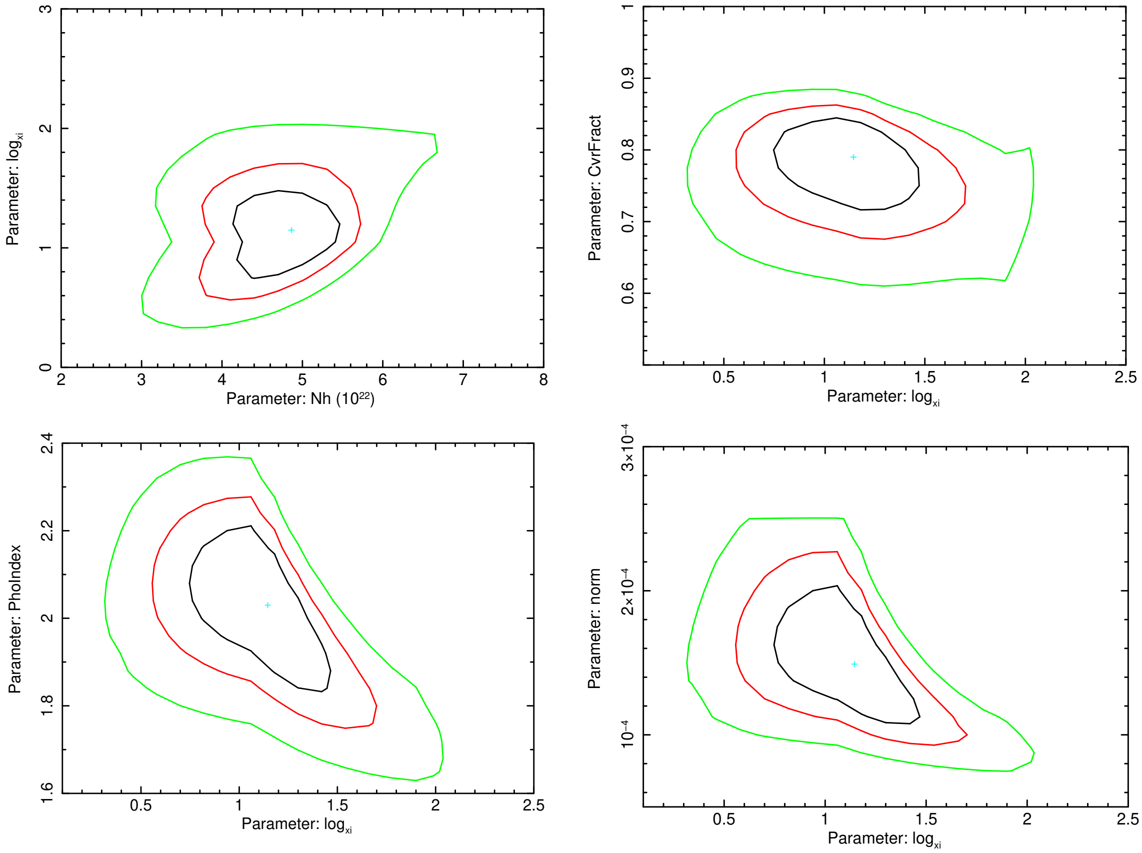

Figure 3.14: 68% (black), 90% (red) and 99% (green) contour plots for the 2020 continuum model ionization parameter $log(\xi)$

Blind search and line fitting

We conducted again the blind search method, as described in Sect. 3.2.3 and obtained the results shown in Figure 3.15. We tried both XMM-Newton + NuSTAR (wNu) and XMM-Newton alone (noNu), in order to compare 2005 spectra to data of the same type in the second case (the continuum model parameters do not differ with the addition or removal of the FPM modules).

We notice an emission feature around 7.1 keV and a double-peaked depression around 8 keV. In the noNu contours, it seems that such depression is actually the blending of two features, one at around 7.9 keV and one at 8.5 keV.

Following the same logic as before, we first fit the 7.1 keV emission line. In the wNu dataset, the new fit has a C-stat value of 340 with 311 d.o.f. (F-test: 98%). In the noNu one, the initial C-stat value of 248 over 229 d.o.f. goes to 239 over 227 d.o.f.

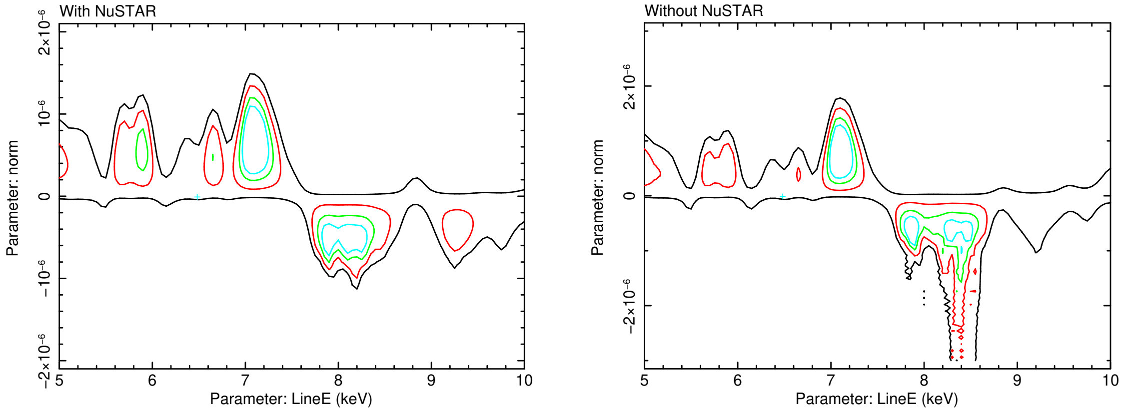

Figure 3.15: Blind search contours with 3 EPIC and 2 FPM spectra (*left*) and with EPIC spectra alone (*right*). Note the scale difference, and see Fig. 3.9 for comparison
.

(F-test: 98%). In both cases, the line has energy E=7.1 ± 0.1 keV, consistent with the typical AGN FeXXVI line at 6.97 keV. In this sense, we see no difference between the two datasets.

We note that an increase in the ionization state of the emission Fe-line is reflected in the increase in the ionization parameter.

Concerning the absorption lines, we find in the no noNu case a line at E=$8.5^{+0.1}_{-0.2}$ keV, with a $\Delta\mathcal{C} = 6$ (F-test: 94%). Moving the initial value of such line towards the 7.9 keV feature, the fit converges to E=$7.9^{+0.8}_{-0.1}$ with equal $\Delta\mathcal{C}$ value. The big upper error suggests that the fit is incapable of distinguishing between the two features, as they have the same C-stat value. This is also evident from the contour plots in Fig. 3.16,*right*. If we add a second line, in order to account for both absorption components, we get once again $\Delta\mathcal{C} = 6$ (F-test = 97%)[3], and the upper error of the 7.9 keV line shrinks down to 0.1 keV. We, therefore, believe this broad depression in the spectrum is actually two blended narrow features.

In the wNu case, the addition of an absorption line also provides a $\Delta\mathcal{C} = 6$. The line energy converges to $E = 7.9^{+0.5}_{-0.5}$ keV. In this case, the instrumental resolution (which gets lowered with the addition of NuSTAR) does not allow to distinguish between the

---

[3] The F-test significance depends not only on the Δ-statistic, but also on the ratios between the d.o.f. before and after including a new model component. On the same dataset, the more components are added to a model, the higher the ratio will be. Therefore, equal values of $\Delta\mathcal{C}$ will give higher significance for models with more free parameters.

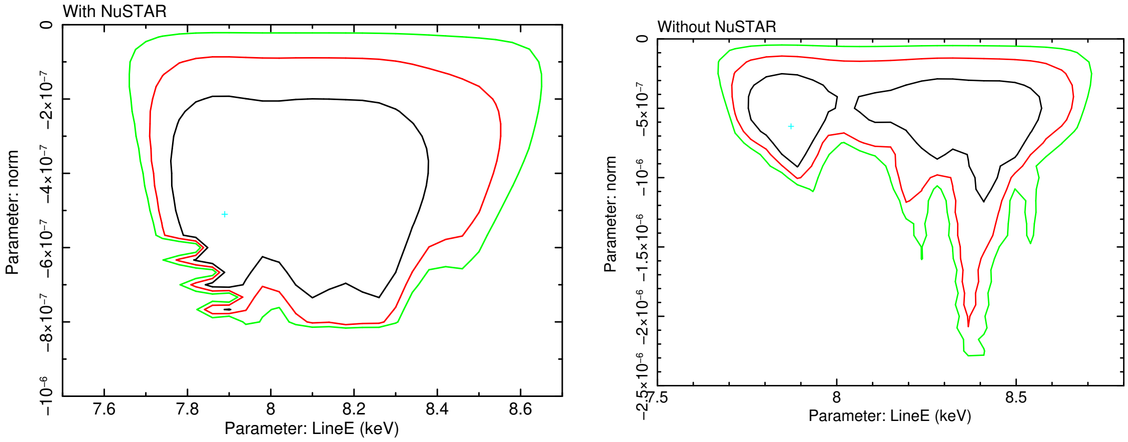

Figure 3.16: *Left*: wNu 7.9 keV line parameters contour plots, with levels: 68% (black), 90% (red), 95% (green). Right: same as left, for the noNu case.

two features (hence the big upper error, Fig. 3.16,*left*). Moreover, the addition of a second gaussian does not provide a significant improvement ($\Delta\mathcal{C} = 4$).

We note that a possible explanation for the blending of the absorption features in the wNu case could be the binning criteria, which creates larger bins for the FPMA and FPMB modules than for the EPIC data, in which photon counts are higher. In order to explore this possibility, we also tested combining EPIC data binned with the KB-scheme with NuSTAR data binned with the GRPPHA group-min-1 option. This is still statistically consistent, as we are using Cash-statistics, which is designed for Poissonian binning regime.

By doing so, we are able to distinguish the two features as in the noNu case (Fig. 3.17), with results completely consistent with the noNu case (same $\Delta\mathcal{C}$s, same continuum, and same energies and errors).

We decide to only focus on the noNu case in the following analysis, in order to have similar datasets when comparing the 2020 spectrum with the 2005 one, but we stress that the commonly used approach of using the same binning scheme for all data might not be ideal in cases similar to this, in which you are looking for high energy absorption features with low photon statistics.

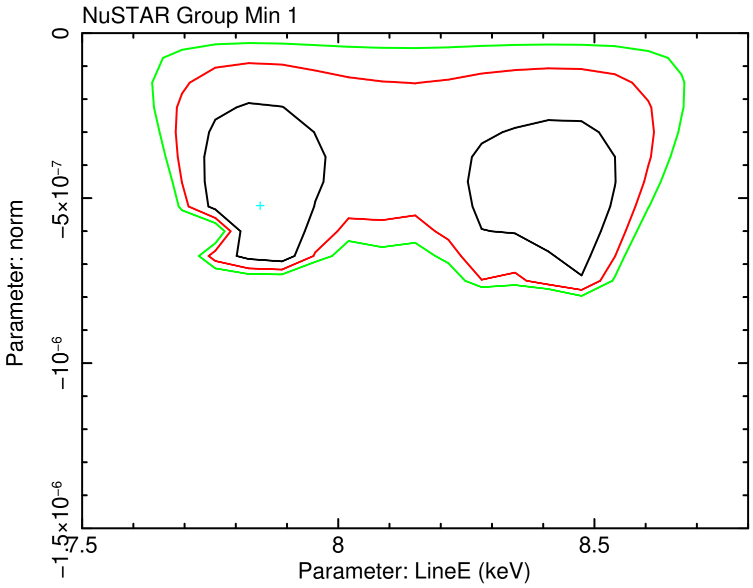

Figure 3.17: wNu absorption line parameters contour plots, at 68% (black), 90% (red) and 95%(green) signficance level. In this case, NuSTAR was binned through the group-min-1 option. The implementation of this binning scheme shows evidence for two narrow absorption features, rather than one.

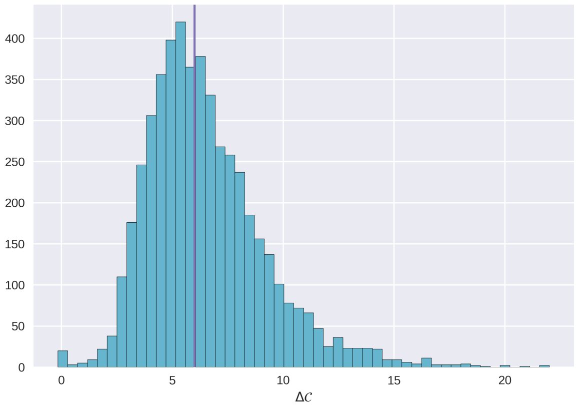

Figure 3.18: Differential distribution of $\Delta\mathcal{C}_{sim}$ obtained from the Monte Carlo simulations. In purple, $\Delta\mathcal{C}_{real}$ for either the 7.9 keV and the 8.5 keV lines

Wind significance assessment

We perform Monte Carlo simulations as described in Section 3.2.3, using as the base continuum model TBABS*ZXIPCF*POWERLAW + ZGA (we have included the 7.1 keV emission line, as it was done for the 2005 dataset with the 6.5 keV line). We once again look for the significance of detecting one narrow (σ=10eV) line above 5 keV.

For both the 7.9 keV and 8.5 keV absorption lines, we obtain a significance of 50%,

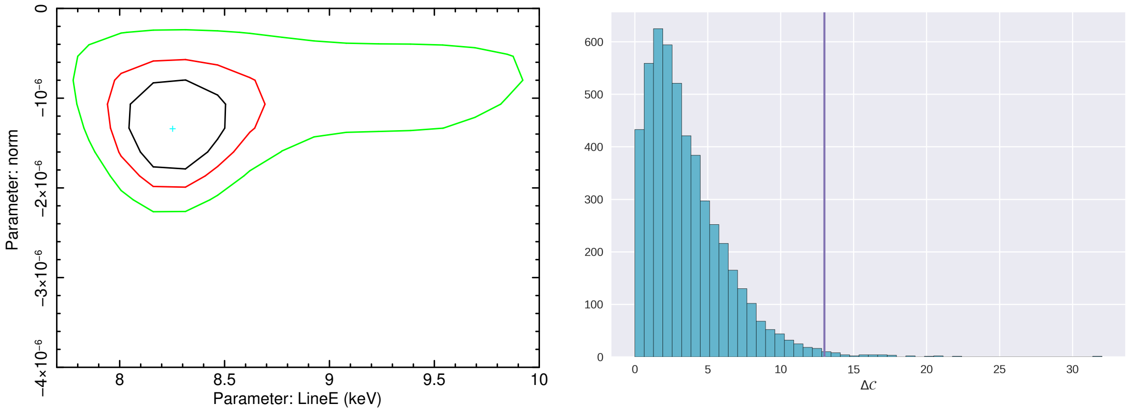

Figure 3.19: *Left*: 68%,90%, and 99% contour plots for the broad line energy and normalization, derived in the nuNU case but also applicable to wNu-GM1. *Right*: Monte Carlo results as in Fig. 3.18 in the noNu case where the absorption line was treated as broad.

therefore neither narrow line is considered to be significant (Fig. 3.18).

However, the 2020 data might not be necessarily interpreted as the blending of 2 gaussian absorption lines, and the spectra could be better reproduced by including one broad absorption line. We tested this in the noNu case and also in the wNu spectra, where NuSTAR data was binned with the group min 1 scheme (wNu-GM1), motivated by the previous section.

In the XMM-Newton-only case, we achieve a fit improvement of $\Delta\mathcal{C} = 13/3$ d.o.f. (99.6% significance from F-test), finding a line at E=$8.2^{+0.6}_{-0.3}$ keV with $\sigma = 0.47^{+0.8}_{-0.2}$ keV (Fig. 3.19). Including NuSTAR, we obtain similar results (also with $\Delta\mathcal{C} = 13/3$ d.o.f.) and similar values of F-test significance (99.4%).

We perform Monte-Carlo line significance assessment as before, but this time allowing the σ to vary as well between 0.2 and 0.8 keV (for smaller values we would be fitting narrow lines, while for greater values could be fitting the continuum.). The simulations provide a significance of 99.1 %, which corresponds to 2.1 σ (Fig. 3.19,*Right*).

3.2.5 Physical Winds Modelling

Motivated by the previously described significant detection, we fit ad hoc XSTAR tables (Kallman 1999) instead of simple phenomenological gaussians. Such tables can be implemented as a model component in order to compute the physical conditions

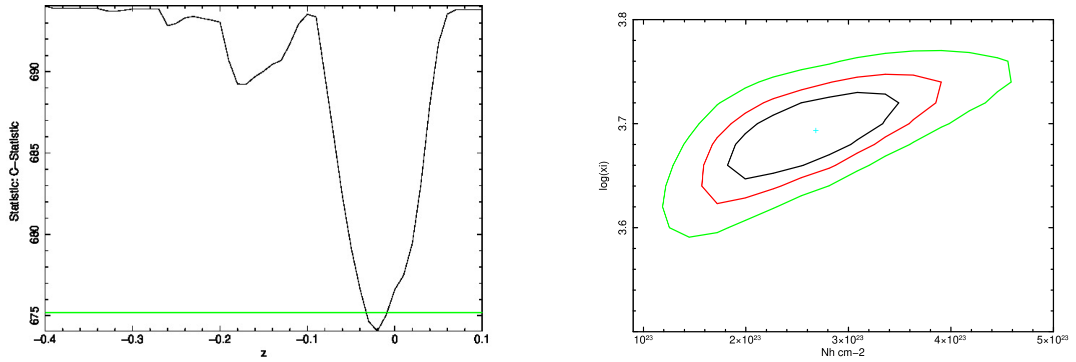

Figure 3.20: *Left:* C-statistic as a function of XSTAR parameter z. The unambiguous minimum at z$\sim$ 0.02 is indicating at what velocity the UFO is moving. *Right:* Contour plots of the XSTAR parameters N$_H$ and $log(\xi)$.

of photoionized gas, which are described by the column density N$_H$, the ionization parameter ξ and the redshift z[4]. We tested two tables, one with parameter v_{turb} = 1000 km/s and one with v_{turb} = 5000 km/s on the wNu-GM1 data.

The spectra are best reproduced when the 5000 km/s table is used and when the 7.1 keV emission line is omitted from the model. At the same time, the photon index adjusts to the slightly shallower value of 1.94, while remaining consistent with the previously found value of 2.11 within 1σ. Following the procedure implemented in Tombesi et al. (2011), we stepped the z parameter between -0.4 and 0.1 in order to find the best-fit improvement value (the results are plotted in Fig. 3.20). With a fit improvement of $\Delta\mathcal{C}$ = 18/3 d.o.f (99.98 %, almost 4σ), going from 519 vs 555 d.o.f to 501 vs 552 d.o.f., we obtain $z = -0.017 \pm 0.013$, $log\xi = 3.69 \pm 0.08$ and N$_H = (2.3 \pm 1.3) \times 10^{23}$cm^{-2}. These values are well representative of the average UFO population, as it will be discussed in Chapter 5.

We note that the fit improves much more significantly when the UFO is modeled as photoionized gas (XSTAR), rather than as a gaussian absorption line. This is due to the fact that the photoionized gas model takes into account a variety of absorption lines on a broad spectral range ($\sim 1 - 10keV$). As the outflow does not only contain Iron, this model better reproduces the data, compared to a gaussian absorption line, which only models the most prominent Iron absorption (See e.g Pounds and Page 2006).

---

[4] the z computed by the model is related to the absorber's redshift (z_a) relative to the source's position (z_c) by $(1+z) = (1+z_a)(1+z_c)$

3.2.6 Outflow Energetics

The mass outflow rate can be derived using the following equation:

$$\dot{M} = \Omega N_H m_p V_{out} R \tag{3.6}$$

where Ω is the solid angle subtended by the outflow, m_p is the proton mass, V_{out} is the ouflow velocity, R its radius, and N_H the column density of the outflowing gas.

By adopting the same recipe as Nardini and Zubovas (2018) ($\Omega/4\pi = 0.5$ and $R = 2c^2/V_{out}^2$) we can derive the following outflow properties through:

$$\dot{M} = 9.4\left(\frac{N_H}{10^2 4cm^{-2}}\right)\beta^{-1} M_8 \times 10^{24} g/s \tag{3.7}$$

where $\beta \times c = V_{out}$, and M_8 is the black hole mass in units of $10^8 M_\odot$.

V_{out} can be computed from z through the relativistic formula:

$$1 + z = \sqrt{\frac{1+\beta}{1-\beta}} \tag{3.8}$$

By solving for β we measure the velocity of the UFO to be

- $V_{out} = (0.15 \pm 0.1)$ c

Using Eq. 3.7, we obtain a mass outflow rate $\dot{M}_{out}$ of:

- $\dot{M}_{out} = (2.8 \pm 0.5) \times 10^{-2}\ M_\odot/yr$

and similarly to what we have done in Section 3.1.2, we obtain the following momentum outflow rate $\dot{P}_{out}$ and kinetic power $\dot{K}_{out}$:

- $\dot{P}_{out} = (8 \pm 5)\ \times 10^{33} erg/cm$
- $\dot{K}_{out} = (1.8 \pm 1.2)\ \times 10^{43} erg/s$

In Chapter 5 we compare the parameters obtained for the UFO and for the ionized outflow to each other, to the properties of the AGN, and to other samples from literature, and we discuss the physical implications.

Chapter 4

The X-ray Variability

In this Chapter, we derive the 20-year-long X-ray lightcurve for 2M0918 in the 0.5-2 keV band. This range was chosen both for its universal usage in literature to account for the soft X-ray emission, and also because it guarantees good performance for all of the instruments considered in this analysis (see Fig. 2.7 for a comparison in the effective areas of the facilities used).

The observations analyzed are listed in Table 4.1

Instrument	**Date**	**Reference**
Chandra	2001-02-18	Wilkes et al. 2002
XMM-Newton	2003-04-24	Wilkes et al. 2005
XMM-Newton	2005-11-15	PW07
eROSITA (eRASS1)	2020-05-02	This Work
XMM-Newton + NuSTAR	2020-10-19	”
eROSITA (eRASS2)	2020-11-03	”
eROSITA (eRASS3)	2021-05-06	”
eROSITA (eRASS4)	2021-11-05	”

Table 4.1: All the observations used in the variability analysis listed in ascending chronological order, together with the instrument used and the main reference where the data is presented first.

4.1 Populating the Lightcurve

For all of our observations, we inferred fluxes from spectral analysis. The analysis for the 2005 and 2020 XMM-Newton observations has already been presented in the previous Chapter, while the rest is reported in the following sections, starting from the earliest observation to the latest. All the errors in this section are at 90% confidence, unless stated otherwise.

4.1.1 Chandra

For the 2001 Chandra data, we used products as extracted by the CXC's Automated Processing pipeline (ObsID 2159[1]). The data were processed with CXC software version 10.9.2, using CalDB version 4.9.4. We then extracted the source and background spectra, and produced the ARF and RMF with the SPECEXTRACT task of the Chandra Interactive Analysis of Observations (CIAO) software version 4.14.0, using a circular region of r=5" for the source and r=27" for the background. The event file with the extraction regions corresponding to source and background can be found in Fig. 4.1, *Left*.

The spectrum has a total of 155 counts in the 0.5-7 keV range, with an exposure time of ∼ 2 ks.

Prompted by the spectral fitting results obtained in Chapter 3, we model the 2001 spectrum in XSPEC with an absorbed powerlaw model (TBABS*ZTBABS*POWERLAW) in the 0.5-7 keV range, with binning scheme GROUP-MIN-1. The model reproduces the spectrum nicely (see Fig. 4.1, *right*) with a C-stat value of 95/383 d.o.f. The

---

[1] https://doi.org/10.25574/02159

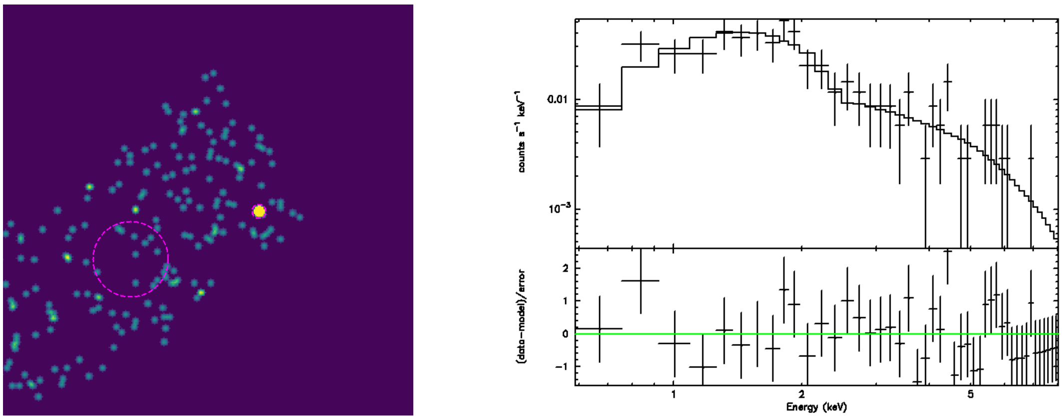

Figure 4.1: *Left:* 2001 Chandra image of 2M0918. The counts were re-binned and smoothed for visualization purposes, and the dashed magenta circles represent the regions used for background extraction (larger circle) and source spectral extraction (smaller circle). *Right:* 0.5-7 keV 2001 Chandra spectrum of 2M0918, rebinned for plotting purposes only. The solid line represents the model. Below the spectrum, the residuals show that the data is well reproduced by the neutrally absorbed powerlaw model.

galactic N_H (TBABS) is set at 4×10^{20} cm^2, as it was done for the 2005 and 2020 XMM-Newton observations, and the redshift of the local absorber (ZTBABS) is once again set to be z=0.149. We obtain a photon index for the powerlaw of $\Gamma = 1.87 \pm 0.4$ with a normalization of $(1.84^{+0.9}_{-0.6}) \times 10^{-4}$ photons/keV/cm^2/s, while the restframe absorber can only be constrained as an upper limit of $N_H = 3.7 \times 10^{21}$ cm^2 at 90% confidence level. This is also evident from the contour plots in Fig. 4.2, where the large uncertainties in parameter estimation are clear.

We note that the photon index is consistent with the one derived for the 2005 and 2020 observations, while the powerlaw normalization seems to be consistent only with the 2020 spectra.

We derived fluxes in the 0.5-2 keV band corrected for galactic absorption with the CFLUX model component, obtaining $logF = -12.54 \pm 0.6$ erg/s/cm^2.

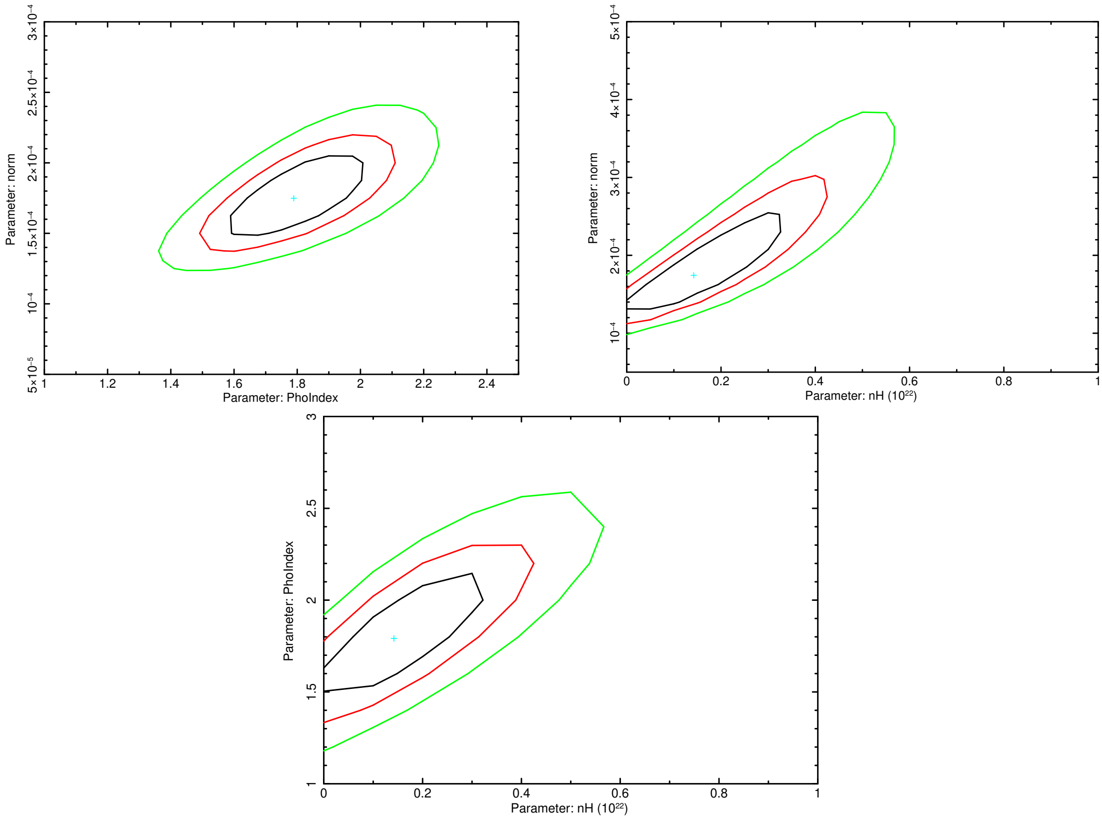

Figure 4.2: 68% (black), 90% (red) and 99% (green) confidence levels contour plots for the free parameters of the model fit to the 2001 Chandra spectrum. The N_H is always consistent with 0.

4.1.2 XMM-Newton - 2003

For the 2003 XMM-Newton observations, we extract the spectra following the same procedure as in Section 3.2.3. The maximum SNR in the 2-10 keV band is achieved with source extraction region radii of 32", 38" and 33" respectively for MOS1, MOS2, and pn. We extracted the background spectra from regions of 100" in radius for the MOS cameras and 50" for the pn.

The exposure times for the 2003 XMM-Newton observations are ~8000s, with 467, 208, and 153 counts for pn, MOS1, and MOS2 respectively. In order to be consistent with the other XMM-Newton observations, we once again apply the optimal binning scheme to the data, as it was done for the 2005 and 2020 observations.

We initially model the three spectra simultaneously in the 0.5-10 keV range with the same simple absorbed powerlaw model as it was done in the previous Chandra observation. However the fit is of poor quality (C-stat value: 287/198 d.o.f.) and while the absorber is rejected by the fit, the inferred photon index is $\Gamma = 1.17 \pm 0.12$, which is well below the average AGN photon index of ~ 1.8 (Nandra and Pounds 1994, Dadina 2008, Ricci et al. 2017). A photon index of less than 1.4 at 90% confidence has been used in literature as a selection criterion for highly obscured AGN (Lanzuisi et al. 2013, Georgantopoulos et al. 2013, Lanzuisi et al. 2018), as an absorbed powerlaw with an intrinsically steeper photon index can be mimicked by an unabsorbed powerlaw with a flatter photon index (George and Fabian 1991). We, therefore, insisted on including absorbers in the model we fit.

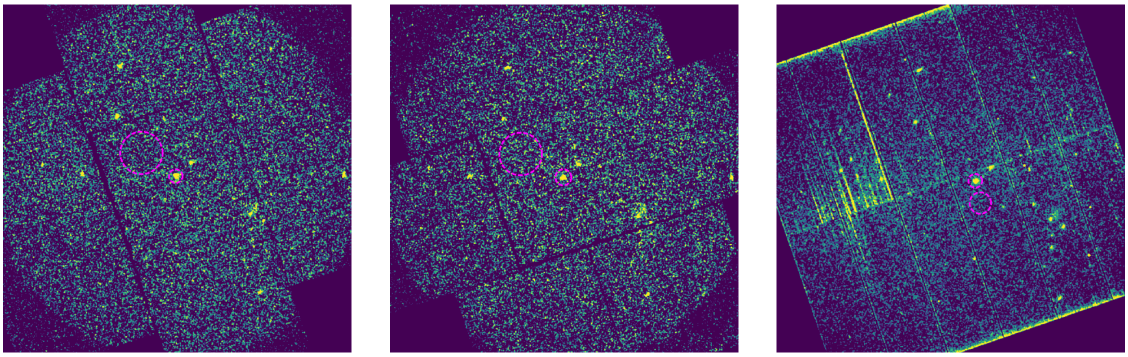

Figure 4.3: MOS1, MOS2, and pn smoothed images of the 2003 observation. In magenta, the background extraction regions and the source extraction regions.

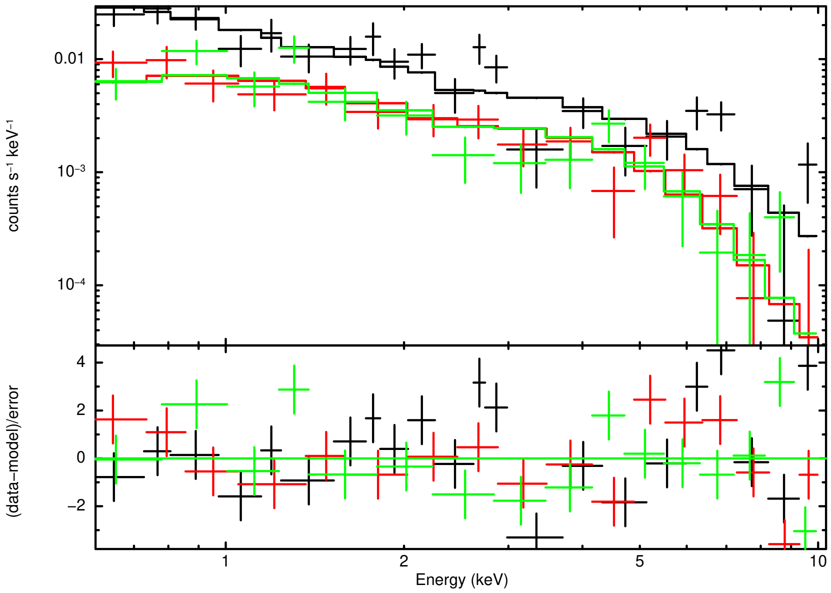

Figure 4.4: 2003 pn (black), MOS1 (green) and MOS2 (red) spectra rebinned for plotting purposes, The solid lines represent the best-fit model (TBABS*TBPCF*PO).

We initially tested ZXIPCF for consistency with the other XMM-Newton observations analyzed, but the low photon statistics didn't allow to break the degeneracies of the model parameters even when the photon index was frozen to the value obtained from the 2005 and 2020 spectra (~ 2). We, therefore, resorted to TBPCF, which is the same as ZTBABS with the addition of a parameter to account for partial covering. We freeze this parameter to a covering fraction of 80%, as motivated by the results for the other XMM-Newton observations. The spectrum can be seen in Fig. 4.4.

With this model, we obtain a better fit both from a statistical (C-stat value: 287/198 d.o.f.) and physical point of view: The photon index is now $\Gamma = 2.03 \pm 0.14$, in agreement with the other measurements reported in this work. The partially covering absorber has a column density of $N_H = 6.4^{+4.2}_{-2.0} \times 10^{22}$ cm^{-2}, which is consistent with $N_H > 10^{23}$, as it is also evident from the contour plots in Fig. 4.5.

From this spectral fit, through CFLUX, we obtain an observed $logF = -13.32 \pm 0.03$ erg/s/cm^2, which is a factor $\gtrsim 6$ dimmer than the Chandra observation.

We note that in the hard band some spectral features, such as iron lines, can still be present in the residuals in Fig. 4.4, but as the focus of our spectral analysis is soft flux estimation we are satisfied with our best-fit model.

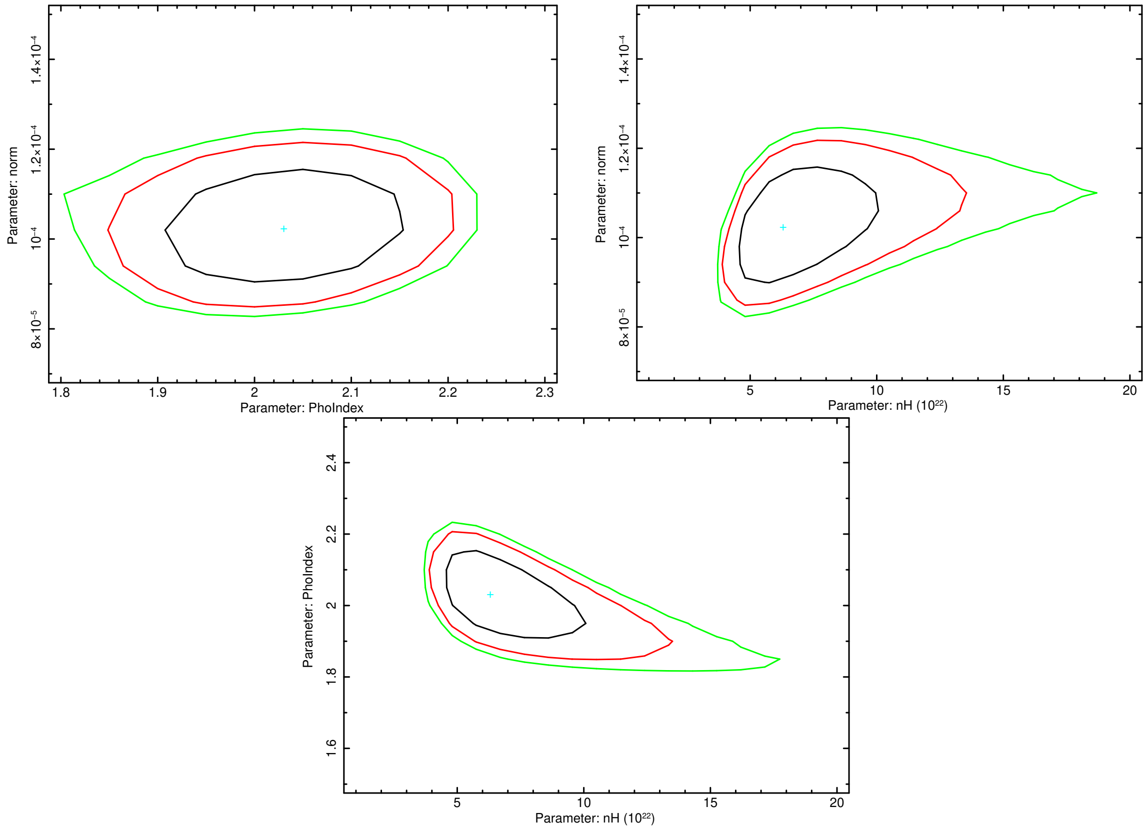

Figure 4.5: 68% (black), 90% (red) and 95% (green) confidence levels contour plots for the free parameters of the model fit to the 2003 XMM spectrum. The N_H spans a large region in parameter space, but is now no longer consistent with 0.

4.1.3 eROSITA

To analyze the eROSITA spectra we first matched 2M0918 with the eROSITA catalogs for eRASS1 through eRASS4 (available within the eROSITA-DE consortium) with the software TOPCAT v4.8-6. For all 4 catalogs, the matching was positive and unambiguous. The eROSITA images of the source are shown in Fig. 4.6.

We subsequently downloaded the source products from the web tool DATool as extracted by the eROSITA Science Analysis Software System (eSASS, Brunner et al. 2022) pipeline in the latest available configuration. The products included ARFs, RMFs, and source and background spectra for each eRASS and for different TM combinations (see Liu et al. 2022 for details on how the source and background extraction regions are defined in the automated pipeline).

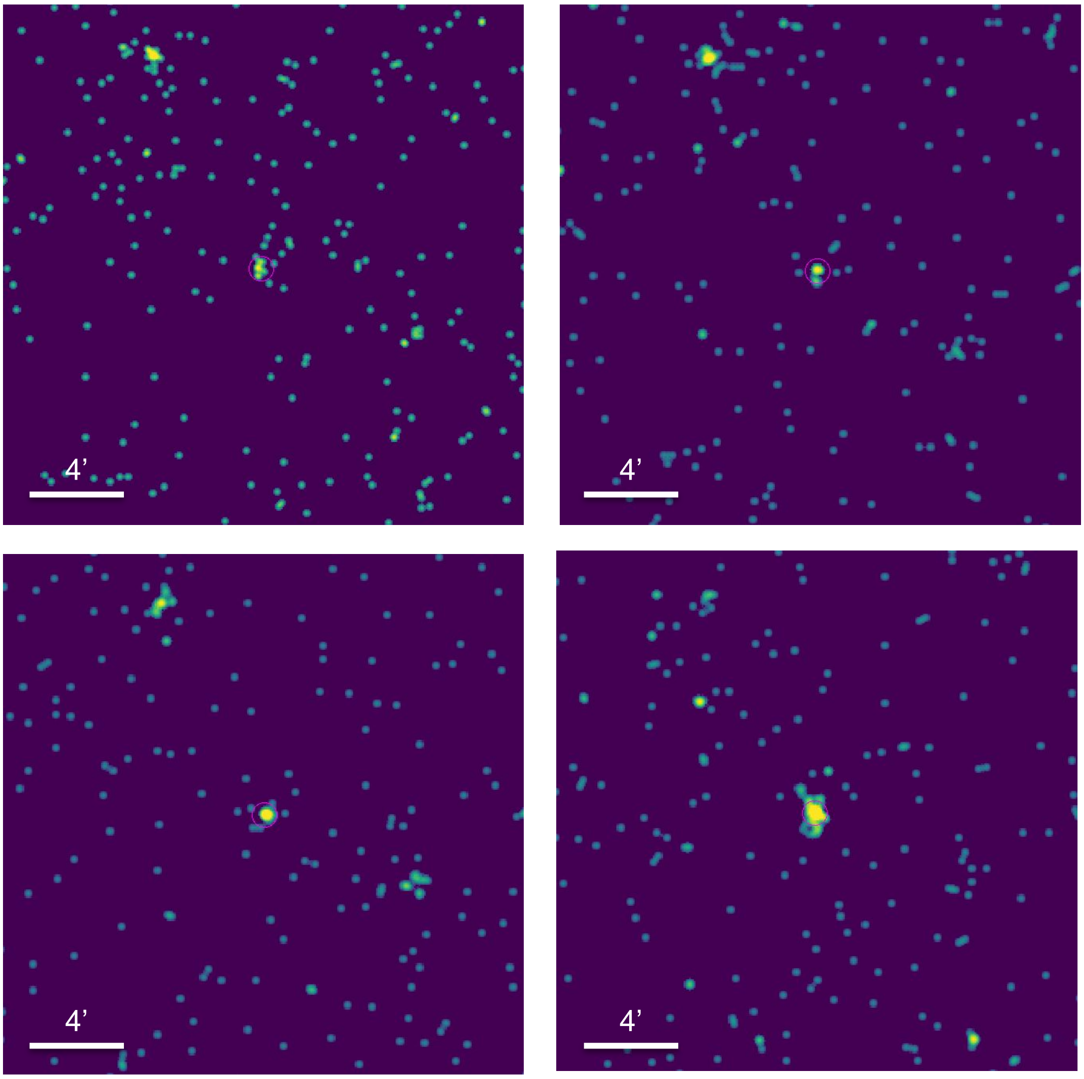

Figure 4.6: eRASS1 (*top left*), eRASS2 (*top right*), eRASS3 (*bottom left*) and eRASS4 (*bottom right*) smoothed images of 2M0918 in the 0.2-2.3 keV band. The AGN is located in the d=60” circle in magenta. Even from a visual inspection, it is clear that the source brightened in eRASS4.

The observation strategy of eROSITA is such that exposure times and photon counts will be much lower than for other telescopes (Tab. 4.2). Because of this limitation on photon statistics, we resorted to a different method for the spectral analysis, making use of Bayesian statistics and background modeling.

We chose to model the spectra of the combined TM1, TM2, TM3, TM4, and TM6, leaving out TM5 and TM7 because these modules are known to be affected by light leaks, which contaminate observations (see P21). The analysis was conducted with

eRASS	**Counts**	**Exp. Time** [s]
eRASS1	17	170
eRASS2	5	140
eRASS3	17	135
eRASS4	39	149

Table 4.2: Photon counts and exposure times for each eRASS observation of 2M0918 in the full energy band. eRASS 4 has ∼ 8× more counts than eRASS2, with comparable exposure times.

the software Bayesian X-ray Analysis (BXA[2], Buchner et al. 2014) which connects the nested sampling algorithm UltraNest[3] package (Buchner 2021 and references therein), with the fitting environment CIAO/Sherpa (Fruscione et al. 2006).

We chose to use this analysis technique as it is particularly well suited for low photon statistics, as no binning or assumption of gaussianity of the parameter distribution is needed. Moreover, BXA also includes the possibility to simultaneously model the background with empirical Principal Component Analysis (PCA) models (See Simmonds et al. 2018 for details on background PCA models).

We model the 4 unbinned spectra and background simultaneously in the 0.2 - 10 keV range. SHERPA include xspec models, therefore for consistency with the almost simultaneous XMM-Newton observations we model the source as a powerlaw absorbed by TBPCF with covering fraction fixed at 80%, with the usual galactic absorption. BXA, being of bayesian nature, allows to include priors on the parameters, which we set to be uniform on the log of the powerlaw normalization and the column density of the local absorber. This means that we're assuming total ignorance on these parameters before our analysis. We instead implement a gaussian prior for the photon index with $\mu = 1.95$ and $\sigma = 0.15$, based on the discussion in section 4.1.2. Given our low photon counts (Tab 4.2) and the softness of the eROSITA response it is crucial to have some constraints on the photon index.

The 4 spectra are plotted in Fig. 4.7, together with the best-fit model and the background model for each observation.

---

[2] `https://johannesbuchner.github.io/BXA/`

[3] `https://johannesbuchner.github.io/UltraNest/`

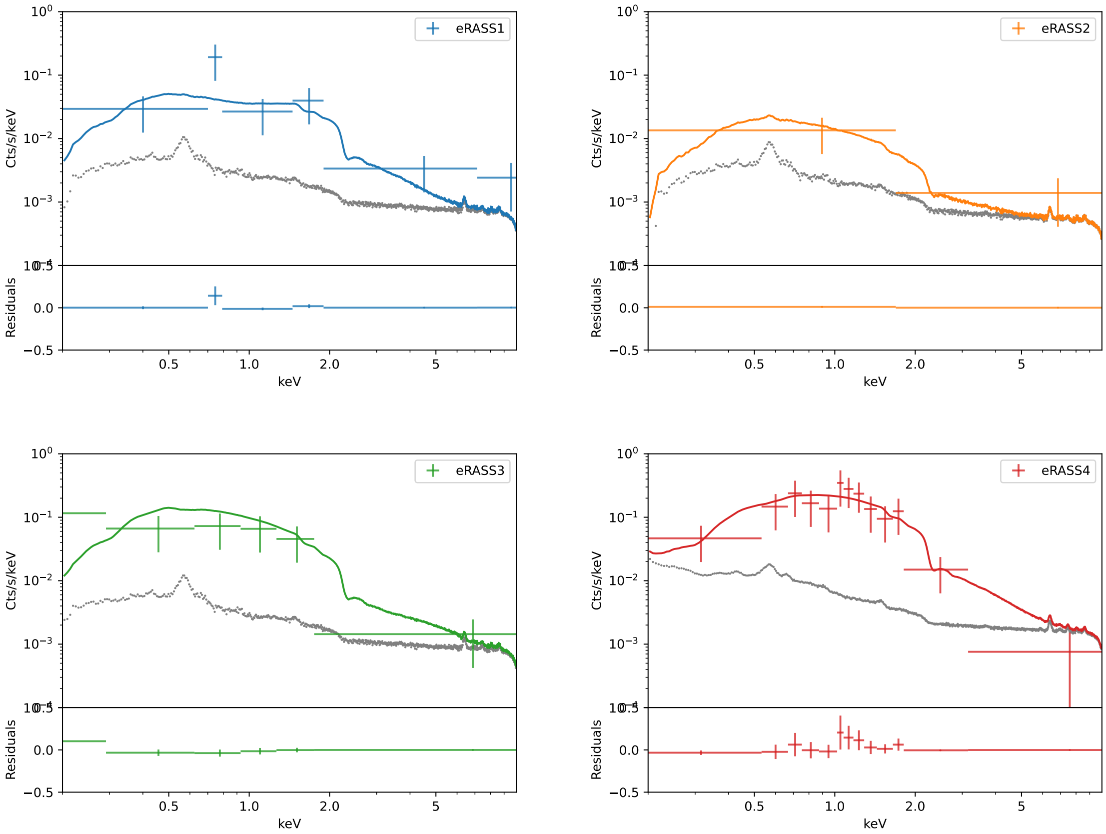

Figure 4.7: eRASS1-4 spectra of 2M0918 rebinned for plotting purposes only. The solid line represents the best-fit model, while the grey dotted line is the background best-fit model. Below the spectra, the residuals are plotted. It's easy to note that eRASS2 is the dimmest of all observations while eRASS4 is the brightest, as we also knew from Tab 4.2.

After running the analysis we produced a cornerplot of the posterior distribution of the fitted parameters with the Python module Corner.py (Foreman-Mackey 2016, which are shown in Fig. 4.8. This is similar to the contour plots that we produced with XSPEC, but the contours here are credibility rather than confidence regions. As one can clearly see from Fig 4.8 and Tab. 4.3, the fit is insensitive to the local absorber in all eRASSes except 4 (the brightest), in which we find moderate absorption. We also note that the source is consistent with being undetected in eRASS2.

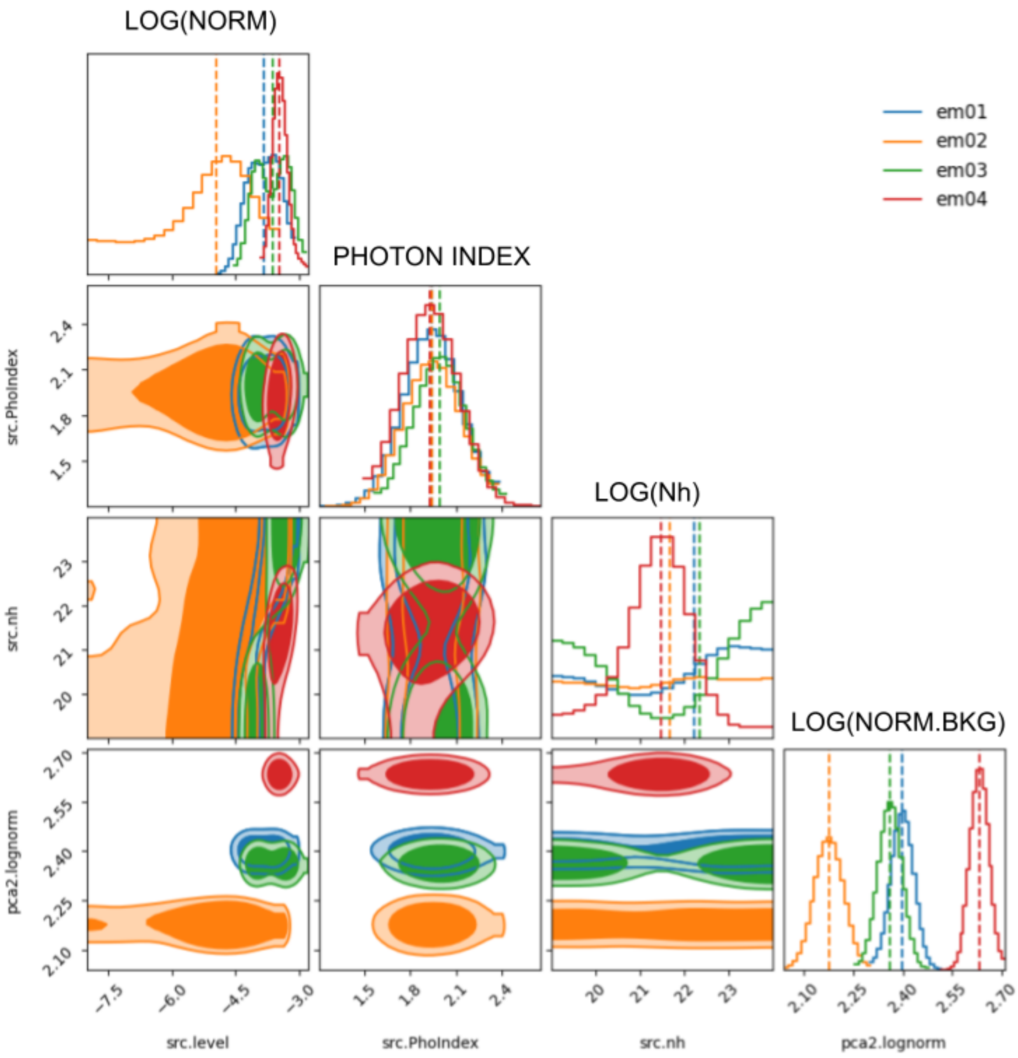

Figure 4.8: Cornerplot of the fitted parameters (powerlaw normalization, photon index, column density and background normalization). The colors are the same as in Fig. 4.7. The histograms represent individual parameter posterior distribution, while the shaded contours the credibility regions of the interception of different parameters (the darker color corresponds to 68% of the integrated posterior, while the lighter color to 90%)

eRASS	**log(norm)**	$\mathbf{\Gamma}$	$\log(\mathbf{N}_H/[\mathrm{cm}^{-2}])$	$\mathbf{\log(F/[erg/s/cm^2])}$
eRASS1	-3.84 ± 0.32	1.94 ± 0.14	21.79 ± 1.52	$1.43^{+0.34}_{-0.41} \times 10^{-13}$
eRASS2	-5.31 ± 1.10	1.95 ± 0.15	21.60 ± 1.46	$1.36^{+1.98}_{-1.32} \times 10^{-14}$
eRASS3	-3.65 ± 0.35	1.99 ± 0.15	21.70 ± 1.77	$2.21^{+0.47}_{-0.57} \times 10^{-13}$
eRASS4	-3.44 ± 0.16	1.92 ± 0.15	21.37 ± 0.74	$5.42^{+0.63}_{-0.89} \times 10^{-13}$

Table 4.3: Best-fit parameters for each eROSITA scan of 2M0918. The errors in this table correspond to 1σ. The only observation in which the fit is able to converge to a definitive column density is eRASS4.

4.2 The 20-year lightcurve

We show the 20-year-long observed flux X-ray lightcurve in Fig 4.9, which includes fluxes from the spectra presented in this Chapter and the ones in Chapter 3.

Variability is evident and recurrent, with the 2005 XMM-Newton observation being 11x brighter than the 2003 observation and 6x brighter than the 2020 observation. The dimmest state is the one associated with eRASS2, where the source was consistent with being undetected. However, this was only 14 days after a clear XMM-Newton detection, and if we take the upper error bar to be the 3σ upper limit on the eRASS2 flux, the 2 values are actually compatible with small variability. The flux did however increase again by a factor 5.3 with respect to the 2020 XMM-Newton observation in eRASS4.

In Fig. 4.10 we plot N_H as a function of time (with the exclusion of eRASS 1-3, in which the fit was insensitive to this parameter). When we compare it to Fig. 4.9 a clear anticorrelation between N_H and Flux is noticeable. In other words, dimmer states correspond to higher inferred column density, while brighter states correspond to lower quantities of obscuring material. This would favor a scenario in which the recurring alternating between high and low flux states is driven by a change in the

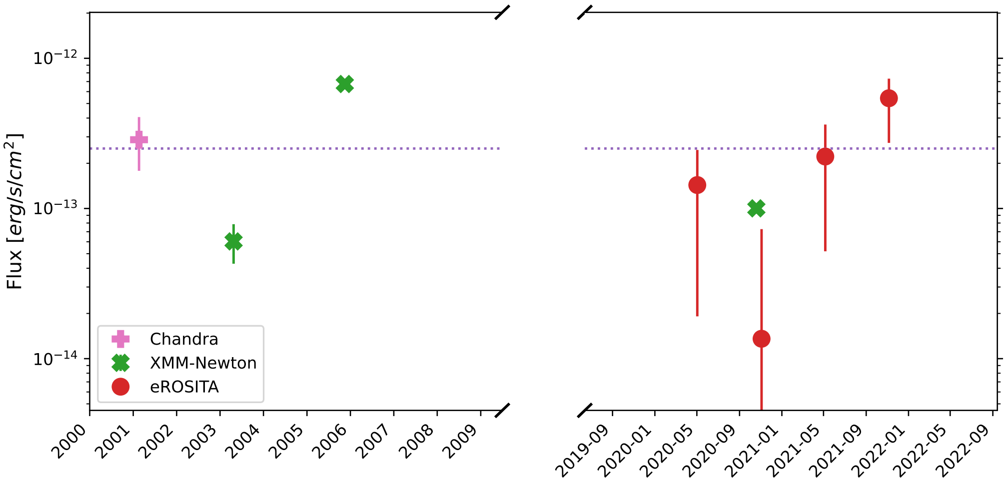

Figure 4.9: 0.5-2 keV cross-instrument lightcurve for 2M0918. The error bars correspond to 3σ for all observations. The purple dotted line represents the weighted average flux level.

absorbing material, which is not uncommon (See e.g. Torricelli-Ciamponi et al. 2014 and references therein for other examples of variable N_H in AGN).

We also plot the intrinsic flux variation over time in Fig. 4.11. As one can see, the intrinsic flux increases significantly between 2003 and 2005 and then drops again in 2020. The flux ratios are 11.6 (2005/2003) and 7 (2005/2020).

We also note that the eRASS2 upper limit does not seem to be consistent with the 2020 XMM-Newton intrinsic flux measurement. The data seem to indicate a drop of a factor ~ 2 in only 14 days.

We already knew from Section 3.2.4 that the intrinsic powerlaw component was also changing, and this analysis supports and extends such claim. Changes in accretion and obscuration are both responsible for the observed variability, but the intrinsic luminosity seems to be the main driver.

In the next Chapter we interpret the following results and propose a scenario, motivated by the detection in the 2020 XMM-Newton observations of fast accretion-disk scale winds.

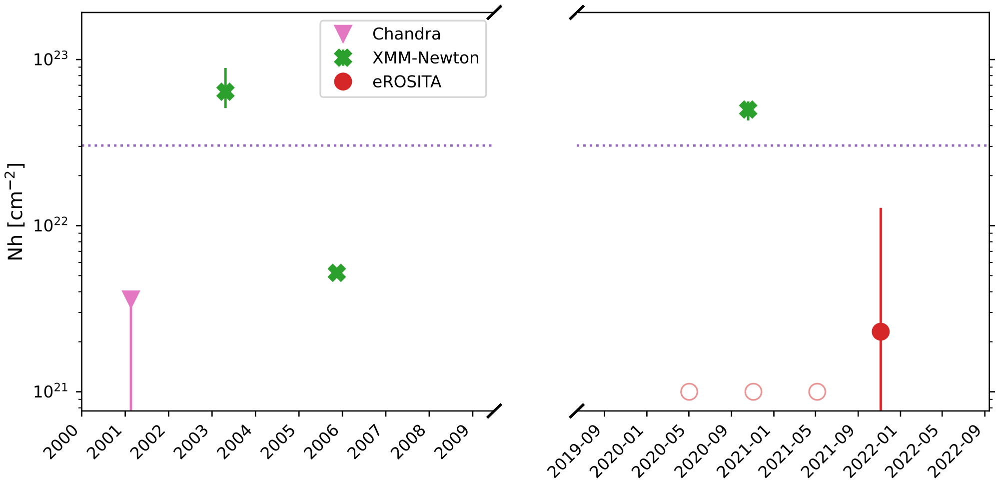

Figure 4.10: N_H inferred from model fitting as a function of time. The red hollow circles correspond to eRASS 1-3, where the N_H wasn't constrained by the fit, while the purple dotted line is the weighted average N_H. Chandra is reported as an upper limit at 90% confidence, while the error bars correspond to 1σ. A clear anticorrelation with flux is noticeable when comparing this plot with Fig. 4.9.

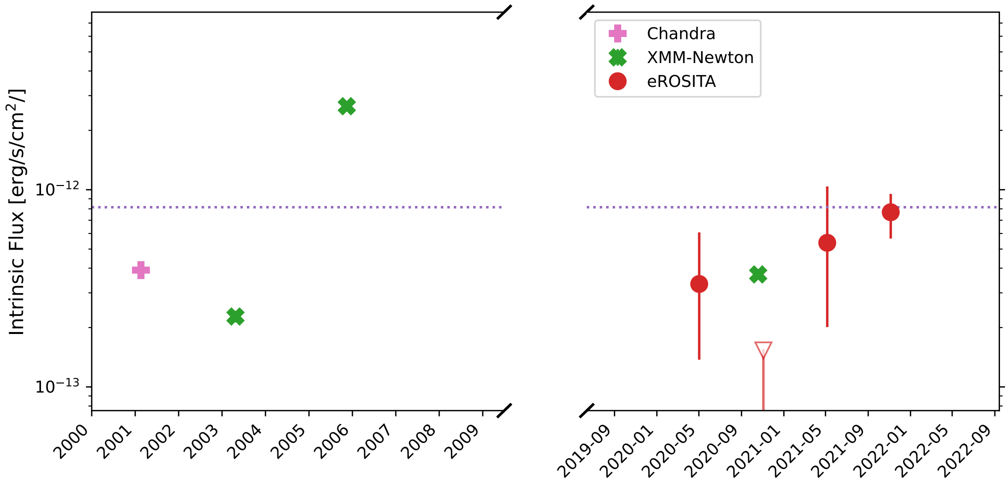

Figure 4.11: Powerlaw normalization inferred from model fitting as a function of time. The red triangle corresponds to eRASS2, where we interpret the normalization as an upper limit. While we report all errors at 1σ, we take the 90% confidence upper limit to show that the XMM-2020 and eRASS2 normalization are actually compatible.

Chapter 5

Summary & Discussion

5.1 Summary of the results

In this final Chapter, we discuss the physical implications of the results regarding feedback and variability for 2M0918. In order to do so, we first summarize such results, as obtained following our multi-epoch and multiwavelength spectral analysis of the source:

- Through our optical spectral analysis we have detected winds in the ionized gas phase (as traced by $[\mathrm{OIII}]_{5007}$ line emission) with velocities larger than 900 km/s, and energetics up to 10^{42} erg/s. We also measured a black hole mass of $log(M/M_{\odot}) = 7.1^{+0.4}_{-0.4}$.

- Through high counting statistics X-ray spectral analysis we have significantly detected ($P_{MC} > 99\%$) UFOs with velocities of $V_{out} = (0.15 \pm 0.1)$c and energetics of $\dot{K}_{out} = (1.8 \pm 1.2) \ \times 10^{43} erg/s$

- Finally, we have modeled 8 different observations taken with 4 different X-ray telescopes and built the 20-year-long lightcurve for 2M0918. This revealed significant variability on timescales of $\sim$ 2 years[1], with amplitude variations of more than 1 order of magnitude.

  The spectral analysis also allowed us to analyze the variability of single spectral components and parameters. Significant variations both in the intrinsic luminosity and in the column density of the absorber were found.

In the following Sections, we illustrate what these results tell us about 2M0918. We

---

[1] The rest frame variability timescale Δt_{rf} is equal to the observed variability timescale Δt_{obs} divided by a factor $(1 + z)$ to account for cosmological time dilation. As $(1 + z) = 1.149$ for 2M0918, the observed and restframe timescales are practically equal.

first present a discussion on the multiphase winds, and subsequently a discussion on variability, in which we also propose a model to explain the derived lightcurve.

5.2 Multiphase Outflows

In Chapter 3 we detected and quantified outflows in two different phases and scales for 2M0918.

Concerning the outflow in the ionized phase, we plot in Fig. 5.1 the scaling relations found for similar outflows in (F17) and Bischetti et al. (2019).

Two samples of representative AGN (the F17 sample and the AGN/composite subsample of Fluetsch et al. 2021) are plotted in the same figure. As it can be seen, 2M0918 does not deviate significantly from scaling relations found in literature for objects of similar type. The bolometric luminosity used to produce this plot is the SED-fitting derived $L_{bol} = 2.23 \times 10^{45}$ (See Chapter 1).

We check whether the AGN winds are consistent with known correlations also in the case of the UFO (Fig. 5.2). The figures are taken from Tombesi et al. (2013), and the blue datapoints correspond to UFOs, while the red are classified as Warm Absorbers, and the green are intermediate classes. As it can be seen, even in the X-ray the winds from 2M0918 are located in quite a populated parameter space. This is evident also in Fig. 5.3, where more correlations are plotted (see caption for more details).

From these plots and relations, one can deduct continuity between different phases of the winds. It's not possible for us to check this statement in the X-rays, as we are not explicitly modeling for Warm Absorber. We can however compare the optical and X-ray winds.

In Fig. 5.4, we plot $\dot{K}_{out}$ vs. L_{bol}, both for the UFO (blue) and the ionized outflows (orange), with the F17 ionized sample + UFO sample. We can see that the winds of 2M0918 lie at the bottom edge of their respective sample distributions, and that the UFO is more efficient ($\dot{K}_{out} \sim 0.01 \times L_{bol}$) than ionized wind ($\dot{K}_{out} \ll 0.01 \times L_{bol}$), in agreement to what was found in F17.

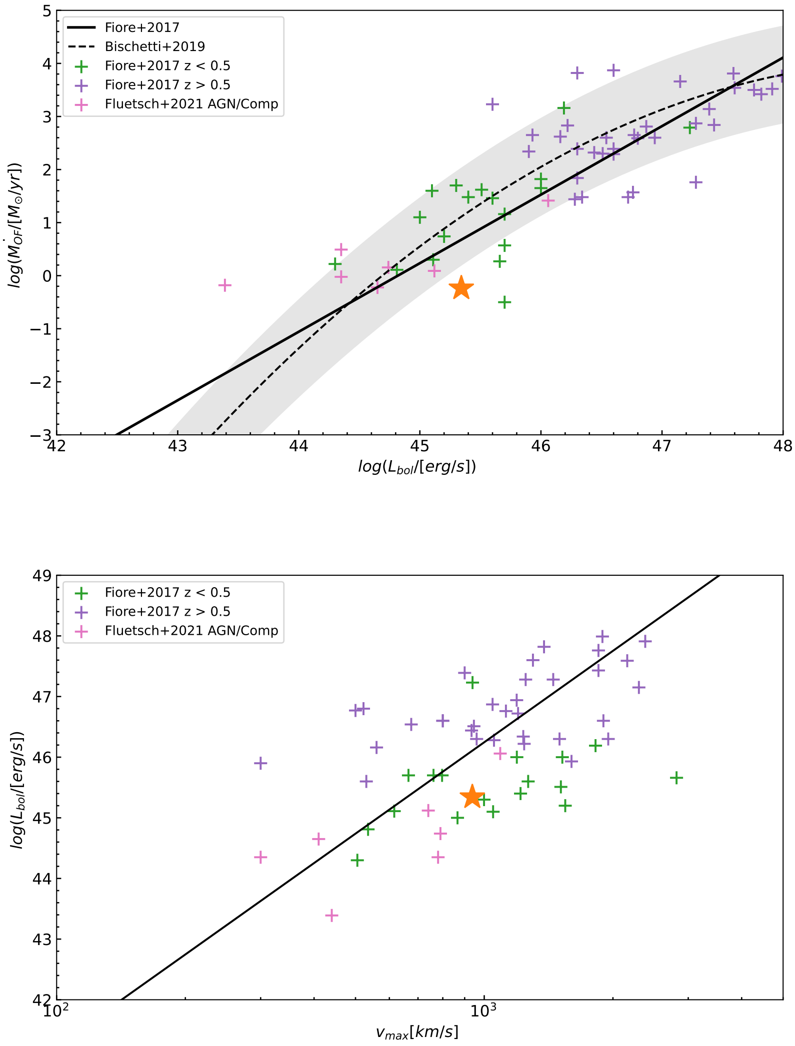

Figure 5.1: *Top:* Mass outflow rate vs. L_{bol}. *Bottom:* AGN bolometric luminosity vs. outflow velocity. In both plots, the solid line represents the scaling relation found in F17, and the green and purple crosses are the AGN sample from the same paper. The pink crosses are the Fluetsch et al. (2021) sample classified either as AGN or composite. The dashed line and shaded area in the top plot correspond to the scaling relation found in Bischetti et al. 2019. 2M0918 is represented by the orange star.

5.2.1 Momentum- vs. Energy-Driven Winds.

One of the most relevant features of our analysis is the simultaneous detection of multiphase winds. As mentioned in Chapter 1, AGN feedback is thought to propagate from small, sub-pc scales all the way to galaxy and group/cluster scales. Although this is commonly accepted both from a theoretical and computational point of view (King and Pounds 2015, Costa et al. 2020), the physics of feedback is still unclear. More specifically, it is yet not known whether winds propagate in a momentum-driven fashion, in which radiation cooling is faster than the outflow, and so energy is not conserved, or in an energy-driven scenario, in which cooling is negligible and the wind front expands adiabatically. While theory deems both mechanisms to be suitable, observations can constrain this by measuring disk- (UFOs) and galaxy-scale winds (Molecular or Ionized phase) in the same Galaxy. A collection of sources for which energetics in at least two phases are available has been compiled by Tozzi et al. (2021). However the sample is still small (12 sources + Mrk 509, reported in Zanchettin et al. 2021). With 2M0918 we are able to expand the sample of sources in which both a UFO and an ionized outflow are detected from 5 to 6 (+16%).

In Fig. 5.5 we plot the outflow momentum rate of 2M0918 normalized by L_{bol}/c as a function of outflow velocity. This is a standard diagnostic for feedback mechanisms, as winds conserving momentum in their propagation would lie on the dashed line parallel

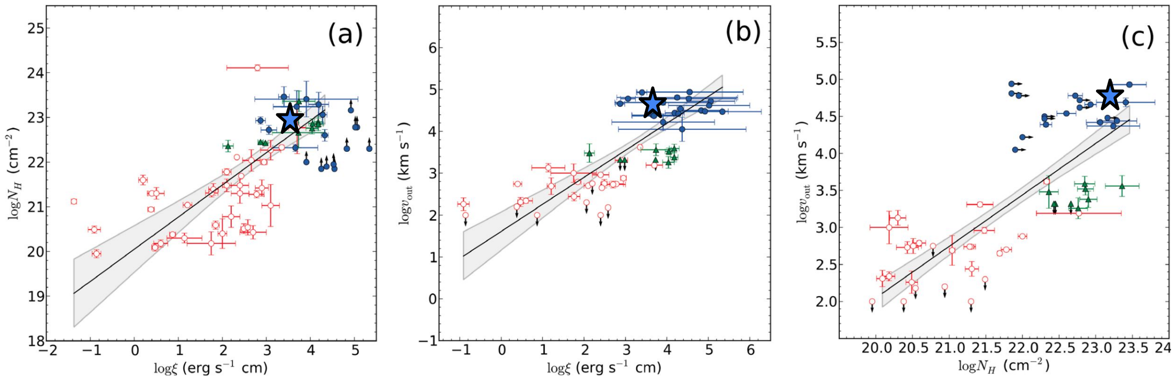

Figure 5.2: Correlation between X-ray wind parameters (ξ, Nh and v_{out}) taken from Tombesi et al. (2013). The red points are classified as Warm Absorbers, the blue as UFOs, and the green are an intermediate class. 2M0918 (the blue star) lies perfectly in the UFO region.

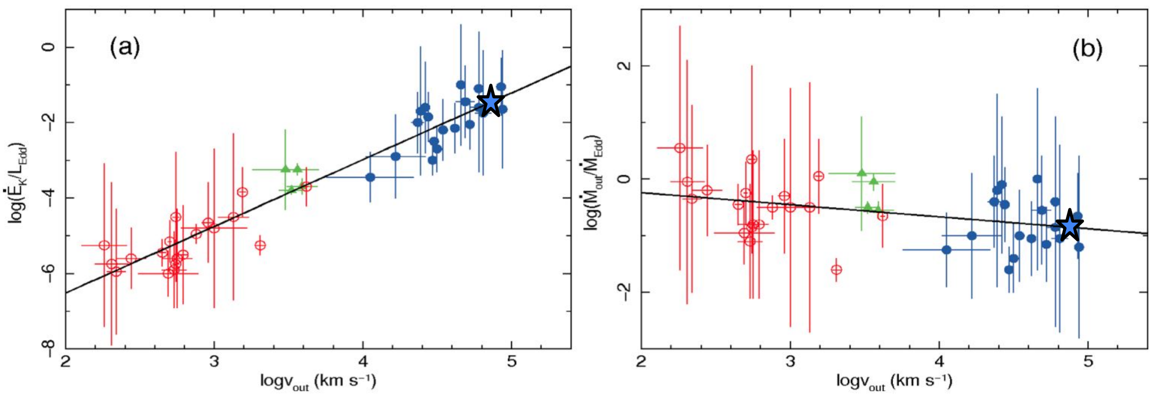

Figure 5.3: Correlations between normalized energetics ($\dot{M}_{out}$ and $\dot{E}_{kin}$ and outflow velocity, taken once again from Tombesi et al. (2013). The color scheme is the same as in Fig. 5.3, which shows without any doubt that the UFOs found in 2M0918 (blue star) are consistent with previous literature.

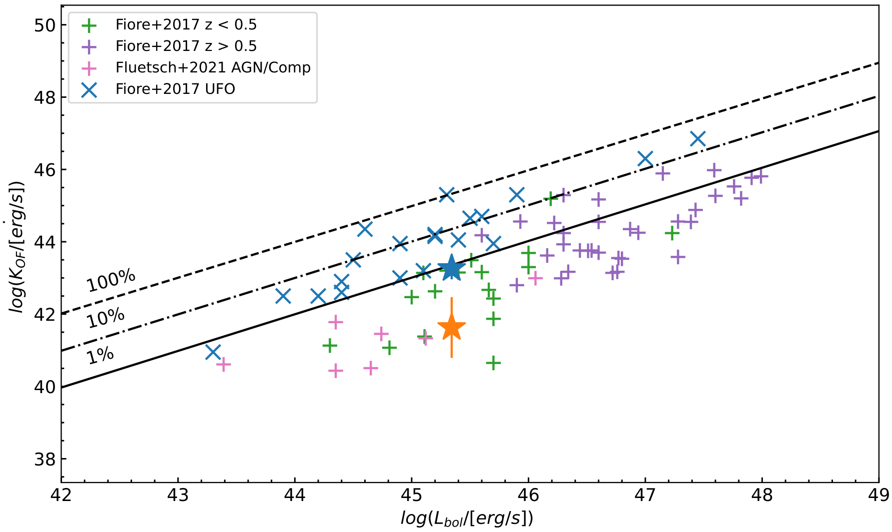

Figure 5.4: Kinetic coupling efficiencies of the winds in 2M0918, plotted over the F17 sample for both UFOs and Ionized winds and the Fluetsch et al. 2021 subsample defined as in Fig. 5.1. The blue and orange stars represent respectively the UFO and the ionized outflows in 2M0918.

to the x-axis, while energy-driven winds would follow the descending line.

2M0918 lies on the momentum-driven line, although the derived momentum outflow rate for the ionized outflow is only a lower limit, because of the uncertainty on the outflow radius (see Chapter 3), and therefore the measurements are also consistent with an energy-driven scenario. We do however stress that, in order for this to be true,

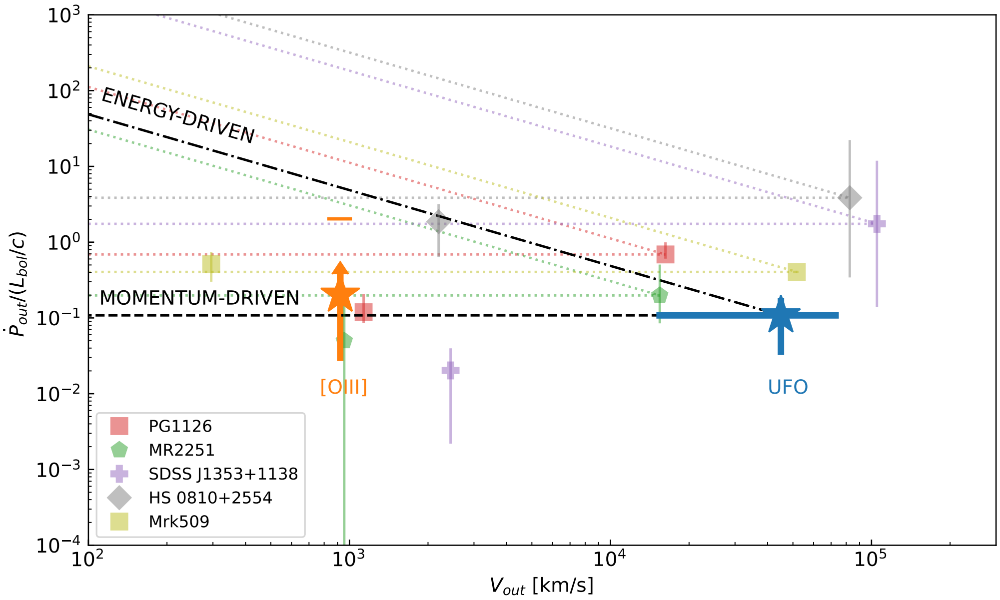

Figure 5.5: Momentum outflow rate normalized by L_{bol}/c vs. outflow velocity for 2M0918 (Orange + Blue stars). The two solid lines correspond to the two different feedback mechanisms described in the text, as labeled. In the background, we also plot the sources from Marasco et al. 2020 and Tozzi et al. 2021 where galaxy scale winds are ionized, each with their respective diagnostic line. The orange line above the [OIII] measurements stands to show what value of $\dot{P}_{out}/L_{bol}$ we would expect were the outflow radius 10x smaller (0.39 kpc). We consider this as a strong upper limit, as Ionized outflows are usually seen on scales of 100s to 1000s of pc.

the ionized outflow would have to be confined to a radius of 10s or few 100s of pc. Although not impossible, ionized outflows have typical radii of several 100s to 1000s of pc (F17), therefore we conclude that the momentum-driven scenario is more realistic.

In Fig. 5.6 we add 2M0918 (and Mrk 509, of which a multiphase wind analysis is presented in Zanchettin et al. 2021) to the plot initially presented in Marasco et al. (2020) and then extended in Tozzi et al. (2021). While we already knew that our source is associated with a momentum-driven scenario, it is worth mentioning that our results corroborate the conclusion drawn by both of the authors, which state that the energy- and momentum-driven models of feedback propagation explain well the observation at least up to galaxy-scales.

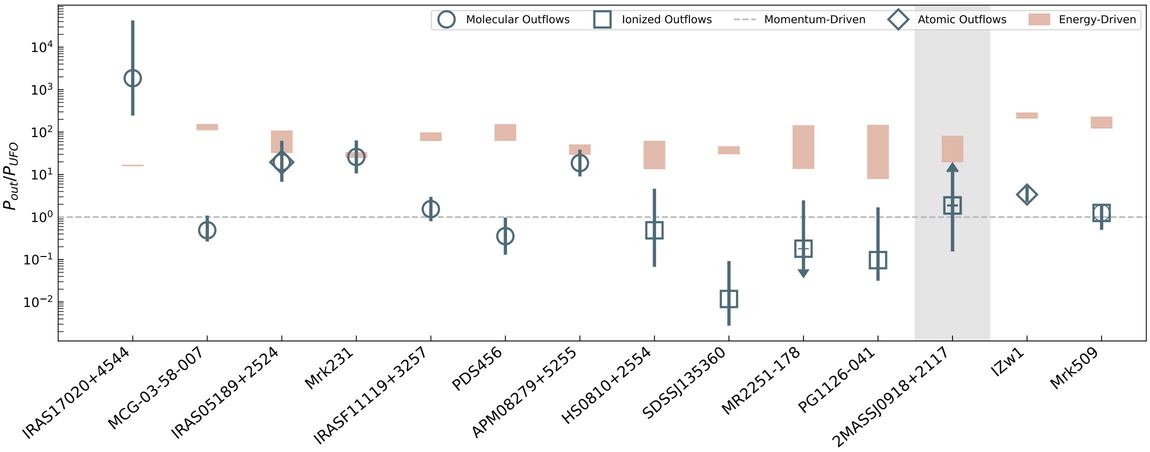

Figure 5.6: Updated figure from Tozzi et al. 2021, with the addition of 2M0918 (grey shaded area) and Mrk 509 (Zanchettin et al. 2021). This plot contains a compilation of sources for which UFO and galaxy-scale wind energetics are available, with the large-scale winds being either ionized, molecular or atomic. The ratio of the outflow momentum rates $\dot{P}_{out}/\dot{P}_{UFO}$ is plotted for each source, together with values predicted from theory for momentum- or energy-driven scenarios. The predicted value of $\dot{P}_{out}/\dot{P}_{UFO}$ for the energy-driven scenario can be estimated as the ratio v_{UFO}/v_{out} by imposing the conservation of energy, while the dashed line at y=1 is the prediction of a momentum-driven scenario.

5.2.2 Tracks in the $N_H - \lambda_{EDD}$ Plane and Bolometric Luminosities

AGN caught in active feedback phases are expected to be located in a specific region of the $N_H - \lambda_{EDD}$ plane (Fabian et al. 2008). This is due to the interplay between the intensity of radiation pressure from accretion and the gravitational force that acts on the dusty obscuring material. In other words, as the accretion rate increases, only very heavy nuclear absorbing clouds can survive the intense radiation field. In Fig. 5.7 we plot the N$_H - \lambda_{EDD}$ plane, as adapted from Ricci et al. (2022), with the density contours found from the Swift-BAT AGN Spectroscopic Survey sample (BASS) presented in the same paper. The track described by 2M0918 is included in the plot.

While the column density N_H was derived from the spectral analysis described in the previous Chapters, the Eddington ratio is defined as $\lambda_{EDD} = L_{bol}/L_{EDD}$, with the Eddington luminosity $L_{EDD} = 1.26 \times 10^{38}(M/M_{\odot})$ being a constant only dependent on the mass of the black hole (for a mass of $log(M/M_{\odot}) = 7.1^{+0.4}_{-0.4}$ this is

$L_{EDD} = (1.6^{+0.4}_{-0.6}) \times 10^{45} erg/s$). Using the same L_{bol} as in Sect. 5.2, derived from SED-fitting, would not tell us anything about variability, as the underlying assumption is time constancy. SED-fitting is generally considered the most reliable estimator for bolometric luminosity, as it takes into account multiwavelength emission, which can help disentangle degeneracies in the multiple emission components of galaxies/AGNs. However, by assuming that changes in the intrinsic X-ray emission are due to variations in accretion rate, deriving the bolometric luminosity from the 2-10 keV band is more suited to account for variability.

For our purposes, therefore, we estimate the AGN bolometric luminosity using the bolometric correction ($k_{bol} \equiv L_{bol}/L_{2-10}$). We use the bolometric corrections presented

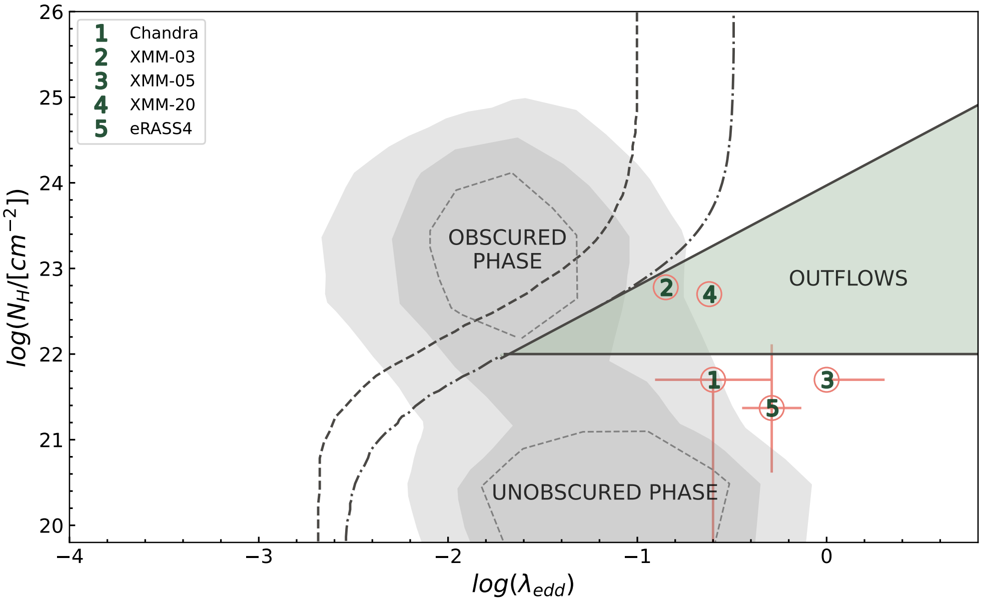

Figure 5.7: $N_H - \lambda_{EDD}$ plane, adapted from Ricci et al. (2022), and including density contours of the BASS XXXVII sample. The green region labeled as "OUTFLOWS" (also known in literature as forbidden region) corresponds to an N$_H$-λ_{EDD} space where absorption cannot be long-lived. The dashed line corresponds to the effective Eddington limit for dusty gas reported in Ishibashi et al. (2018), while the dash-dotted line is the effective Eddington limit when including infrared radiation trapping, from the same authors, adapted to the seminal values of Fabian et al. (2009) (solid black line constraining the forbidden region). 2M0918 entered and left the outflow region twice between 2001 and 2021, in agreement with the detection of outflows.

in Duras et al. (2020):

$$k_{bol}(L_{2-10}) = 15.33 \times \left[1 + \left(\frac{log(L_{2-10}/L_{\odot})}{11.48}\right)^{16.2}\right] \tag{5.1}$$

where $L_{\odot} = 3.9 \times 10^{33}$erg/s is the solar luminosity. By applying this equation to the Chandra, XMM-Newton(+NuSTAR) and eROSITA-eRASS4 2-10 keV fluxes we obtain the following λ_{EDD}:

	Chandra 01	**XMM-03**	**XMM-05**	**XMM+Nu 20**	**eRASS4 21**
$\lambda_{\mathbf{EDD}}$	0.25 ± 0.12	0.15 ± 0.02	$\gtrsim 1$	0.23 ± 0.02	0.51 ± 0.14

From these results and referring to Fig. 5.7, it is clear that 2M0918 lives in a scarcely populated region of the $N_H - \lambda_{EDD}$ plane, making the characterization of this source unique. Moreover, it is also evident that 2M0918 crossed multiple times the "forbidden" outflow region of the $N_H - \lambda_{EDD}$ plane. This is in agreement with the detection of UFOs and ionized winds. Changes in accretion rate are also significant, which provides us with further constraints on the nature of the variability of 2M0918, which we describe and interpret in the next Section.

We stress that the underlying assumption in this treatment is that winds are radiation-driven. It should be noted that other mechanisms, which we do not explore in this work, can also be responsible for the launching of winds. These include but are not limited to magnetically-driven winds, (e.g. Lynden-Bell 1996, Yuan et al. 2015) and thermally-driven winds (e.g. Begelman et al. 1983, Waters and Proga 2018).

5.3 Explaining the Variability of 2M0918

.

In Chapter 4 we derived the 20-year-long X-ray lightcurve from cross-instrument spectral analysis. The choice of individually modeling each spectrum, instead of simply fitting all observations with the same powerlaw model and looking for changes in normalization, enables, with some degree of uncertainty, to disentangle the variability of different components.

The spectral variability observed in 2M0918 is sufficiently drastic in order to classify this as a CL-AGN. Recalling Section 1.2 of Chapter 1 (and Ricci and Trakhtenbrot 2022, which is the main source for this section of the discussion), CL-AGNs can be divided into two classes based on whether the variability is to be ascribed to changes in the l.o.s obscuring material (*Changing-Obscuration* AGN, CO-AGN Mereghetti et al. 2021) or to changes in accretion state (*Changing-State* AGN, CS-AGN, Graham et al. 2020). X-ray CL-AGN are typically associated with CO-AGN, and some degree of obscuration variability is observable in a large fraction of the general AGN population (Risaliti et al. 2002, Markowitz et al. 2014). This is usually attributed to eclipsing events from gas clouds in the BLR (this is the case for the famous NGC1365, Risaliti et al. 2009,Maiolino et al. 2010) or the clumpy nature of the dusty torus (see Ramos-Almeida and Ricci 2017 for a review). There is no particular reason why we shouldn't consider these as valid scenarios for the observed variability of 2M0918: timescales range from days to years and the variations in N_H are well within the observed range. However, these models don't predict or require any variation in the AGN accretion rate, which we do observe indeed (Fig. 5.7). We would then have to explain the accretion changes as uncorrelated to the obscuration and the result of disk instabilities (Śniegowska et al. 2022). We stress once again that one should still keep these models in mind as possible explanations of the observed lightcurve, however, it is also possible to explore the plausibility of a connection between the two phenomena.

In the last few years, an alternative mechanism in which the CO-AGN event is explained in terms of obscuration due to outflowing gas material has been proposed for some sources (such as NGC5548, Kaastra et al. 2014, NGC3227, Beuchert et al. 2015 and NGC378, Mehdipour et al. 2017). In these cases, the absorber is ionized to some degree, but for low SNR observations, it's impact on the spectra can mimic that of neutral gas.

For 2M0918 the ionization parameter ξ was observed to increase by an order of magnitude between 2005 and 2020 (the two observation sets in which the SNR was high enough to disentangle the degeneracy in the ZXIPCF parameters), concurrent with an increase in column density. These are the same observations in which UFO signatures were detected. At the same time between 2003 and 2020, as it's shown in Fig. 5.7, the AGN entered, crossed, and left the $Nh - \lambda$ plane region in which sources are expected to be in the outflowing phase. We believe that, from these considerations, the observed variability can be associated with outflowing gas.

We propose the following scenario, which explains the variability in accretion rate, absorber column density, and the appearance of winds in one unified scheme:

- In **2001** the source was observed in a low-Eddington state. Some amount of clumpy obscuring gas was present in the nuclear regions as it is currently accepted in AGN models, but was not significantly obscuring the source.
- In **2003** the source was obscured, due to gas intercepting the line of sight. This transition could either be explained in terms of simple Keplerian orbit of an uneven, clumpy medium, but also as an inflowing motion of the gas. The 2005 observations favour the second option (see next bullet point).
- In **2005** we observed the AGN in a brighter state than before, accreting at the Eddington limit. This may be due to the AGN accreting part of the gas that caused the increase in obscuration in 2003, with a resulting increase in intrinsic luminosity and decrease in column density.
- in **2020** the source appeared to be obscured once again, but this time the absorbing material was ionized to a mild degree. The AGN dimmed back to its original low-Eddington state. We attribute the absorption to outflowing clouds intercepting the line of sight. These clouds were pushed and ionized by the UFO of which we saw hints in the 2005 spectra and found confirmation in the 2020 observations, as a result of the high radiation field generated from the previous accretion event.
- At the end of **2021** the source went back to its low-Eddington unobscured state, as the UFOs successfully cleared the surrounding gas. The AGN is now slightly brighter than it was in 2001, but not significantly.

Fig. 5.8 shows a cartoon of the proposed scenario.

Although we strongly support this model, based on our analysis, it must be noted that the timescales at which accretion rate changes propagate through standard SS79 accretion disks are the viscous timescales:

$$t_{vis} \sim 400 \left(\frac{H/R}{0.05}\right)^{-2} \left(\frac{\alpha}{0.03}\right)^{-1} \left(\frac{R}{150 r_g}\right)^{3/2} M_8 \ yrs \tag{5.2}$$

Where H/R measures the thickness of the disk, α is the viscous coefficient, R the radius at which the timescale is computed, in units of gravitational radii, and M_8 is the SMBH mass in units of $10^8 M_\odot$. Assuming standard prescriptions the viscous timescales for 2M0918 are of the order of 40 years. This is a factor ~ 10 times longer than the observed variability of 2 years, which would make our observations incompatible with theoretical predictions. However, it must be noted that the standard α-disk has been recognized by theorists as an oversimplification for quite some time, and some solutions, such as a thick disk, have been proposed to release the standard disk assumption, which would also shrink the timescales for accretion rate changes (See Lawrence 2018 for a discussion; see also Komossa and Grupe 2022 and references therein).

We also note that the episodic accretion event doesn't necessarily have to be communicated to the whole disk in order for luminosity to increase. In the case of Tidal Disruption Events (TDEs), which are events in which Black Holes accrete stars passing in their vicinity, super-Eddington accretion disks can form on timescales of days (See e.g. Gezari 2021 for a review). Although gas accretion and TDEs are different phenomena, we believe that variations in λ_{EDD} can in principle happen on timescales shorter than the ones predicted by Eq. 5.2 even for gas streams. For example, this

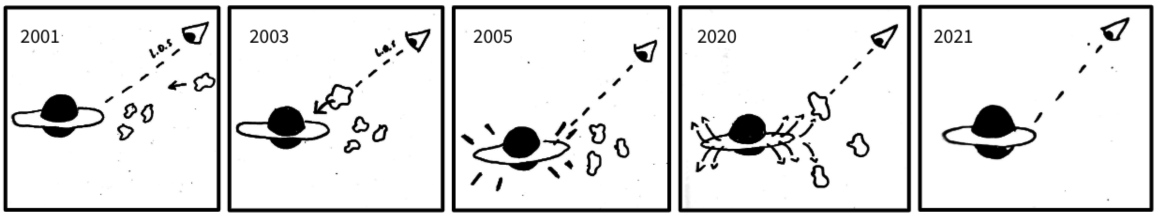

Figure 5.8: Cartoon of the proposed variability scenario (not to scale). Note that the episodic accretion is most likely happening in the form of a stream, rather than the single-cloud accretion event drawn in the simplistic figure.

could be the case if the accretion stream was not coplanar with the accretion disk (e.g. Chan et al. 2019). This possibility is corroborated by the fact that accretion in 2005 is consistent with being super-Eddington, but further investigation is necessary.

5.4 Future perspectives

We believe a monitoring of the source with simultaneous X-ray and Optical observations will help further constrain the nature of the variability of 2M0918. As eROSITA operations will hopefully soon resume, we will be able to scan the source every 6 months for at least 2 more years, which will reveal whether the source stabilized or is still varying. In addition, the future X-ray mission Einstein Probe (Yuan et al. 2022), dedicated to the monitoring of transients, will also provide further constraints on the variability of 2M0918.

Regarding Optical/UV, as an extension of this work, we will also analyze the data of the Optical Monitor OM on board of XMM-Newton, to fully understand whether the change in intrinsic X-ray luminosity can be related to accretion variability.

Furthermore, optical IFU observations will allow us to directly infer the geometry of the outflows, tightening our constraints on the ionized outflow energetics. This approach has been extensively used both at low-z (e.g Venturi et al. 2021, Speranza et al. 2022) and at high-z (e.g. XID2028, Cresci et al. 2015, Cresci et al. 2023). The use of mm/sub-mm facilities, such as the Atacama Large Millimeter Array (ALMA), will allow us to probe the molecular phase of the outflow, which remains as of now totally unprobed.

In these regards, we are currently working on proposals for ALMA and the optical IFU Multi Unit Spectroscopic Explorer (MUSE), in order to obtain such data.

Bibliography

Antonucci, RRJ and JS Miller (1985). "Spectropolarimetry and the nature of NGC 1068". In: *The Astrophysical Journal* 297, pp. 621–632.

Arnaud, KA (1996). "XSPEC: the first ten years". In: *Astronomical data analysis software and systems V*. Vol. 101, p. 17.

Begelman, Mitchell C et al. (1983). "Compton heated winds and coronae above accretion disks. I Dynamics". In: *The Astrophysical Journal* 271, pp. 70–88.

Beuchert, Tobias et al. (2015). "A variable-density absorption event in NGC 3227 mapped with Suzaku and Swift". In: *Astronomy & Astrophysics* 584, A82.

Bianchi, Stefano et al. (2009). "CAIXA: a catalogue of AGN in the XMM-Newton archive-I. Spectral analysis". In: *Astronomy & Astrophysics* 495.2, pp. 421–430.

Bischetti, M et al. (2019). "The gentle monster PDS 456-Kiloparsec-scale molecular outflow and its implications for QSO feedback". In: *Astronomy & Astrophysics* 628, A118.

Blandford, Roger et al. (2019). "Relativistic jets from active galactic nuclei". In: *Annual Review of Astronomy and Astrophysics* 57, pp. 467–509.

Boquien, M et al. (2019). "CIGALE: a python code investigating GALaxy emission". In: *Astronomy & Astrophysics* 622, A103.

Boroson, Todd A and Richard F Green (1992). "The emission-line properties of low-redshift quasi-stellar objects". In: *The Astrophysical Journal Supplement Series* 80, pp. 109–135.

Bronzwaer, Thomas and Heino Falcke (2021). "The nature of black hole shadows". In: *The Astrophysical Journal* 920.2, p. 155.

Brunner, H et al. (2022). "The eROSITA Final Equatorial Depth Survey (eFEDS)-X-ray catalogue". In: *Astronomy & Astrophysics* 661, A1.

Brusa, M et al. (2018). “Molecular outflow and feedback in the obscured quasar XID2028 revealed by ALMA”. In: *Astronomy & Astrophysics* 612, A29.

Brusa, M et al. (2015). “X-shooter reveals powerful outflows in z 1.5 X-ray selected obscured quasi-stellar objects”. In: *Monthly Notices of the Royal Astronomical Society* 446.3, pp. 2394–2417.

Buchner, J (Apr. 2021). “UltraNest - a robust, general purpose Bayesian inference engine”. In: *The Journal of Open Source Software* 6.60, 3001, p. 3001. DOI: `10.21105/joss.03001`. arXiv: `2101.09604 [stat.CO]`.

Buchner, J et al. (2014). “X-ray spectral modelling of the AGN obscuring region in the CDFS: Bayesian model selection and catalogue”. In: *Astronomy & Astrophysics* 564, A125.

Cano-Díaz, M et al. (2012). “Observational evidence of quasar feedback quenching star formation at high redshift”. In: *Astronomy & Astrophysics* 537, p. L8.

Cappi, M et al. (2009). “X-ray evidence for a mildly relativistic and variable outflow in the luminous Seyfert 1 galaxy Mrk 509”. In: *Astronomy & Astrophysics* 504.2, pp. 401–407.

Cash, Webster (1979). “Parameter estimation in astronomy through application of the likelihood ratio”. In: *The Astrophysical Journal* 228, pp. 939–947.

Chan, Chi-Ho et al. (2019). “Tidal disruption events in active galactic nuclei”. In: *The Astrophysical Journal* 881.2, p. 113.

Cicone, C et al. (2012). “The physics and the structure of the quasar-driven outflow in Mrk 231”. In: *Astronomy & Astrophysics* 543, A99.

Cicone, Claudia et al. (2018). “The largely unconstrained multiphase nature of outflows in AGN host galaxies”. In: *Nature Astronomy* 2.3, pp. 176–178.

Costa, Tiago et al. (2014). “Feedback from active galactic nuclei: energy-versus momentum-driving”. In: *Monthly Notices of the Royal Astronomical Society* 444.3, pp. 2355–2376.

Costa, Tiago et al. (2020). “Powering galactic superwinds with small-scale AGN winds”. In: *Monthly Notices of the Royal Astronomical Society* 497.4, pp. 5229–5255.

Cresci, Giovanni et al. (2015). “Blowin’in the wind: both “negative” and “positive” feedback in an obscured high-z quasar”. In: *The Astrophysical Journal* 799.1, p. 82.

Cresci, Giovanni et al. (2023). “Bubbles and outflows: the novel JWST/NIRSpec view of the z= 1.59 obscured quasar XID2028”. In: *arXiv preprint arXiv:2301.11060*.

Cutri, Roc M et al. (2002). “The 2MASS red AGN survey”. In: *International Astronomical Union Colloquium*. Vol. 184. Cambridge University Press, pp. 127–136.

Dadina, M. (July 2008). “Seyfert galaxies in the local Universe (z $\leq$ 0.1): the average X-ray spectrum as seen by BeppoSAX”. In: 485.2, pp. 417–424. DOI: `10.1051/0004-6361:20077569`. arXiv: `0801.4338 [astro-ph]`.

Di Matteo, Tiziana et al. (2005). “Energy input from quasars regulates the growth and activity of black holes and their host galaxies”. In: *nature* 433.7026, pp. 604–607.

Duras, F et al. (2020). “Universal bolometric corrections for active galactic nuclei over seven luminosity decades”. In: *Astronomy & Astrophysics* 636, A73.

Event Horizon Telescope Collaboration et al. (2019a). “First M87 event horizon telescope results. I. The shadow of the supermassive black hole”. In: *Astrophys. J. Lett* 875.1, p. L1.

Event Horizon Telescope Collaboration et al. (Apr. 2019b). “First M87 Event Horizon Telescope Results. II. Array and Instrumentation”. In: 875.1, L2, p. L2. DOI: `10.3847/2041-8213/ab0c96`. arXiv: `1906.11239 [astro-ph.IM]`.

Event Horizon Telescope Collaboration et al. (2022). “First Sagittarius A* Event Horizon Telescope results. I. The shadow of the supermassive black hole in the center of the Milky Way”. In: *The Astrophysical Journal Letters* 930.2, p. L12.

Fabian, AC et al. (2015). “Properties of AGN coronae in the NuSTAR era”. In: *Monthly Notices of the Royal Astronomical Society* 451.4, pp. 4375–4383.

Fabian, AC et al. (2009). “Radiation pressure and absorption in AGN: results from a complete unbiased sample from Swift”. In: *Monthly Notices of the Royal Astronomical Society: Letters* 394.1, pp. L89–L92.

Fabian, AC et al. (2008). “The effect of radiation pressure on dusty absorbing gas around active galactic nuclei”. In: *Monthly Notices of the Royal Astronomical Society: Letters* 385.1, pp. L43–L47.

Fabian, Andrew C (2012). “Observational evidence of active galactic nuclei feedback”. In: *Annual Review of Astronomy and Astrophysics* 50, pp. 455–489.

Ferrarese, Laura and David Merritt (2000). “A fundamental relation between supermassive black holes and their host galaxies”. In: *The Astrophysical Journal* 539.1, p. L9.

Fiore, Fabrizio et al. (2017). “AGN wind scaling relations and the co-evolution of black holes and galaxies”. In: *Astronomy & Astrophysics* 601, A143.

Fluetsch, Andrin et al. (2021). “Properties of the multiphase outflows in local (ultra) luminous infrared galaxies”. In: *Monthly Notices of the Royal Astronomical Society* 505.4, pp. 5753–5783.

Foreman-Mackey, Daniel (2016). “corner.py: Scatterplot matrices in Python”. In: *The Journal of Open Source Software* 1.2, p. 24. DOI: `10.21105/joss.00024`. URL: `https://doi.org/10.21105/joss.00024`.

Fruscione, Antonella et al. (2006). “CIAO: Chandra’s data analysis system”. In: *Observatory Operations: Strategies, Processes, and Systems*. Vol. 6270. SPIE, pp. 586–597.

Gebhardt, Karl et al. (2000). “A relationship between nuclear black hole mass and galaxy velocity dispersion”. In: *The Astrophysical Journal* 539.1, p. L13.

Georgantopoulos, Ioannis et al. (2013). “The XMM deep survey in the CDF-S-IV. Compton-thick AGN candidates”. In: *Astronomy & Astrophysics* 555, A43.

George, IM and AC Fabian (1991). “X-ray reflection from cold matter in active galactic nuclei and X-ray binaries”. In: *Monthly Notices of the Royal Astronomical Society* 249.2, pp. 352–367.

Gezari, Suvi (2021). “Tidal disruption events”. In: *Annual Review of Astronomy and Astrophysics* 59, pp. 21–58.

Gezari, Suvi et al. (2017). “iPTF Discovery of the Rapid “Turn-on” of a Luminous Quasar”. In: *The Astrophysical Journal* 835.2, p. 144.

Gitti, Myriam et al. (2006). “Multifrequency VLA radio observations of the X-ray cavity cluster of galaxies RBS797: evidence of differently oriented jets”. In: *Astronomy & Astrophysics* 448.3, pp. 853–860.

Giustini, Margherita and Daniel Proga (2019). “A global view of the inner accretion and ejection flow around super massive black holes-Radiation-driven accretion disk winds in a physical context”. In: *Astronomy & Astrophysics* 630, A94.

Giustini, Margherita et al. (2011). “Variable X-ray absorption in the mini-BAL QSO PG 1126-041”. In: *Astronomy & Astrophysics* 536, A49.

Graham, Matthew J et al. (2020). “Understanding extreme quasar optical variability with CRTS–II. Changing-state quasars”. In: *Monthly Notices of the Royal Astronomical Society* 491.4, pp. 4925–4948.

Greene, Jenny E and Luis C Ho (2005). “Estimating black hole masses in active galaxies using the Hα emission line”. In: *The Astrophysical Journal* 630.1, p. 122.

Gunn, James E. et al. (Apr. 2006). “The 2.5 m Telescope of the Sloan Digital Sky Survey”. In: 131.4, pp. 2332–2359. DOI: `10.1086/500975`. arXiv: `astro-ph/0602326 [astro-ph]`.

Guo, Hengxiao et al. (2018). “PyQSOFit: Python code to fit the spectrum of quasars”. In: *Astrophysics Source Code Library*, ascl–1809.

Häring, Nadine and Hans-Walter Rix (2004). “On the black hole mass-bulge mass relation”. In: *The Astrophysical Journal* 604.2, p. L89.

Harrison, Christopher Mark (2016). *Observational constraints on the influence of active galactic nuclei on the evolution of galaxies*. Springer.

Harrison, CM (2017). “Impact of supermassive black hole growth on star formation”. In: *Nature Astronomy* 1.7, p. 0165.

Harrison, Fiona A. et al. (June 2013). “The Nuclear Spectroscopic Telescope Array (NuSTAR) High-energy X-Ray Mission”. In: 770.2, 103, p. 103. DOI: `10.1088/0004-637X/770/2/103`. arXiv: `1301.7307 [astro-ph.IM]`.

Ishibashi, W et al. (2018). “The energetics of AGN radiation pressure-driven outflows”. In: *Monthly Notices of the Royal Astronomical Society* 476.1, pp. 512–519.

Jansen, F. et al. (Jan. 2001). “XMM-Newton observatory. I. The spacecraft and operations”. In: 365, pp. L1–L6. DOI: `10.1051/0004-6361:20000036`.

Kaastra, JS and JAM Bleeker (2016). “Optimal binning of X-ray spectra and response matrix design”. In: *Astronomy & Astrophysics* 587, A151.

Kaastra, JS et al. (2014). “A fast and long-lived outflow from the supermassive black hole in NGC 5548”. In: *Science* 345.6192, pp. 64–68.

Kalberla, Peter MW et al. (2005). “The leiden/argentine/bonn (lab) survey of galactic hi-final data release of the combined lds and iar surveys with improved stray-radiation corrections”. In: *Astronomy & Astrophysics* 440.2, pp. 775–782.

Kallman, Tim (1999). “XSTAR: A program for calculating conditions and spectra of photoionized gases”. In: *Astrophysics Source Code Library*, ascl–9910.

Kang, Jia-Lai and Jun-Xian Wang (2022). “The X-ray coronae in NuSTAR bright active galactic nuclei”. In: *The Astrophysical Journal* 929.2, p. 141.

Kaspi, Shai et al. (2005). “The relationship between luminosity and broad-line region size in active galactic nuclei”. In: *The Astrophysical Journal* 629.1, p. 61.

King, Andrew and Ken Pounds (2015). “Powerful outflows and feedback from active galactic nuclei”. In: *Annual Review of Astronomy and Astrophysics* 53, pp. 115–154.

Komossa, S and D Grupe (2022). “Extreme Accretion Events: TDEs and Changing-Look AGN”. In: *arXiv preprint arXiv:2212.10331*.

Kormendy, John and Luis C Ho (2013). “Coevolution (or not) of supermassive black holes and host galaxies”. In: *Annual Review of Astronomy and Astrophysics* 51, pp. 511–653.

Lanzuisi, G et al. (2018). “The Chandra COSMOS legacy survey: compton thick AGN at high redshift”. In: *Monthly Notices of the Royal Astronomical Society* 480.2, pp. 2578–2592.

Lanzuisi, G et al. (2013). “The Chandra-COSMOS survey–IV. X-ray spectra of the bright sample”. In: *Monthly Notices of the Royal Astronomical Society* 431.1, pp. 978–996.

Lawrence, Andy (2018). “Quasar viscosity crisis”. In: *Nature Astronomy* 2.2, pp. 102–103.

Liu, T et al. (2022). “The eROSITA Final Equatorial-Depth Survey (eFEDS)-The AGN catalog and its X-ray spectral properties”. In: *Astronomy & Astrophysics* 661, A5.

Longair, Malcolm S (2011). *High energy astrophysics.* Cambridge university press.

Longair, Malcolm S. (2011). *High Energy Astrophysics.*

Luo, B. et al. (Jan. 2017). “The Chandra Deep Field-South Survey: 7 Ms Source Catalogs”. In: 228.1, 2, p. 2. DOI: 10.3847/1538-4365/228/1/2. arXiv: 1611.03501 [astro-ph.GA].

Lynden-Bell, D (1996). “Magnetic collimation by accretion discs of quasars and stars”. In: *Monthly Notices of the Royal Astronomical Society* 279.2, pp. 389–401.

Magorrian, John et al. (1998). “The demography of massive dark objects in galaxy centers”. In: *The Astronomical Journal* 115.6, p. 2285.

Maiolino, R et al. (2010). ““Comets” orbiting a black hole”. In: *Astronomy & Astrophysics* 517, A47.

Marasco, A et al. (2020). “Galaxy-scale ionised winds driven by ultra-fast outflows in two nearby quasars”. In: *Astronomy & Astrophysics* 644, A15.

Markowitz, AG et al. (2014). “First X-ray-based statistical tests for clumpy-torus models: eclipse events from 230 years of monitoring of Seyfert AGN”. In: *Monthly Notices of the Royal Astronomical Society* 439.2, pp. 1403–1458.

Matt, Giorgio et al. (2003). “Changing look: from Compton-thick to Compton-thin, or the rebirth of fossil active galactic nuclei”. In: *Monthly Notices of the Royal Astronomical Society* 342.2, pp. 422–426.

Matzeu, GA et al. (2017). “Evidence for a radiatively driven disc-wind in PDS 456?” In: *Monthly Notices of the Royal Astronomical Society: Letters* 472.1, pp. L15–L19.

Matzeu, GA et al. (2022). “Supermassive Black Hole Winds in X-rays–SUBWAYS. I. Ultra-fast outflows in QSOs beyond the local Universe”. In: *arXiv preprint arXiv:2212.02960*.

Mehdipour, M et al. (2017). “Chasing obscuration in type-I AGN: discovery of an eclipsing clumpy wind at the outer broad-line region of NGC 3783”. In: *Astronomy & Astrophysics* 607, A28.

Mereghetti, Sandro et al. (2021). “Time domain astronomy with the THESEUS satellite”. In: *Experimental Astronomy* 52.3, pp. 309–406.

Merloni, A. et al. (2012). *eROSITA Science Book: Mapping the Structure of the Energetic Universe*. DOI: 10.48550/ARXIV.1209.3114. URL: https://arxiv.org/abs/1209.3114.

Merloni, A et al. (2014). “The incidence of obscuration in active galactic nuclei”. In: *Monthly Notices of the Royal Astronomical Society* 437.4, pp. 3550–3567.

Miniutti, G and AC Fabian (2006). “Discovery of a relativistic Fe line in PG 1425+ 267 with XMM-Newton and study of its short time-scale variability”. In: *Monthly Notices of the Royal Astronomical Society* 366.1, pp. 115–124.

Miniutti, G et al. (2007). “IRAS 13197- 1627 has them all: Compton-thin absorption, photoionized gas, thermal plasmas and a broad Fe line”. In: *Monthly Notices of the Royal Astronomical Society* 375.1, pp. 227–239.

Miniutti, G et al. (2014). “The properties of the clumpy torus and BLR in the polar-scattered Seyfert 1 galaxy ESO 323–G77 through X-ray absorption variability”. In: *Monthly Notices of the Royal Astronomical Society* 437.2, pp. 1776–1790.

Morganti, Raffaella et al. (2016). “Another piece of the puzzle: The fast H i outflow in Mrk 231”. In: *Astronomy & Astrophysics* 593, A30.

Nandra, K and Kenneth Alwyne Pounds (1994). “GINGA observations of the X-ray spectra of Seyfert galaxies”. In: *Monthly Notices of the Royal Astronomical Society* 268.2, pp. 405–429.

Nardini, Emanuele and Kastytis Zubovas (2018). “Multi-phase outflows as probes of AGN accretion history”. In: *Monthly Notices of the Royal Astronomical Society* 478.2, pp. 2274–2280.

Nardini, EMANUELE et al. (2015). “Black hole feedback in the luminous quasar PDS 456”. In: *Science* 347.6224, pp. 860–863.

Netzer, Hagai (2015). “Revisiting the unified model of active galactic nuclei”. In: *Annual Review of Astronomy and Astrophysics* 53, pp. 365–408.

Osterbrock, Donald E (1981). “Seyfert galaxies with weak broad H alpha emission lines”. In: *The Astrophysical Journal* 249, pp. 462–470.

Osterbrock, Donald E and Gary J Ferland (2006). *Astrophysics Of Gas Nebulae and Active Galactic Nuclei*. University science books.

Padovani, Paolo et al. (2017). “Active galactic nuclei: what’s in a name?” In: *The Astronomy and Astrophysics Review* 25, pp. 1–91.

Pavlinsky, M et al. (2021). “The ART-XC telescope on board the SRG observatory”. In: *Astronomy & Astrophysics* 650, A42.

Piconcelli, E et al. (2004). “Evidence for a multizone warm absorber in the XMM—Newton spectrum of Markarian 304”. In: *Monthly Notices of the Royal Astronomical Society* 351.1, pp. 161–168.

Pillepich, Annalisa et al. (2021). “X-ray bubbles in the circumgalactic medium of TNG50 Milky Way-and M31-like galaxies: signposts of supermassive black hole activity”. In: *Monthly Notices of the Royal Astronomical Society* 508.4, pp. 4667–4695.

Pounds, KA and Belinda Jane Wilkes (2007). “Comparison of high-and low-state X-ray spectra in the type 1.5 quasi-stellar object 2MASS 0918+ 2117”. In: *Monthly Notices of the Royal Astronomical Society* 380.4, pp. 1341–1347.

Pounds, Kenneth A and Kim L Page (2006). “Confirming the high velocity outflow in PG1211+ 143”. In: *Monthly Notices of the Royal Astronomical Society* 372.3, pp. 1275–1278.

Pounds, Kenneth A et al. (2003). “A high-velocity ionized outflow and XUV photosphere in the narrow emission line quasar PG1211+ 143”. In: *Monthly Notices of the Royal Astronomical Society* 345.3, pp. 705–713.

Predehl, P. et al. (2021). “The eROSITA X-ray telescope on SRG”. In: *Astronomy &amp Astrophysics* 647, A1. DOI: 10.1051/0004-6361/202039313. URL: https://doi.org/10.1051%2F0004-6361%2F202039313.

Protassov, Rostislav et al. (2002). “Statistics, handle with care: detecting multiple model components with the likelihood ratio test”. In: *The Astrophysical Journal* 571.1, p. 545.

Ramos-Almeida, Cristina and Claudio Ricci (2017). “Nuclear obscuration in active galactic nuclei”. In: *Nature Astronomy* 1.10, pp. 679–689.

Ricci, C et al. (2022). “BASS XXXVII: The role of radiative feedback in the growth and obscuration properties of nearby supermassive black holes”. In: *The Astrophysical Journal* 938.1, p. 67.

Ricci, Claudio (2011). “Active Galactic Nuclei at hard X-ray energies: absorption, reflection and the unified model”. PhD thesis. University of Geneva.

Ricci, Claudio and Benny Trakhtenbrot (2022). “Changing-look Active Galactic Nuclei”. In: *arXiv preprint arXiv:2211.05132*.

Ricci, Claudio et al. (2018). “BAT AGN Spectroscopic Survey–XII. The relation between coronal properties of active galactic nuclei and the Eddington ratio”. In: *Monthly Notices of the Royal Astronomical Society* 480.2, pp. 1819–1830.

Ricci, Claudio et al. (2017). “BAT AGN spectroscopic survey. V. X-ray properties of the Swift/BAT 70-month AGN catalog”. In: *The Astrophysical Journal Supplement Series* 233.2, p. 17.

Risaliti, G et al. (2007). “Occultation Measurement of the Size of the X-Ray-emitting Region in the Active Galactic Nucleus of NGC 1365”. In: *The Astrophysical Journal* 659.2, p. L111.

Risaliti, G et al. (2002). “Ubiquitous variability of X-ray-absorbing column densities in Seyfert 2 galaxies”. In: *The Astrophysical Journal* 571.1, p. 234.

Risaliti, Guido et al. (2009). “Variable partial covering and a relativistic iron line in NGC 1365”. In: *The Astrophysical Journal* 696.1, p. 160.

Schlegel, David J et al. (1998). “Maps of dust infrared emission for use in estimation of reddening and cosmic microwave background radiation foregrounds”. In: *The Astrophysical Journal* 500.2, p. 525.

Shakura, Ni I and Rashid Alievich Sunyaev (1973). “Black holes in binary systems. Observational appearance.” In: *Astronomy and Astrophysics* 24, pp. 337–355.

Shen, Yue (2013). “The mass of quasars”. In: *arXiv preprint arXiv:1302.2643*.

Sijacki, Debora et al. (2015). “The Illustris simulation: the evolving population of black holes across cosmic time”. In: *Monthly Notices of the Royal Astronomical Society* 452.1, pp. 575–596.

Silk, Joseph and Martin J Rees (1998). “Quasars and galaxy formation”. In: *arXiv preprint astro-ph/9801013*.

Simmonds, Charlotte et al. (2018). “XZ: Deriving redshifts from X-ray spectra of obscured AGN”. In: *Astronomy & Astrophysics* 618, A66.

Skrutskie, MF et al. (2006). “The two micron all sky survey (2MASS)”. In: *The Astronomical Journal* 131.2, p. 1163.

Śniegowska, Marzena et al. (2022). “Modeling changing-look active galactic nuclei phenomenon in 1D using accretion disk instabilities”. In: *Astronomische Nachrichten* 343.1-2, e210065.

Soltan, Andrzej (1982). “Masses of quasars”. In: *Monthly Notices of the Royal Astronomical Society* 200.1, pp. 115–122.

Speranza, G et al. (2022). “Warm molecular and ionized gas kinematics in the type-2 quasar J0945+ 1737”. In: *Astronomy & Astrophysics* 665, A55.

Sunyaev, R et al. (2021). “SRG X-ray orbital observatory-Its telescopes and first scientific results”. In: *Astronomy & Astrophysics* 656, A132.

Tombesi, F et al. (2011). “Evidence for ultra-fast outflows in radio-quiet active galactic nuclei. II. Detailed photoionization modeling of Fe K-shell absorption lines”. In: *The Astrophysical Journal* 742.1, p. 44.

Tombesi, Francesco et al. (2010). “Evidence for ultra-fast outflows in radio-quiet AGNs-I. Detection and statistical incidence of Fe K-shell absorption lines”. In: *Astronomy & Astrophysics* 521, A57.

Tombesi, Francesco et al. (2013). “Unification of X-ray winds in Seyfert galaxies: from ultra-fast outflows to warm absorbers”. In: *Monthly Notices of the Royal Astronomical Society* 430.2, pp. 1102–1117.

Torricelli-Ciamponi, G et al. (2014). “Search for X-ray occultations in active galactic nuclei”. In: *Monthly Notices of the Royal Astronomical Society* 442.3, pp. 2116–2130.

Tozzi, G et al. (2021). “Connecting X-ray nuclear winds with galaxy-scale ionised outflows in two z 1.5 lensed quasars”. In: *Astronomy & Astrophysics* 648, A99.

Truemper, Joachim (June 1993). “ROSAT-A New Look at the X-ray Sky”. In: *Science* 260.5115, pp. 1769–1771. DOI: 10.1126/science.260.5115.1769.

Urry, C Megan and Paolo Padovani (1995). “Unified schemes for radio-loud active galactic nuclei”. In: *Publications of the Astronomical Society of the Pacific* 107.715, p. 803.

Venturi, G et al. (2021). “MAGNUM survey: Compact jets causing large turmoil in galaxies-Enhanced line widths perpendicular to radio jets as tracers of jet-ISM interaction”. In: *Astronomy & Astrophysics* 648, A17.

Venturi, Giacomo et al. (2017). “Ionized gas outflows from the MAGNUM survey: NGC 1365 and NGC 4945”. In: *Frontiers in Astronomy and Space Sciences* 4, p. 46.

Waters, Tim and Daniel Proga (2018). “Magnetothermal disc winds in X-ray binaries: poloidal magnetic fields suppress thermal winds”. In: *Monthly Notices of the Royal Astronomical Society* 481.2, pp. 2628–2645.

Weisskopf, Martin C. et al. (July 2000). “Chandra X-ray Observatory (CXO): overview”. In: *X-Ray Optics, Instruments, and Missions III*. Ed. by Joachim E. Truemper and Bernd Aschenbach. Vol. 4012. Society of Photo-Optical Instrumentation Engineers (SPIE) Conference Series, pp. 2–16. DOI: `10.1117/12.391545`. arXiv: `astro-ph/0004127 [astro-ph]`.

Wik, Daniel R et al. (2014). “NuSTAR observations of the bullet cluster: constraints on inverse compton emission”. In: *The Astrophysical Journal* 792.1, p. 48.

Wilkes, Belinda J et al. (2002). “The X-ray properties of 2MASS red active galactic nuclei”. In: *The Astrophysical Journal* 564.2, p. L65.

Wilkes, Belinda J et al. (2005). “XMM-Newton observations of red AGNs”. In: *The Astrophysical Journal* 634.1, p. 183.

Wolter, Hans (Jan. 1952). “Spiegelsysteme streifenden Einfalls als abbildende Optiken für Röntgenstrahlen”. In: *Annalen der Physik* 445.1, pp. 94–114. DOI: `10.1002/andp.19524450108`.

Yang, Qian et al. (2018). “Discovery of 21 new changing-look AGNs in the northern sky”. In: *The Astrophysical Journal* 862.2, p. 109.

York, Donald G. et al. (Sept. 2000). “The Sloan Digital Sky Survey: Technical Summary”. In: 120.3, pp. 1579–1587. DOI: `10.1086/301513`. arXiv: `astro-ph/0006396 [astro-ph]`.

Yuan, Feng et al. (2015). “Numerical simulation of hot accretion flows. III. Revisiting wind properties using the trajectory approach”. In: *The Astrophysical Journal* 804.2, p. 101.

Yuan, Weimin et al. (2022). “The Einstein Probe mission”. In: *arXiv preprint arXiv:2209.09763*.

Zanchettin, MV et al. (2021). “The IBISCO survey-I. Multiphase discs and winds in the Seyfert galaxy Markarian 509”. In: *Astronomy & Astrophysics* 655, A25.